Ligand-Protected Nanocluster Stability, Doping, and Prediction

by

Michael G. Taylor

Bachelor of Science in Chemical Engineering , University of

Nebraska-Lincoln, 2013

Submitted to the Graduate Faculty of

the Swanson School of Engineering in partial fulfillment

of the requirements for the degree of

Doctor of Philosophy

University of Pittsburgh

2019

UNIVERSITY OF PITTSBURGH

SWANSON SCHOOL OF ENGINEERING

This dissertation was presented

by

Michael G. Taylor

It was defended on

May 2, 2019

and approved by

Giannis Mpourmpakis, PhD, Assistant Professor, Department of Chemical and Petroleum
Engineering

J. Karl Johnson, PhD, Professor, Department of Chemical and Petroleum Engineering

Christopher Wilmer, PhD, Assistant Professor, Department of Chemical and Petroleum
Engineering

Rongchao Jin, PhD, Professor, Department of Chemistry, Carnegie Mellon University

Dissertation Director: Giannis Mpourmpakis, PhD, Assistant Professor, Department of
Chemical and Petroleum Engineering

Ligand-Protected Nanocluster Stability, Doping, and Prediction

Michael G. Taylor, PhD

University of Pittsburgh, 2019

Though new nanomaterials are synthesized everyday for applications ranging from targeted drug delivery to chemical catalysis via ligand-stabilized colloidal growth methods, the physical underpinnings of these processes are often unknown. Without detailed knowledge of growth mechanisms or an understanding of the stability of the final product, synthesis of colloidal nanomaterials often relies on trial-and-error experimentation. Towards enabling nanomaterials-by-design, precise control of nanomaterial morphology (i.e. size, shape, chemical composition, and chemical ordering) is desired as morphology often dictates properties. To control morphology, an understanding of how nanomaterial structure relates to stability is needed. An ideal class of colloidal nanomaterials for studying structure-stability relations are the atomically-precise thiolate-protected metal nanoclusters (MNCs).

In this work, we focus on developing deeper understanding of the structure-related remarkable stability of MNCs and their physicochemical transformations utilizing *ab initio* computational methods. First, we introduce a novel Thermodynamic Stability Model (TSM) for ligand-protected MNCs and demonstrate its power for understanding the stability of a wide range of MNCs. Next, we focus on the energetics of heterometal doping and ligand/dopant-mediated precise transformations of several smaller Au MNCs, showing remarkable agreement with experimental results. Finally, we demonstrate the application of the TSM to capture a wide range of experimental heterometal doping observations in Au_{25} MNCs for which no simple explanation previously existed. We also use the TSM to make predictions related to dopant locations and concentrations within the Au_{38} MNC.

Overall, this dissertation advances knowledge of the underpinnings of the stability of ligand-protected atomically-precise MNCs contributing to MNC design for targeted applications.

Table of Contents

List of Tables

List of Figures

Preface

There are so many people and organizations during my time at Pitt who have helped make the last few years of work, play, and life joyful and this doctorate achievable. First and foremost I recognize the work and love of God in my life through His only Son Jesus. The faith, focus, and strength He has given me over the last few years has been paramount in navigating the waters of a PhD in Chemical Engineering. I am especially grateful to Him for helping me meet and, soon after, marry my wife, best friend, and love of my life, Natalie Nieman. She has been loving, kind, helpful, supportive, and patient towards me through the thick of it.

More than anyone else, except God, the person who has contributed most to me in pursuit of the goal of a PhD is my advisor, Dr. Giannis Mpourmpakis. Yanni, you have been a phenomenal advisor and hopefully will be a life-long friend. Thank you so much always for pushing me to do better. Your positive attitude and solid direct criticism have helped form me into the researcher I am. Dr. Johnson, thank you for your help with advising me and being there for conversations about life, work, and career - and for helping me so much as a reference writer. Dr. Wilmer, thank you for teaching me invaluable skills in scientific visualization, your career advice, and for your very open attitude towards scientific discussions, and networking. Dr. Jin, thank you so much for being a phenomenal collaborator, sharing your talented graduate students (especially Dr. Qi Li and Yingwei Li) with our lab, and for your help with serving as reference for me.

From our lab (CANELa) I have to recognize my long-time colleagues and friends Natalie Austin and Pavlo Kostetskyy for their discussions, comments, and willingness for peer-commiseration when needed. Thanks to Zihao Yan for being a great Master's student, friend, and mentee. Also thanks to the other members of CANELa, whom I consider all good friends and colleagues - Dr. Mudit Dixit, Michael Cowan, James Dean, Ashley Mascareno, Xi Peng, Dr. Rosalba Juárez Mosqueda, Robin Tan, Dr. Dylan Bayerl, Rafaelle Cheula, Emily Freeman, Anantha Nagarajan, Peter Tancini, John Hoover, Isadora Carnaval, and all the other Undergraduates who have worked with the Lab over the years. Outside of our Lab,

I am also extremely grateful for the loving and consistent support of my parents, Carol Gilbert and Edward Taylor, who have been there from the beginning and have always encouraged and motivated me to do what is right, and what is interesting to me (but also practical). Rounding out family shout-outs, I am also grateful for the love and support from my brother Ian and his wife Naomi, nephew Liam, sister Dae (we miss you and love you so much), extended Family in Nebraska, South Carolina, and California, family in-laws in both Ohio and Washington, and adopted South African family in Pittsburgh (Yinz the best Bert and Talitha!). Outside my family I also have to recognize the huge influence my Church family has been during my time here at Pitt. Redeemer Community Church in Pittsburgh has been the most consistent thing in life in Pittsburgh and lions share of my social life outside work. I am grateful to all the dear friends made at Redeemer (and outside - cheers to Matt - the coolest co-bible study leader I know!) throughout my tenure at Pitt. Shout out to Pastors Dan and Adam for your consistency as leaders of Redeemer as a local body of Christ.

"All things have been handed over to me by my Father, and no one knows the Son except the Father, and no one knows the Father except the Son and anyone to whom the Son chooses to reveal him. Come to me, all who labor and are heavy laden, and I will give you rest. Take my yoke upon you, and learn from me, for I am gentle and lowly in heart, and you will find rest for your souls. For my yoke is easy, and my burden is light."

Matthew 11:27-30

1.0   Introduction

Following the discovery of emergent catalytic properties of nanoscale gold (famously inert in bulk) for low-temperature CO oxidation by Haruta [2], the race for precise nanoscale engineering has rapidly accelerated.[3] For example, we have shown efficient engineering at the nanoscale has potential to transform problems from excessive kidney stone growth[4, 5] to screening of the stability of possible catalytic nanoparticles (NPs).[6] While a variety of synthetic routes for NPs have been created [7], few are scalable to large quantities [8] or allow for atomic-level precision in the synthesized NPs.[9] More precise control of NP structure is highly desirable as NP morphology (i.e. size, shape, composition, and chemical ordering) often directly relates to the useful pysicochemical properties of the NP for specific applications.[3] For example, we showed that the activity of gold NPs for the catalytic oxidation of CO trends with Au NP size.[10]

Therefore, moving towards application-targeted nanoscale engineering will require atomic-level synthetic precision.[11]

1.1   Atomically-Precise Ligand Protected Metal Nanoclusters (MNCs)

One of the only classes of inorganic nanomaterials for which atomic-level precision has been achieved is ligand-protected noble metal nanoclusters (MNCs). Since the first successful crystallization and structural determination of a MNC, the $Au_{102}(MBA)_{44}$ MNC, in 2007 [12], several other atomically-precise noble metal MNCs have been solved via single crystal X-ray diffraction (XRD).[13] These XRD-resolved, thermally-stable ("magic-number") thiolated MNCs ($M_n(SR)_m$, where M=metal and SR=thiolate group) range from 10 to a few hundred metal atoms.[9, 14] A large majority of these precise MNCs are produced using a Brust-Schiffrin-type synthesis.[15] In the Brust-Schiffrin synthesis, metal salts (most notably, Au), are reduced in the presence of thiolate ligands to produce MNCs of specific sizes, depending on the ligands and reaction conditions used.[16] Applying higher temperatures and

excess ligand to a product mixture from an initial reduction step in a process named "size-focusing",[17] in combination with ligand exchange induced size/structural transformation (LEIST)[18] techniques have enabled the synthesis of a series of atomically-precise MNCs. These synthesis techniques favor thermodynamic control as a final step, making their stability more a function of thermodynamic stability. A schematic view of these two synthetic techniques adapted from work by Jin et al. [17, 18] along with examples of solution phase species at each step is highlighted in Figure 1.1.
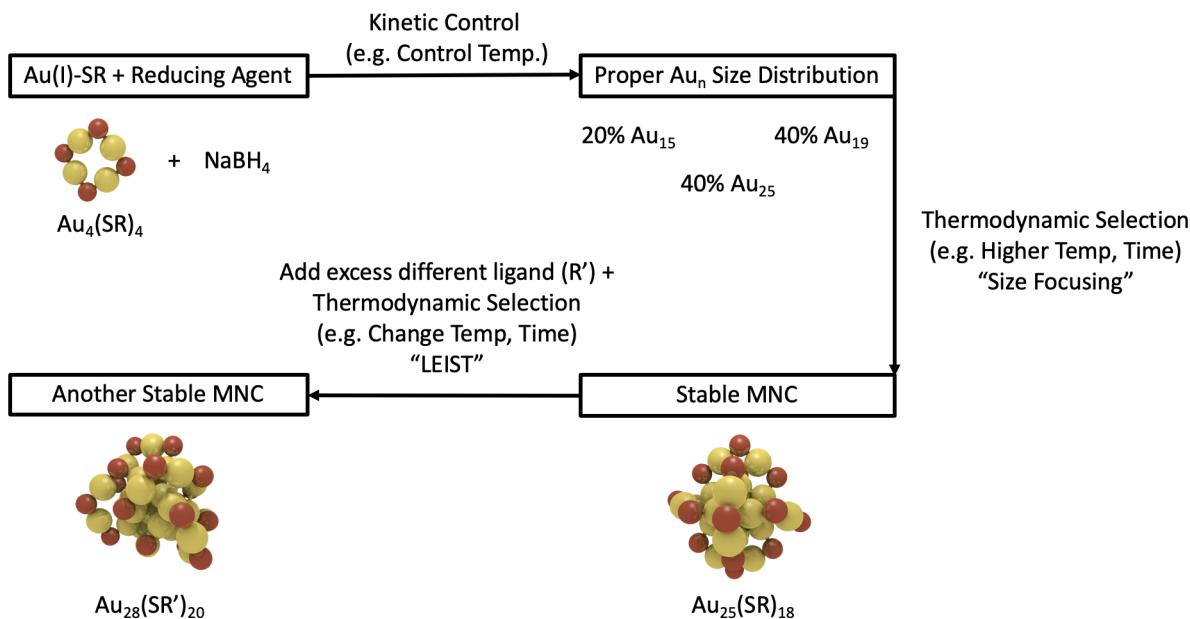
Figure 1.1: Schematic overview of size-focusing and LEIST techniques used in synthesizing and isolating atomically-precise MNCs.

1.2   Theories for MNC Structure and Stability

Given their atomically-precise structure, MNCs are ideal for first-principles-based computational modeling and have been employed to probe structural and electronic properties of these magic-number MNCs. In particular, the "divide-and-protect" theory [19] emerged

in an effort to rationalize the observed structural characteristics of Au MNC and the "superatom" theory to explain the magic-number MNC stability.[20, 21]

The divide-and-protect theory suggests that Au MNCs form from maximizing Au-Au and Au-S interactions that take place in the core and on the surface of the MNCs, respectively. This leads to MNC structures consisting of metallic Au cores with shell structures formed from thiolate-Au bond networks, –SR(-Au-SR)$_n$-, known as "staple motifs". [22, 23] Divide-and-protect theory has proven effective in suggesting MNC structural characteristics, with nearly every MNC displaying such a core-shell structure. However, the divide-and-protect theory only suggests structural trends and does not introduce quantitative descriptors for MNC stability, resulting in a loose general structural criteria. Here, we define structure as composition (Au vs. S content) in addition to MNC size and shape (morphology).

The superatom theory, on the other hand, states that magic-number stability results from the formation of closed-shell electronic orbital structures, similar to noble gases.[20, 21] This theory has been successful in explaining the optical and catalytic properties of several magic-number MNCs, but has been shown weakness as a universal descriptor for the thermodynamic stability of thiolated Au MNCs.[24] In particular, the $Au_{20}(SR)_{16}$ and $Au_{36}(SR)_{24}$ MNCs do not fall in the predictions of the superatom theory, but have been successfully experimentally synthesized and isolated under thermodynamic conditions (i.e. long times of reaction).[25, 26] To capture the stability of MNC like the $Au_{20}(SR)_{16}$, an extension to the "superatom model" called the "superatom newtork" was proposed.[27] This superatom network theory states that all MNCs are either simple superatoms, or are comprised of multiple superatomic subunits combined together. Following this logic of the superatom network model, a "grand unified model" was also proposed stating that all Au MNCs are built of electronically closed-shell subunits.[28, 29] Although the combination of the superatom network/grand unified models are able to capture the stability of all reported Au MNC structures, they should theoretically apply to all metals that fall on the same column of the periodic table as they all apply simple electron counting and shell closure rules. Yet, metals that fall in the same periodic table column (e.g. Au vs. Cu) do not form MNCs of the same size (number of metal atoms and ligands) and structures. Most recently, combinations of divide-and-protect and electron counting methods have been extended to "growth rule" concepts, where larger MNCs

share structural trends with smaller MNCs.[30] Such methods, however, do not clarify the extraordinary stability of particular MNC compositions, sizes, or structures in a "growth rule" path compared to other possible MNCs. This is particularly important as the thiol layers and metals of the MNCs and the MNCs themselves have been shown to be in dynamic equilibrium. [31, 32]

Beyond first-principles calculations, electron-counting methods, and structural rules, simple geometric scaling laws relating the total number of Au atoms (n) to the number of ligands (m) in MNCs have been discovered, though these relations are not designed to predict specific MNC morphologies.[33, 34] In summary, although rich work has been completed in analyzing and predicting MNC structure, exceptions and weakness of each reveal the need for new methods for understanding and rationalizing the "magic" stability of these atomically-precise ligand-protected MNCs.

1.3   Heterometal Doping of MNCs

Heterometal doping and alloying of Au MNCs has been shown to modulate the optical,[35] catalytic,[36] and stability [37] properties of the MNCs and is therefore a promising avenue towards application-driven MNC design. Experimental techniques such as anti-galvanic substitution,[38] intercluster reactions,[39] and simple metal exchange[40] have been successful in doping or alloying heterometals into monometallic MNC frameworks.[41] The properties of doped MNCs are dictated by both the precise dopant locations within the MNC[42] along with dopant concentrations.[35, 43] Towards control of dopants, the first prediction (via density functional theory (DFT) calculations[44]) of doped MNCs and their emergent properties highlighted the potential of doping within the $[Au_{25}(SR)_{18}]^-$ MNC. From this original work two design rules emerged for dopant viability. First, the dopant metal should be of similar size to Au, where metals with similar diameters to Au will not cause a MNC to geometrically reconstruct. Second, the resultant doped MNC should have a similar HOMO-LUMO gap to the undoped MNC. Since this initial work, DFT has proven invaluable in determining the feasibility of doping within specific MNC frameworks [45] and can

give reliable dopant position-dependent energetics for several metals.[46] For some dopants, however, DFT has not matched experimental observations for dopant location and the design rule of HOMO-LUMO gap similarity has failed to predict doping feasibility.[47, 48, 49] Additionally,theoretical studies addressing observed dopant concentrations are rare and there is no existing proven rules for dopant concentration rationalization.[42] Therefore, new theories and methods are needed towards understanding dopant positions and concentration effects within heterometal-doped MNCs.

2.0 Thermodynamic Stability of Ligand-Protected MNCs

The content of this chapter is taken from M. G. Taylor and G. Mpourmpakis, "Thermodynamic Stability of Ligand-Protected Metal Nanoclusters," *Nature Communications*, vol. 8, no. May, p. 15988, 2017.

2.1 Computational Methods

In this work we used DFT calculations to develop and propose a new Thermodynamic Stability Model (TSM) and structural trends in Au MNCs. Specifically, we used the BP-86[51, 52] functional combined with the def2-SV(P) basis set[53] accelerated with the resolution of identities (RI) approximation[54, 55] as implemented in the Turbomole package.[56] Structures were taken directly from previously published work and the R groups of the thiolates were substituted by methyl groups.[12, 57, 58, 25, 1, 59, 60, 61, 62, 63, 64, 65, 66] The BP-86 functional has been successfully used on thiolated-MNC systems [67, 68] and the R=methyl group substitution has been previously applied in computational Au MNC structural determinations.[69, 70] All MNCs were relaxed with a quasi-Newton-Raphson method and were performed without any symmetry constraints. Two methods were used to identify if Au atoms were "core" or "shell", that of natural bond orbital (NBO) charge analysis and that of measuring S-contacts of Au atoms in the structure, where the shell Au atoms have exactly 2 bonded sulfur groups.[71] These two methods were in perfect agreement over all MNCs. With core and shell designations, we isolated the core and shell sections of the MNCs and performed single point energy calculations on each section. From the 1) optimized MNC structure, 2) separated core and 3) separated shell results, two energetic factors of interest, Shell-to-core binding energy (BE) and Core Cohesive Energy (CE) were calculated. The shell-to-core BE is defined as:

$$Shell - to - core\ BE = \frac{E_{FullCluster} - E_{Shell} - E_{Core}}{n_{ShellInt}} \qquad (2.1)$$

where E_x = electronic energy of group X and $n_{ShellInt}$ = number of shell contacts interacting with the core. $n_{shellInt}$ is largely dictated by the number of shell Au atoms in contact with the surface of the cores (less than $4\mathring{A}$ from the nearest core Au atom) because metal-metal bonds dominate the shell-to-core BE (see Figure B3 and related note in Appendix B). Beyond shell metal contacts to the cores, SR groups that are not bound to any shell metals but are bound directly to core metals represent a direct shell-to-core contact and thus are also included in $n_{ShellInt}$. The Core CE is defined as:

$$Core\ CE = \frac{E_{FullCluster} - n_c * E_{MetalAtom} - E_{Shell}}{n_c + n_{ShellInt}} \tag{2.2}$$

where n_c = number of metal atoms contained in the core structures (and E is the total electronic energy). For each of the core structures different multiplicities were tested and the lowest-energy spin states were selected for the core CE calculation. For the gas phase minimum energy clusters and MNC core structures the CE is defined:

$$CE = \frac{E_{Cluster} - n_c * E_{MetalAtom}}{n_c} \tag{2.3}$$

For the core structures, Lennard-Jones radii were used to determine the coordination numbers (CNs). [72] COnductor-like Screening MOdel (COSMO) implicit solvation models were also employed to gauge the effect of dichloromethane (ϵ=8.93) and water ϵ=78.46 solvents on MNC energetics. [73, 74]

2.2 Results and Discussion

2.2.1 Derivation of the Thermodynamic Stability Model (TSM)

The TSM theory is derived from a thermodynamic argument from the following the chemical potentials of all the metal atoms after a reducing agent has been added to the final, fully-formed MNCs. Simply stated, in the TSM, the BE of the shell to the core of a synthesized MNC (Shell-to-core BE) should be balanced with the CE of the core. These two regions or phases of metals in the MNCs are selected as they have been shown to

be chemically distinct by the divide and protect theory and other work on self-assembled monolayers of thiolate on Au.[19, 75] Since we are separating the MNC into two distinct phases (core and shell) which are in direct contact, in order to achieve chemical equilibrium, the partial molar Gibbs free energy (chemical potential (μ) of the two phases should be equal (so $\Delta\mu$(MNC)=0).The proposed stability descriptors of core CE and shell-to-core BE are also linked to these thermodynamic parameters. Towards linking the proposed descriptors to thermodynamic parameters, we select a thermodynamic reference state that corresponds to the solution in the Brust-Schiffrin synthesis immediately following the addition of the reducing agent, consisting of solvated M^0 and staple groups, SR-(M-SR)$_n$, that then, self-assemble to form the MNC core and shell regions, respectively. For example, we envision an initial state where 23 Au^0 atoms exist along with 6 SR-Au-SR-Au-SR and 3 SR-Au-SR staple groups (in addition to excess thiol and solvent) immediately following the addition of the reducing agent. Following the self-assembly process over thermodynamic time frames (e.g. 24 hours), the final state would be the assembled $Au_{38}(SR)_{24}$ MNC in the same solution. Given experimental evidence [76], we assume the difference of the partial molar entropy (s) of the M^0 and staple group between the reference solution and the MNC phases are equivalent. In addition, the core CE in the presence of the shell can largely represent the partial molar enthalpy (h) of the Au atoms in the core relative to the reference solution phase, as electronic energy will dominate h values in a constant volume, liquid phase reaction. To make the analysis of the core CE in the presence of the shell we rely on the core CE and shell-to-core BE above in Equation 2.2:

$$Core\ CE = \frac{E_{FullCluster} - n_c * E_{MetalAtom} - E_{ShellInt}}{n_c + n_{ShellInt}} \qquad (2.4)$$

where E_x is the electronic energy of species X, n$_c$ is the number of metal atoms in the core, and $n_{ShellInt}$ is the number of interactions between the shell and core. This equation can then be rewritten as:

$$Core\ CE = \frac{E_{FullCluster} + n_c * CE_{Core} - E_{Core} - E_{Shell}}{n_c + n_{ShellInt}} \qquad (2.5)$$

where CE_{Core} represents the atomization energy for the isolated gas-phase core as defined in Equation 2.3. Equation 2.5 can then be rearranged as:

$$Core\ CE = \frac{n_c * CE_{Core} + n_{ShellInt} * Shell-to-core\ BE}{n_c + n_{ShellInt}} \tag{2.6}$$

Where $Shell-to-core\ BE$ is defined in Equation 2.1. Thus, the CE of the metal atoms in the core in the presence of the shell can be viewed as a weighted average of the gas phase core CE and shell-to-core BEs. Finally, the shell-to-core BE likewise is treated as the h of the core-binding shell M atoms relative to the reference solution phase, considering interactions between staple groups are known to be very weak relative to their interactions with the core M^0 atoms.[75] These assumptions are summarized as:

$$\Delta\mu_{MCore}^{Solution-MNC} = \Delta h_{MCore} - T\Delta s_{MCore} \approx CoreCE(withshell) - T\Delta s_{MCore} \tag{2.7}$$

and,

$$\Delta\mu_{MShell}^{Solution-MNC} = \Delta h_{MShell} - T\Delta s_{MShell} \approx Shell-to-core\ BE - T\Delta s_{MCore} \tag{2.8}$$

where μ is chemical potential, h is partial molar enthalpy, s is partial molar entropy, T is temperature, and Solution-MNC indicates the difference between the initial solution-phase thermodynamic reference and the formed MNC thermodynamic reference. Thus, the chemical potential difference between the surface and core metal atoms is given as:

$$\Delta\mu(MNC) = 0 = \Delta\mu_{MShell}^{Solution-MNC} - \Delta\mu_{MCore}^{Solution-MNC} \approx Shell-to-coreBE - CoreCE \tag{2.9}$$

which indicates that for the stable MNCs, this difference in chemical potential should equal to zero, highlighting a balance of chemical potentials at this core-shell interface. This thermodynamic analysis helps rationalize the lack of temperature-dependence in the stability of MNCs in temperature regimes where enthalpic dominate entropic contributions. In addition, it highlights the thermodynamic basis for the TSM for MNC stability.

2.2.2 Testing Applicability of TSM to MNCs

Figure 2.1 highlights all DFT-optimized Au nanostructures along with the designation of which atoms are part of the core or shell. We note that the definitions of core and shell metal atoms in Figure 2.1 agrees with previous work [25, 1, 59, 60, 61, 77, 78, 62] with the exception of $Au_{18}SR_{14}$ and $Au_{102}SR_{44}$, where the NBO charge analysis and S-bonding methods revealed that the core could be more precisely defined by 8 atoms rather than 9, and 77 rather than 79 (see analysis in B and Figure B2). [25] When we applied the TSM in Figure 2.2, we plot the calculated shell-to-core BE vs. the CE of the cores for the experimentally determined thiolate-protected Au MNCs (points colored in gold). Interestingly, we reveal a near-perfect match between the shell-to-core BE and the CE of the metal cores. This trend highlights a unique physicochemical feature of the experimentally synthesized $Au_n(SR)_m$ MNCs: that there is a fine balance between the CE of the core and the BE of the shell to the core.

Interesting enough is the observation that this criterion applies to both neutral (Figure 2.1 (a)-(i)) and charged (Figure 2.2(i)) MNCs. Additionally, the two structures which would not be identified as stable by the superatom theory, $Au_{20}SR_{16}$ and the $Au_{36}SR_{24}$, are shown as stable here by the TSM. In order to test if our TSM can be extended to other metals, we performed the same analysis for the $[Ag_{25}(SPhMe_2)_{18}]^-$ MNC (Figure 2.2(ii)) which has been experimentally synthesized.[79] As shown in Figure 2.2, again, the CE of the core and the BE of the shell to the core strike a perfect energy balance (see silver point on parity graph). It should be noticed that the Ag MNC is negatively charged as in the case of the $[Au_{25}SR_{18}]^-$ MNC (Figure 2.2(i)), verifying not only that this trend holds for different metals, but also when these metals are charged. As an additional validation test, we created the $[Cu_{25}SR_{18}]^-$ MNC (Figure 2.2(iii)) based on the crystallographic structure of the corresponding $[Au_{25}SR_{18}]^-$ MNC. It is worth mentioning that, according to the superatom theory, the $[Cu_{25}SR_{18}]^-$ should be a thermodynamically stable nanostructure since Cu and Au are metals with similar electronic shell closure (same period metals).

However, the $[Cu_{25}SR_{18}]^-$ has not been experimentally synthesized as of yet, and, we note that that according to our model, the CE of the core dominates the BE of the shell

a Au$_{18}$SR$_{14}$ **b** Au$_{20}$SR$_{16}$ **c** Au$_{24}$SR$_{20}$

n_c=8 Au $n_{ShellInt}$=10 n_c=7 Au $n_{ShellInt}$=10 n_c=8 Au $n_{ShellInt}$=12

d Au$_{28}$SR$_{20}$ **e** Au$_{30}$S(SR)$_{18}$ **f** Au$_{36}$SR$_{24}$

n_c=14 Au $n_{ShellInt}$=14 n_c=17 Au $n_{ShellInt}$=13 n_c=20 Au $n_{ShellInt}$=16

g Au$_{38}$SR$_{24}q$ **h** Au$_{38}$SR$_{24}t$ **i** Au$_{102}$SR$_{44}$

n_c=23 Au $n_{ShellInt}$=15 n_c=23 Au $n_{ShellInt}$=16 n_c=77 Au $n_{ShellInt}$=25
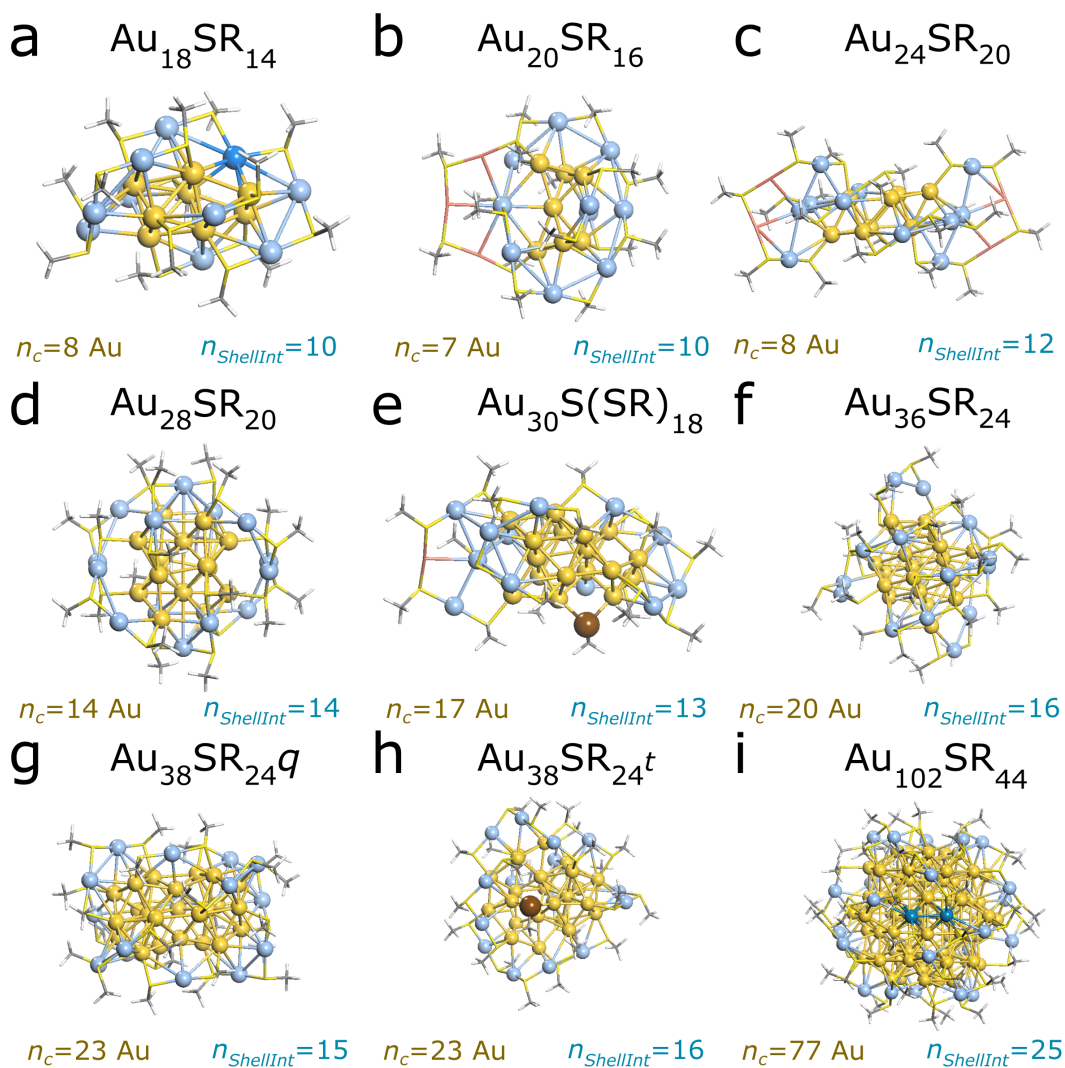
Figure 2.1: Relaxed geometries of the experimentally-synthesized MNCs. (a) $Au_{18}SR_{14}$ (b) $Au_{20}SR_{16}$ (c) $Au_{24}SR_{20}$ (d) $Au_{28}SR_{20}$ (e) $Au_{30}S(SR)_{18}$ (f) $Au_{36}SR_{24}$ (g) $Au_{38}SR_{24}q$ (h) $Au_{38}SR_{24}t$ (i) $Au_{102}SR_{44}$. Ligands (S-CH$_3$) are shown in stick representation while core and shell atoms, in ball and stick, and have been colored yellow and blue, respectively. In (b) and (c), shell Au atoms which do not interact with the core have been colored red and are shown in stick representation, while in (a) and (i) shell Au atoms which were previously identified as core are colored darker blue. In (e) and (h) shell sulfur atoms which are not directly bound to a shell Au atom are shown as brown balls.
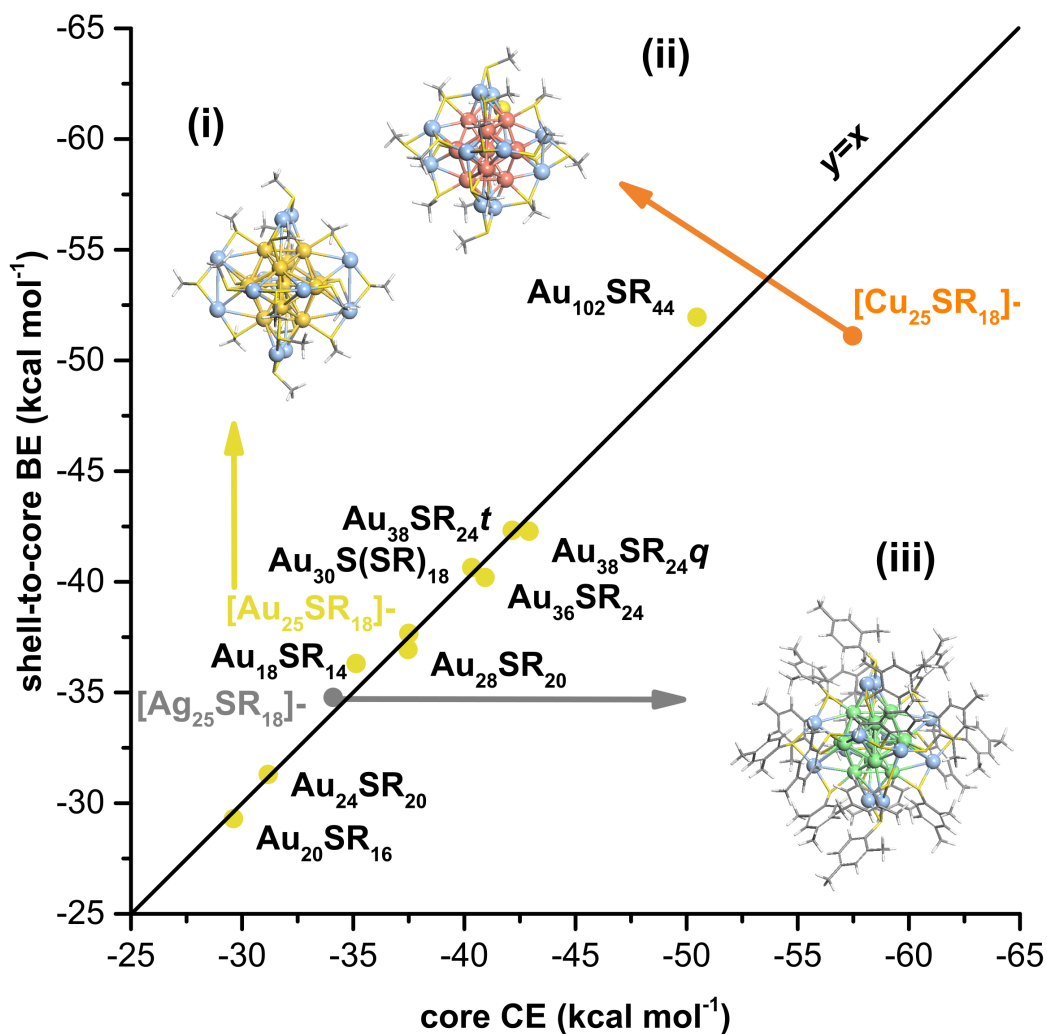
Figure 2.2: Parity between core CE and the shell-to-core BE. The corresponding structures of the $Au_n(SR)_m$ MNCs are presented in Figure 2.1 except from the optimized structures of (i) $[Au_{25}SR_{18}]^-$, (ii) $[Cu_{25}SR_{18}]^-$, and (iii) $[Ag_{25}(SPhMe_2)_{18}]^-$ MNCs, which are shown as insets in the graph. For (i)-(iii) n_c=13 metal atoms (Au/Cu/Ag) and $n_{ShellInt} = 12$ as in Figure 2.1. The shell metal atoms are shown in blue, whereas, the Cu and Ag core metal atoms are shown in red and green, respectively. Here, the Au and Ag MNCs reported were experimentally determined. The Cu MNC structure is hypothetical, relaxed from the Au MNC analogous structure (i).

to the core (red point in Figure 2.2 deviating from the parity line). While the challenge with synthesizing Cu MNCs is largely tied to the persistence of the Cu(I) state [80], our calculation imposes the ideal experimental case where the Cu in $[Cu_{25}SR_{18}]^-$ remains Cu(0). Therefore, we suggest that, at least for this ligand configuration (type and number of ligands), the $[Cu_{25}SR_{18}]^-$ cannot be a magic number MNC. We thus believe that the $[Cu_{25}SR_{18}]^-$ serves as a case where the core CE is not balanced with the shell-to-core BE, ruling out this energetic balance as a simple interfacial effect.

It should be noticed that when switching the thiolate R group to methyl (to reduce computational cost), attention should be given to the effect that this change introduces to the stability of the shell structure, and in turn, to the shell binding to the core of the MNC. Toward understanding ligand impact we highlight that experimentally[81] and theoretically[58], the $[Au_{25}SR_{18}]^-$ MNC has been shown to be stable for a wide variety of ligands, and was successfully synthesized even with small, ethyl R groups.[82] Therefore, the exceptional structural stability of $[Au_{25}SR_{18}]^-$ MNC seems to be experimentally independent of the ligand type, highlighting the importance of metal structure and Au/S stoichiometry in determining stable MNCs. For MNC structures investigated here, interactions at the interface between their core and shell regions should be, to a large degree, unaffected by the ligand selection (see Figure B4 where $Au_{18}SR_{14}$ and $[Au_{25}SR_{18}]^-$ optimization with full ligands resulted to minor energy shifts and for detailed analysis of the $[Ag_{25}SR_{18}]^-$ case). In addition, metal-metal interactions at the interface are energetically far stronger than the ligand-ligand interactions and capture the core-shell and the relative MNC stability. However, enhanced ligand-ligand (R-group) interactions can impact the overall MNC stability as seen in several other recent works.[83, 84] For example, in the case of the $[Ag_{25}]^-$ MNCs, a pi-stacking is observed in the original experimental crystal structures between the phenyl groups present on the shell of the MNC. Although the R=methyl group substitution has been shown to have small effect on the RS-Au bond strength [70, 67], a hydrogen-bond network formed at the MNC surface by groups of the ligands can potentially induce strain on the shell structure, changing in turn the shell-to-core BE (see Figure B4). Interestingly, this observation is in agreement with recent work where conversion from $Au_{38}SR_{24}$ (SR=phenylethanethiolate (PET)) to $Au_{36}SR_{24}$ (SR=4-tert-butylbenzenethiolate (TBBT)) was achieved in solution by swapping

13

the thiolate R groups from PET to TBBT, altering the hydrogen-bond network formed the surface of the MNCs.[85]

To further prove that this structural thermodynamic stabilization is a general behavior and originates solely from the energy balance between the core and shell of the MNCs, we analyzed CE and BE in the presence of the common [45] dichloromethane and water solvents (see Figure B5). Similar to Figure 2.2, the parity between core CE and shell-to-core BE was maintained, with the solvent only weakly affecting the shell-to-core BE. Moreover, we have also tested different DFT methods. In Table D3), core CE (kcal mol^{-1}) and shell-to-core BE (kcal mol^{-1}) from BP-86 [52, 51], PBE [86] and BLYP [51, 87] from single point energy calculations on the BP-86 optimized $[Au_{25}SR_{18}]^-$ structure. We note that there is a tight match between the core CE and shell-to-core BE regardless of density functional for the BLYP, BP-86, and PBE methods.

2.2.3 Synthetic Accessibility and Structural Implications from TSM

To develop a functional "boundary" between synthetically accessible and non-accessible MNCs with the TSM we performed a linear regression on all the experimentally synthesized MNCs with 95% confidence and superimposed the prediction bands (See Figure 2.3).To explore the effectiveness of the 95% confidence and prediction bands in distinguishing between non-stable and stable MNCs we relaxed additional hypothetical MNCs. Beyond the hypothetical $[Cu_{25}SR_{18}]^-$ MNC, we investigated the $Ag_{18}SR_{14}$, $Cu_{18}SR_{14}$, $Ag_{38}SR_{24}q$, and $Cu_{38}SR_{24}q$ theoretical MNCs generated directly from their corresponding Au MNC analogs. We found that they exhibit CE and BE values that deviate beyond the 95% prediction band (Figure 2.3). Additionally, we have tested our method on four theoretically-predicted Au MNCs, the $Au_{18}SR_{14}$,[63] $Au_{20}SR_{16}$,[65] $Au_{24}SR_{20}$,[88] and $Au_{40}SR_{24}$,[64] and showed that two ($Au_{24}SR_{20}$ and $Au_{40}SR_{24}$) out of the four exhibit similar deviation from parity as the theoretical Cu MNCs, whereas, the $Au_{18}SR_{14}$ and $Au_{20}SR_{16}$ MNCs exhibit the CE and BE energy balance. Therefore, this TSM energetic balance is sensitive to the MNC structure and the 95% prediction bands can further be used as potential quantitative "cutoffs" to screen synthetically-accessible MNCs with current best MNC structural prediction practices. [89]
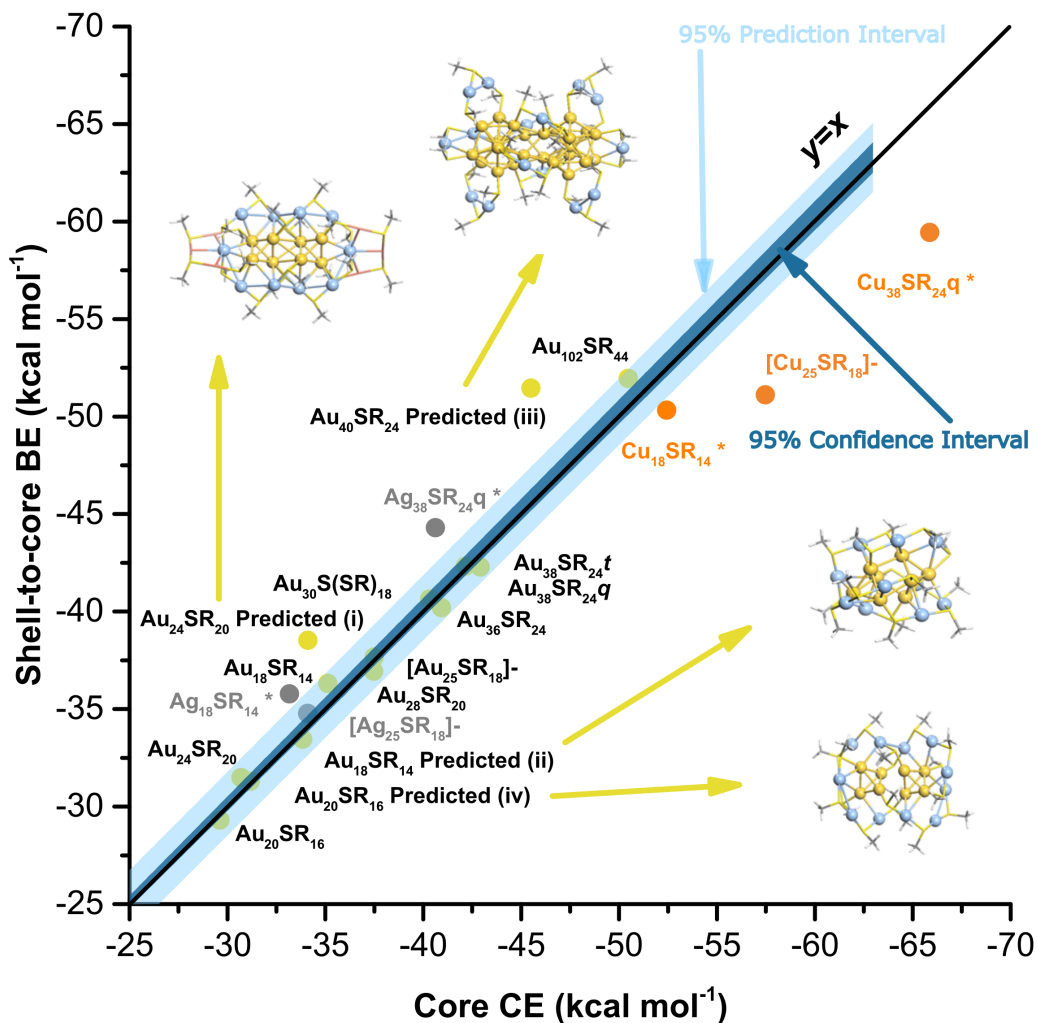
Figure 2.3: Statistical prediction band as synthesizability cutoff. Parity plot between core CE and the shell-to-core BE with 95% Confidence and Prediction bands from experimentally-synthesized Au MNCs superimposed. Additional points to Figure 2.2 include: 1) theoretically predicted Au nanoclusters (NCs) (i) $Au_{24}SR_{20}$, (ii) $Au_{18}SR_{14}$, (iii) $Au_{40}SR_{24}$, and (iv) $Au_{20}SR_{16}$ and 2) MNCs of different metals (*) generated and optimized from their analogous experimental Au MNC structures.

Additionally, because the developed TSM is based on the morphology-dependent energetic factors of CE of the core and the BE of the shell to the core, we expect these properties to correlate with the structural characteristics of the MNCs (i.e. size and shape). For example, it is well-known that the CE of metals scale linearly with $n_m^{-1/3}$, where n_m is the number of metal atoms in a pure metal nanocluster (NC).[90] Actually, one can apply first principles calculations to derive such linear trends, the limit of which shows the CE of the bulk, when $n_m \to$ inf, as has been shown in the case of Au.[90, 91] In Figure 2.4(a) we present such an analysis (core CE vs. $n_c^{-1/3}$, where n_c is the number of Au atoms in the core of the MNCs) and superimpose the shell-to-core BE results, highlighting the linearity between both energetic factors with $n_c^{-1/3}$ for the thermodynamically-stable Au MNCs. The reason $n_c^{-1/3}$ trends linearly with CE is attributed to the decrease in the fraction of low-coordinated (surface) sites observed on the MNCs as the cluster size increases.[91] Surprisingly, the shell-to-core BE was also found to scale linearly with $n_c^{-1/3}$, with almost identical behavior (see linear fits) as the CE. The identification of a common structural descriptor for the CE and the shell-to-core BE behavior on the MNCs helps rationalize the observed parity between these two energy contributions in Figure 2.2. Since the $n_c^{-1/3}$ shows how the low coordinated sites scale with nanocluster size (number of metal atoms, n_c), then we should expect that the average CN to scale linearly as well with both the CE and the shell-to-core BE. This behavior is clearly demonstrated in Figure 2.4(b). The average CN on Au can practically range from 0 (atom) to 12 (bulk). As the average CN of the nanocluster increases, the CE increases (more exothermic values) because the Au atoms tend to form more bonds with their neighbors, increasing the overall stability of the nanocluster. On the other hand, as we have recently shown in the area of catalysis, the adsorbates show higher BEs (more exothermic) on sites of the nanoclusters with low CNs.[92, 10] However, this is not the case here (see red point data in Figure 2.4(b)). The thiolated-Au shell network binds the core in a way that is counterintuitive to the common belief: as the average CN of the MNC core increases, the adsorption strength of the shell increases as well. This counterintuitive trend is highlighted by the difference between the predicted and experimental core structures (and resulting deviation from the parity plot) in the $Au_{24}SR_{20}$ MNC, where the experimental structure showed a core with lower CN than the predicted structure (see Figure B4).[59, 88] In Figure

2.4(c) we plot the shell-to-core BE vs. the shell $n_{Au} \ n_S^{-1}$ ratio (red circles), where n_{Au} is the number of shell Au atoms and n_S is the number of sulfur atoms on the shell (equivalent to m in Au_nSR_m). The shell $n_{Au} \ n_S^{-1}$ ratio demonstrates the cationic character degree of Au on the shell of the MNC (S-R$^{\delta-}$ interacting with Au$^{\delta+}$) and concentration of bridging thiol groups (SR groups not directly bound to the cores). On the same graph, we plot the average CN of the MNC cores vs. the $n_{Au} \ n_S^{-1}$ ratio (black rectangles) on the shell. Notice that both the shell-to-core BE and the core CN scale linearly with the shell $n_{Au} \ n_S^{-1}$ ratio. It can be observed that the lower the $n_{Au} \ n_S^{-1}$ ratio, the stronger the shell-to-core BE because of both the increased electrostatic interactions between the core and shell Au atoms (latter are charged more positively) and the decreased amount of bridging thiol groups, which tend to pull shell Au atoms away from the core.[70] On the other hand, the CN vs. shell $n_{Au} \ n_S^{-1}$ ratio linear trend has a negative slope compared to the shell-to-core BE vs. $n_{Au} \ n_S^{-1}$ ratio linear trend. This fact explains why the shell-to-core BE was found to counterintuitively increase as the average core CN increases. This observation was made based on the Au to SR stoichiometry in only the shells of the MNCs. Examining the total Au to SR ratio on the entire MNC, we note an overall agreement with the experimental observation of increasing MNC diameter resulting from increasing Au to SR ratio in solution.[93]

In Figure 2.4(d) we show the gas phase CE vs $n_c^{-1/3}$ trend for the Au_nSR_m core structures (without the presence of the shells) identified from the crystal structures of the experimentally synthesized MNCs (black rectangles) and compare against the CE behavior of the global minimum energy gas phase Au MNC structures of the same size range (red circles). Interestingly, the gas phase CE (Equation 2.3) is roughly equivalent to the core CE calculated with the presence of the shells in the MNCs (see Equation 2.2 and Figure B6). Therefore, the gas phase CEs of the MNC cores accurately represents the stability of the cores in the MNC (presence of shell), and can be directly compared with the gas phase global minimum energy structures, as in Figure 2.4(d). The initial structures of the global minimum gas phase clusters were taken from recent literature and were relaxed at the same level of theory as the MNC cores.[94, 95, 96] Figure 2.4(d) reveals a difference in the slopes between the minimum energy MNCs and the core nanocluster structures. The difference in slopes can be attributed to the morphology imposed on the Au MNC cores by the presence of the thi-
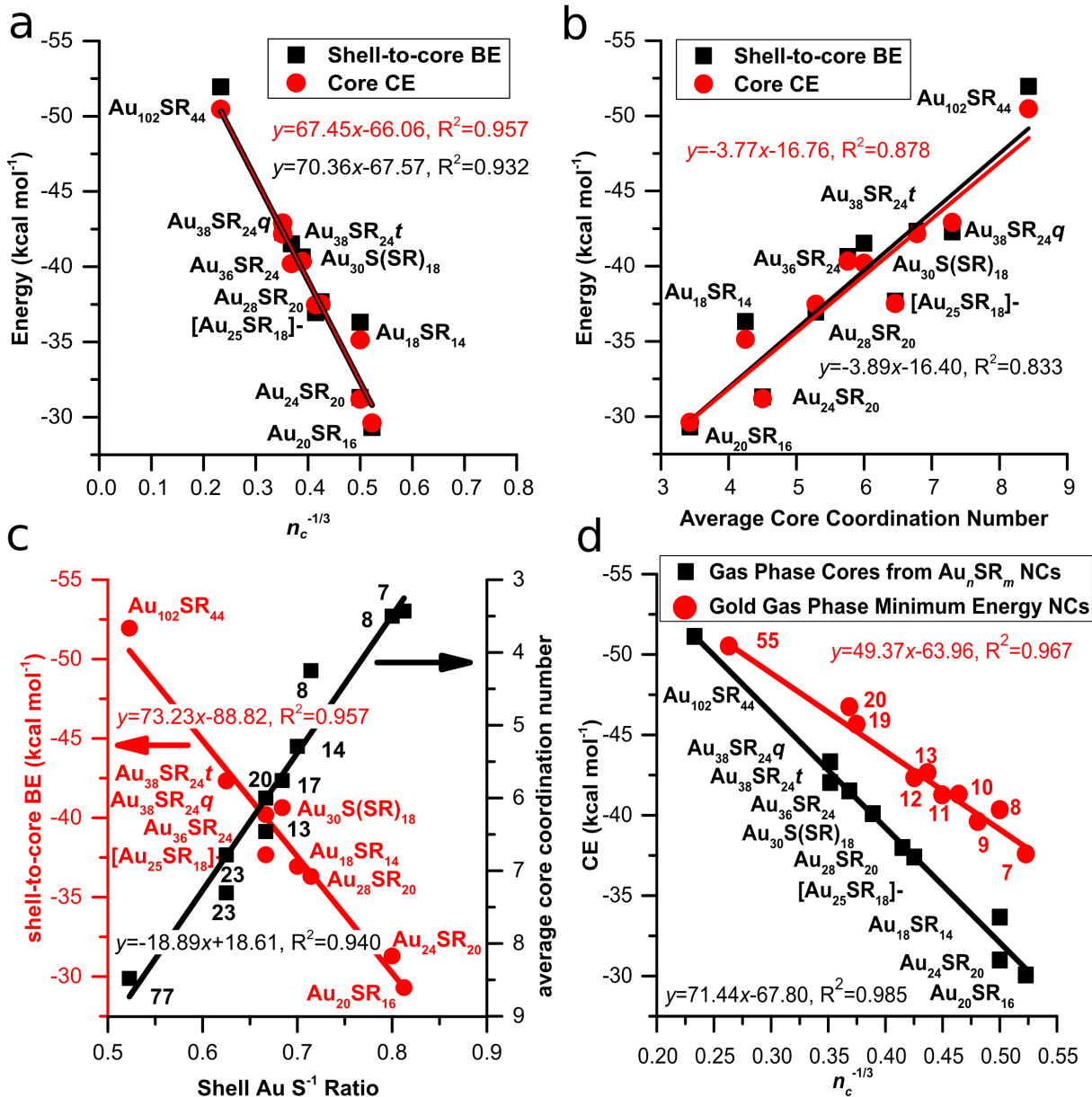
Figure 2.4: MNC stability-morphology relations. (a) Core CE and shell-to core BE vs. $n_c^{-1/3}$ (number of core metal atoms) for cores of thermodynamically stable magic number Au MNCs (b) Core CE and shell-to-core BE vs. average coordination numbers (CNs) for cores of Au nanoclusters (c) Shell-to-core BE and average core CN vs. the ratio of total Au atoms and S atoms in the shells and (d) Global minima gas phase Au clusters and cores of Au MNCs. From Figures 2.1 and 2.2, the Au MNC cores contain: $Au_{18}SR_{14}=8$, $Au_{20}SR_{16}=7$, $Au_{24}SR_{20}=8$, $[Au_{25}SR_{18}]^-=13$, $Au_{28}SR_{14}=14$, $Au_{30}S(SR)_{18}=17$, $Au_{36}SR_{24}=20$, $Au_{38}SR_{24}q,t=23$, and $Au_{102}SR_{44}=77$ Au atoms, respectively.

olate shell. Notice that gas phase minimum energy Au clusters preferentially obtain planar structures up to Au_{13}, whereas, in the presence of the metal-thiolate shell, they obtain 3-dimentional structures.[94, 97] We believe that other magic-number thiolated Au MNC cores will fall directly on the black line. Overall, Figure 2.4 demonstrates for the first time that the stabilization of colloidal MNCs in solution is dictated by two thermodynamic descriptors that need to balance: the metal core of the MNC tends to grow to increase the CE with MNC size (descriptor: CE), while the thiolate-Au network on the shell (acting as adsorbates) obtains a specific composition in staple motifs ($n_{Au} \, n_S^{-1}$ ratio), tuning the shell-to-core BE to match the CE of the core at each MNC size.

Moving forward, using these relations discovered in Figure 2.4, additional stoichiometry rules are needed (i.e. $Au_n(SR)_m$ stoichiometries in addition to core and shell information) to construct a useful methodology for MNC prediction. Toward stoichiometry prediction, previous work identified a geometric descriptor based on the surface area to volume ratio of the MNCs that relates the number of ligands (m) to the total number of Au atoms (n) in the MNCs with a linear trend of m vs. $n^{2/3}$.[34] For the MNCs $n \approx n_c + n_{ShellInt}$ (very small deviations can occur when a shell Au does not bind the core, or a S atom is a direct contact to the core). Given that $n_{ShellInt} \approx n - n_c$ and the Au S^{-1} ratio in the shell dictates a linear trend with shell-to-core BE (Figure 2.4(a)) we would expect m and $n_{ShellInt}$ to be correlated. The inset of Figure 2.5(a) shows that m scales perfectly linearly with $n_{ShellInt}$ (R^2=0.967).

Since m and $n_{ShellInt}$, and m and $n^{2/3}$, are linearly related and since $n_c \approx n - n_{ShellInt}$, a 2/3 exponential relationship (predominates linear functionality) also exists between n_c and m (Figure 2.5(a)). As a result, these observations establish a parametric model for n and m founded on n_c. This parametric model, which can now predict the overall MNC stoichiometry, is presented in Figure 2.5(b). We have thus shown (using the relations derived from Figure 2.4) that the core morphology largely dictates the overall MNC characteristics. Along these lines, our new model captures the previously identified m vs. $n^{2/3}$ behavior and nearly all of the MNCs fall within the 95% prediction intervals. Because this model is parametric with n_c, however, specific core and shell region information can be immediately derived for MNCs of any given n,m. For example, given n_c=45, $m \approx 32 - 34$ and $n_{ShellInt} \approx 19 - 20$ resulting in the $Au_{64}(SR)_{32}$, $Au_{65}SR_{34}$, and any other combination between these
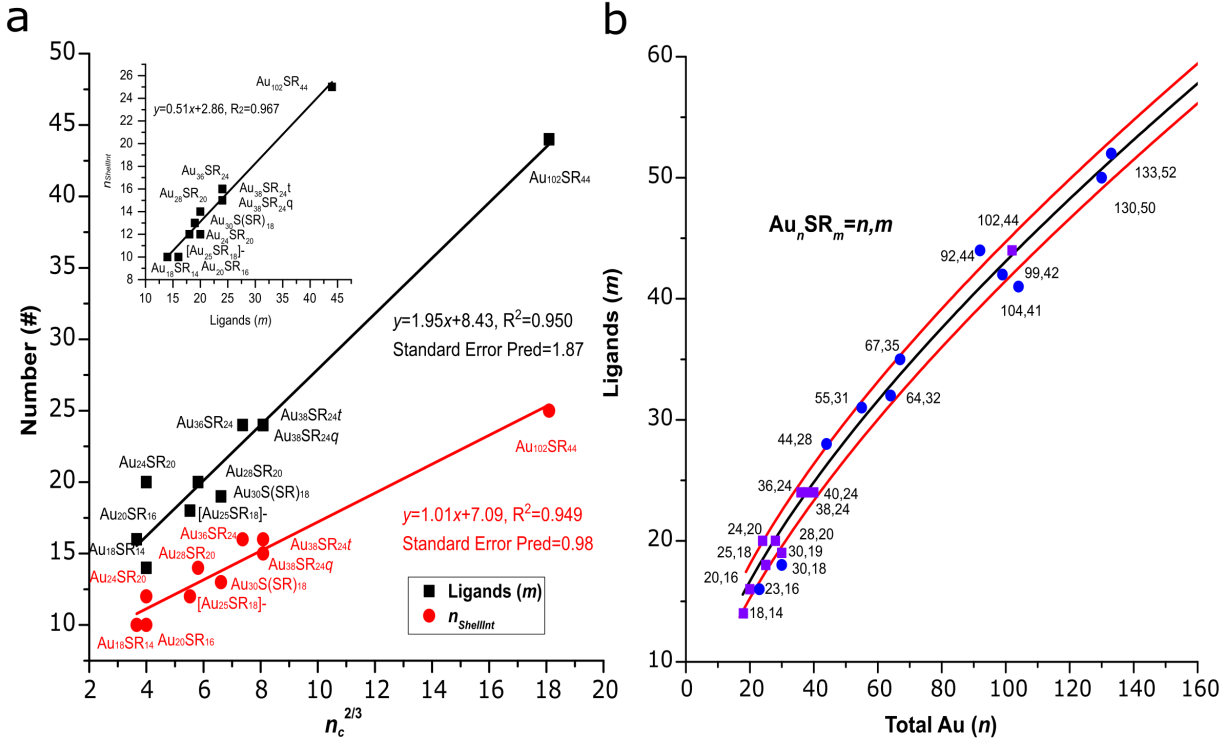
Figure 2.5: Stoichiometry relations in MNCs. (a) Number of Ligands (m) and $n_{ShellInt}$ vs. $n_c^{2/3}$ for all MNCs of Figure 2.4. The inset graph shows the $n_{ShellInt}$ vs. m behavior. (b) Predicted stoichiometric trend between Number of Ligands (m) and Total Au (n) atoms of the MNCs. The predictions were made using the relations shown in (a). The black line represents the best fit, whereas, the surrounding red lines the standard error in the prediction. The purple square points represent experimentally accessible MNCs used in our calculations to develop the TSM, whereas, the blue circles represent other experimentally accessible MNCs identified in literature.

n,m vales to identify MNCs (see Figure 2.5(b) for experimentally synthesized $Au_{64}(SR)_{32}$ MNC). From this point, the structure-energy relationships identified in Figure 2.4 can be used to feed structural information to the MNC prediction (e.g. core CN) as well as to screen candidate structures on the energy balance criterion between the core CE and the shell-to-core BE (see Figure 2.2). Thus, the identified relationships aid the prediction of MNCs that span sizes larger than the ones currently affordable by high-throughput DFT calculations.

2.3 Conclusions

In this chapter we developed a thermodynamic stability theory (TSM) derived from first-principles calculations, rationalizing the stability of colloidal metal MNCs in solution and significantly advancing the previously proposed divide-and-protect and superatom theories.[21, 19] Our theory reveals that for every thermodynamically-isolated, experimentally synthesized thiolate-protected MNC, there is a perfect energy balance between the adsorption strength of the ligand-shell to the metal-core and the cohesive energy of the core. Our theory applies to both neutral and charged MNCs, as well as to different metals. Additionally, we highlight the impact of the thiolate ligands on the overall stability and size/shape of the MNC.[16] Finally, this theory directly relates these thermodynamic stability (energy) contributions to geometrical characteristics of metal cores of the MNC, rationalizing MNC size and shape effects on MNC stability and opening new avenues for in-silico MNC predictions.

3.0   Understanding Targeted Transformations of MNCS

The content of this chapter is taken from:

- From/or modified from Q. Li, T.-y. Luo, M. G. Taylor, S. Wang, X. Zhu, Y. Song, G. Mpourmpakis, N. L. Rosi, and R. Jin, "Molecular "Surgery" on a 23-gold-atom Nanoparticle," *Science Advances*, vol. 3, no. 5, p. e1603193, 2017. ©The Authors, some rights reserved; exclusive licensee American Association for the Advancement of Science. Distributed under a Creative Commons Attribution NonCommercial License 4.0 (CC BY-NC) http://creativecommons.org/licenses/by-nc/4.0/.

- Taken in part from Q. Li, M. G. Taylor, K. Kirschbaum, K. J. Lambright, X. Zhu, G. Mpourmpakis, and R. Jin, "Site-selective Substitution of Gold Atoms in the $Au_{24}(SR)_{20}$ Nanocluster by Silver," Journal of Colloid and Interface Science, vol. 505, no. 1 Nov 2017, pp. 1202– 1207, 2017.

- Reprinted (adapted) with permission from Q. Li, K. J. Lambright, M. G. Taylor, K. Kirschbaum, T.-Y. Luo, J. Zhao, G. Mpourm- pakis, S. Mokashi-Punekar, N. L. Rosi, and R. Jin, "Reconstructing the Surface of Gold Nanoclusters by Cadmium Doping," *Journal of the American Chemical Society*, vol. 139, no. 49, pp. 17779–17782, 2017. Copyright 2017 American Chemical Society.

3.1   Computational Methods

In this work we used DFT and free energy calculations to study targeted metal doping and MNC transformation phenomena. We used the BP-86[51, 52] functional combined with the def2-SV(P) basis set[53] accelerated with the resolution of identities (RI) approximation[54, 55] as implemented in the Turbomole package. Gibbs free energies were calculated using the harmonic oscillator approach applied to the vibrational modes calculated over the entire MNCs at 298.15 K. The $[Au_{23}(SR)_{16}]^-$ and $[Au_{25}(SR)_{18}]^-$ structures were taken from previously published crystallographic information and the R groups of the thio-

Table 3.1: Example reactions (using $[Au_{23}(SR)_{16}]^-$) for MNC doping and transformation.

Reaction Type	Reaction Expression
Motif Exchange	$[Au_{23}(SR)_{16}]^- + 2(AuCl)_2PPh_2CPPh_2 \rightarrow Au_4(SR)_4 + [Au_{21}(SR)_{12}(Ph_2PCH_2PPh_2)_2(AuCl_2)_2]^-$
Ag Doping	$[Au_{23}(SR)_{16}]^- + \frac{1}{4}Ag_4(SR)_4 \rightarrow [Au_{22}Ag(SR)_{16}]^- + \frac{1}{4}Au_4(SR)_4$
Au Growth	$[Au_{23}(SR)_{16}]^- + \frac{1}{2}Au_4(SR)_4 \rightarrow [Au_{25}(SR)_{18}]^-$
Ag Growth	$[Au_{23}(SR)_{16}]^- + \frac{1}{2}Ag_4(SR)_4 \rightarrow [Au_{23}Ag_2(SR)_{18}]^-$

lates were substituted by methyl groups and the positive counterions were removed to maintain consistent charge states.[60, 101] The structure of the $[Au_{21}(SR)_{12}(P-C-P)_2(AgCl_2)]^-$ was taken from XRD results [98] and the R groups $(-C_6H_{11})$ of the thiolates were substituted for (-CH$_3$). From the relaxed $[Au_{23}(SR)_{16}]^-$ MNC, Au atoms were substituted for Ag atoms in each location and up to 4 Ag total in the locations highlighted in Figure C1. The $Au_{24-x}Ag_x(TBBM)_{20}(x \approx 1)$ [99] and $[Au_{19}Cd_2(SR)_{16}]^-$ [100] structures were taken from XRD, with (-CH$_3$) substituting the R groups. For the $[Au_{19}Cd_2(SR)_{16}]^-$ structural MNCs, all calculations with system charge imposed such that electronic shell closure was achieved and, when possible, matched experiments. Tetramers (M_4SR_4) were used as a reference for the growth and doping reactions for the M$_1$SR complexes (M=Au or Ag), since these tetramers have previously been shown to be highly thermodynamically stable.[92] A summary of example reactions used to model the Gibbs free energy of each type of MNC transformation are shown in Table 3.1. We also introduce a geometric displacement vector to capture MNC rearrangement in Equation 3.1.

$$\delta = \frac{\sum_{i=1}^{N_{atoms}}\sqrt{(x_{i,final} - x_{i,initial})^2 + (y_{i,final} - y_{i,inital})^2 + (z_{i,final} - z_{i,initial})^2}}{N_{atoms}} \tag{3.1}$$

where N_{atoms} is the number of atoms and x, y, and z represent the spatial coordinates of the atoms in both their initial and final states.

3.2 Results and Discussion

3.2.1 Molecular "surgery" on a 23-gold-atom MNC

With single crystal XRD experiments, Ag doping and MNC transformations were observed by the group of Professor Rongchao Jin at Carnegie Mellon University into the $[Au_{23}(SR)_{16}]^-$ MNC as summarized in Figure 3.1.[98] Briefly, when only a small amount of Ag(SR) was added to a solution of $[Au_{23}(SR)_{16}]^-$, Ag doping was achieved to $[Au_{23-x}Ag_x(SR)_{16}]^-$ (x≈1) in two distinct locations. With the addition of more Ag(SR), the $[Au_{23-x}Ag_x(SR)_{16}]^-$ MNC transformed to a $[Au_{25-x}Ag_x(SR)_{18}]^-$ MNC. However, if a PPh_2CPPh_2 (P-C-P) ligand was added to the $[Au_{23-x}Ag_x(SR)_{16}]^-$ (x≈1) the MNC would react to form a new $[Au_{21}(SR)_{12}(P-C-P)_2]^+$ MNC. Interestingly, the pure $[Au_{23}(SR)_{16}]^-$ MNC was inert to addition of Au(SR) or (P-C-P) ligands. Overall, this experimental work presents a case of very interesting doping and ligand-induced MNC transformations are observed where theoretical understanding of these MNC transformations is needed.
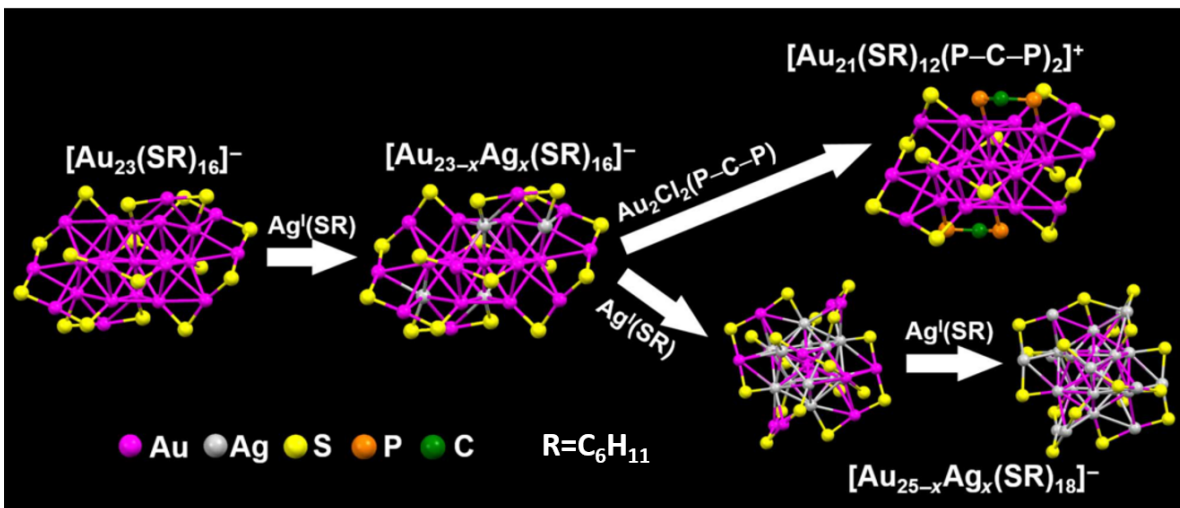
Figure 3.1: Experimentally-observed doping pathways and transformations in the $[Au_{23}(SR)_{16}]^-$ MNC.

Figure 3.2 shows our computational free energy results. First, we observe that for the $[Au_{23}(SR)_{16}]^-$ and $[Au_{22}Ag(SR)_{16}]^- MNCs$, Ag doping reactions are exothermic and slightly

24

preferred over growth reactions to form $[Au_{25-x}Ag_x(SR)_{18}]^-$ MNCs. Additionally, we see that the growth of $[Au_{23}(SR)_{16}]^-$ to $[Au_{25}(SR)_{18}]^-$ is unfavorable.
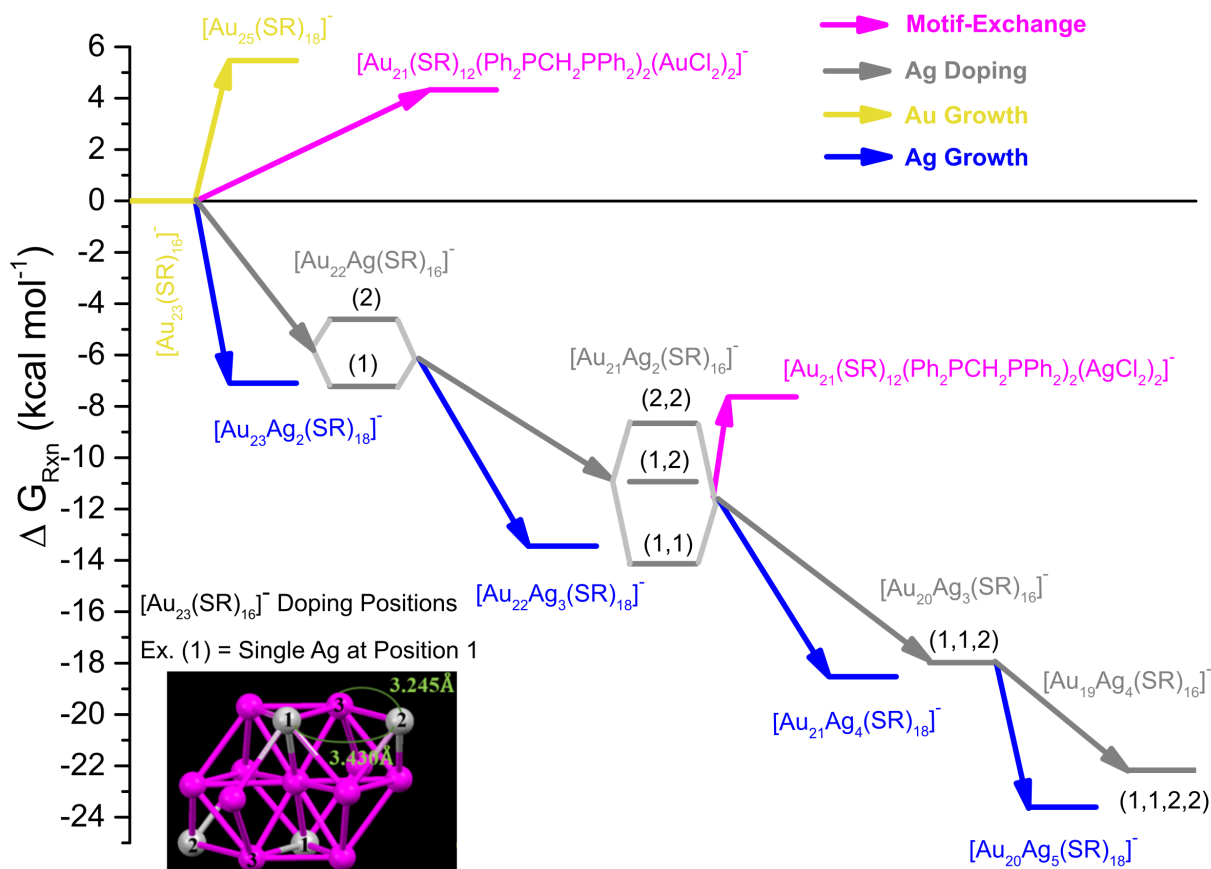
Figure 3.2: DFT-calculated free energies of reactions (ΔG_{rxn}) of the experimentally synthesized pure and Ag-doped Au MNCs. The inset picture demonstrates the different (thermodynamically stable) doping positions of Ag in the Au_{15} core of the $[Au_{23-x}Ag_x(SR)_{16}]^-$ MNC. The different energy levels of the $[Au_{23-x}Ag_x(SR)_{16}]^-$ MNCs represent the lowest-energy isomers (based on doping positions of the inset).

However, for the $[Au_{21}Ag_2(SR)_{16}]^-$ MNC, growth to $[Au_{21}Ag_4(SR)_{18}]^-$ becomes energetically more preferred than the doping step to $[Au_{20}Ag_3(SR)_{16}]^-$, rationalizing the lack of observed $[Au_{20}Ag_3(SR)_{16}]^-$, especially given the low-stoichiometric amount of Ag(SR) added. This preference in the Ag growth step over Ag doping is further enhanced in the reaction of

$[Au_{20}Ag_3(SR)_{16}]^-$ to form $[Au_{20}Ag_5(SR)_{18}]^-$ over $[Au_{19}Ag_4(SR)_{16}]^-$. This demonstrates an increasing energetic preference for growth to $[Au_{25-x}Ag_x(SR)_{18}]^-$ MNCs in agreement with the fact that further (than x=2) doped $[Au_{23-x}Ag_x(SR)_{16}]^-$ are not observed. Next, we observe a significantly uphill thermodynamic reaction between the $Au_2Cl_2(PPh_2CPPh_2)$ and the $[Au_{23}(SR)_{16}]^-$ to form the $[Au_{21}(SR)_{12}(Ph_2PCH_2PPh_2)_2(AuCl_2)_2]^-$ MNC (representing motif-exchange reactions). However, we see light doping of Ag into the $[Au_{23}(SR)_{16}]^-$ opens a now-exothermic path to $[Au_{21}(SR)_{12}(Ph_2PCH_2PPh_2)_2(AuCl_2)_2]^-$, enabling the (P-C-P) transformation from an initial $[Au_{23}(SR)_{16}]^-$. It should be noticed that all these theoretical findings are in perfect agreement with the experimental observations, demonstrating that a thermodynamics (free energy) analysis can capture the growth behavior of these MNCs (at least for the systems of interest).

3.2.2 Site-selective substitution of Au by Ag in the $Au_{24}(SR)_{20}$ MNC.

Though the free energy analysis used in tracking the Ag doping in the $[Au_{23-x}Ag_x(SR)_{16}]^-$ MNC was promising, it did little to reveal any underpinning physics for why the doping was preferred at the specific locations observed. To start to address this question we first studied Ag doping within the $Au_{24}(SR)_{20}$ MNC. Experimentally, it was shown that ligand exchange on the lightly doped $[Au_{23-x}Ag_x(SR)_{16}]^-$ transformed the MNC to a lightly doped $Au_{24}(SR)_{20}$ MNC.[99] Interestingly, only three Ag locations were observed in the XRD single crystal analysis. To study doping within this $Au_{24}(SR)_{20}$ MNC, we looked at free energy of doping utilizing an Ag doping reaction as in 3.1. Beyond this, we compared the NBO charge [71] of Au atoms at specific locations with the doped Ag atoms at the same locations (ΔCharge) to see if charge transfer to Ag might play a role in determining preferred dopant location.

After substituting the full ligands for methyls and performing Gibbs free energy analysis on the preference of doping Ag into various positions within the $Au_{24}(SR)_{20}$ framework, we verified that the lowest-energy doping locations correspond to the positions observed in the experiments (see Figure 3.3). Upon examining the NBO charges of the Ag atoms when doped in the MNC versus the equivalent Au charges within the $Au_{24}(SR)_{20}$, we find that the
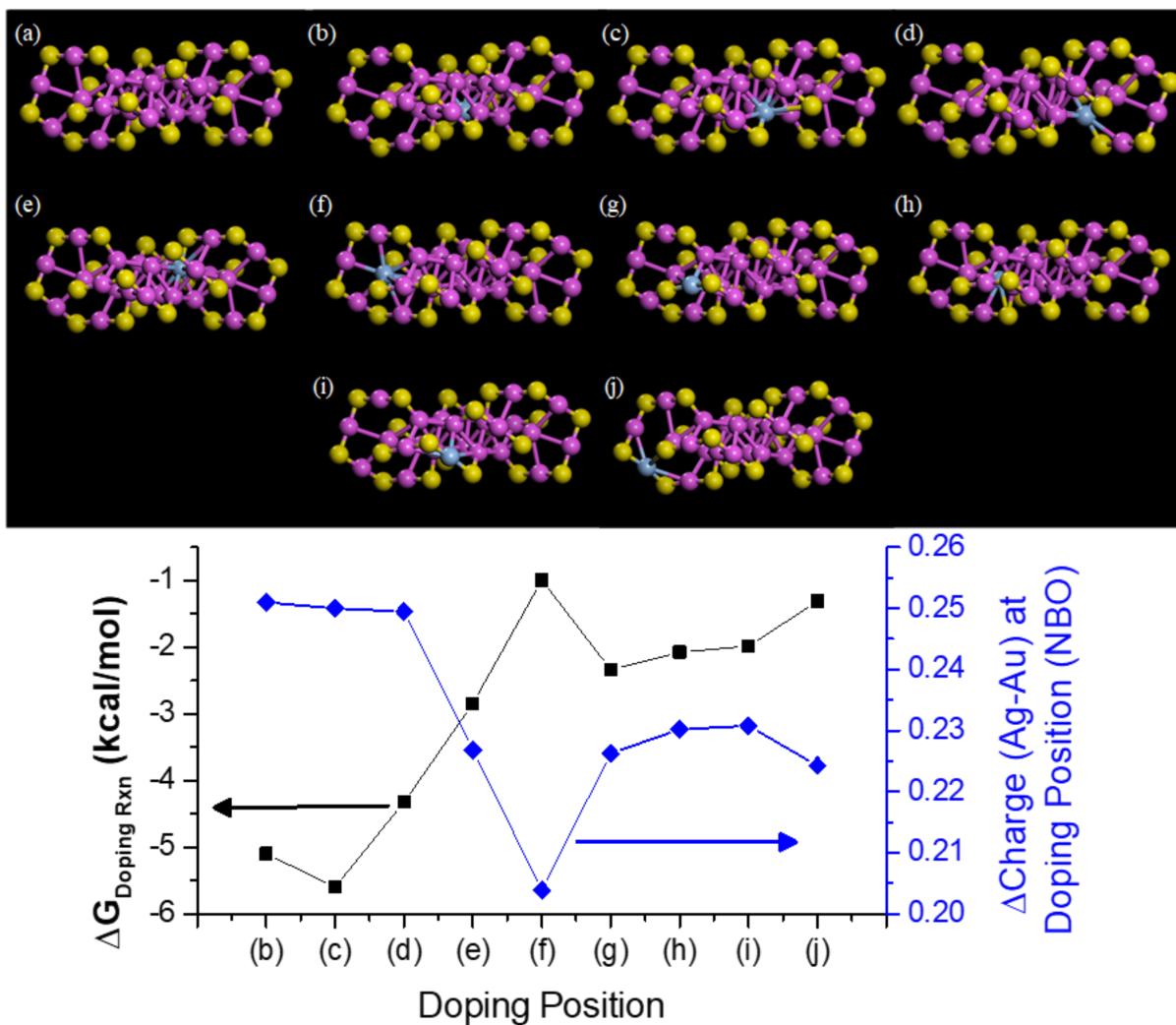
Figure 3.3: Upper: (a) $Au_{24}(SCH_3)_{20}$ and (b)-(d) experimental doping locations; (e)-(j) non-experimental dopant positions for Ag atoms tested via DFT in the $Au_{23}Ag(SCH_3)_{20}$ MNC. The $-CH_3$ groups have been removed for clarity. Lower: Free Energies of doping reactions and ΔCharge (NBO) on between Ag atoms in locations of doping (upper) and the equivalent-position Aus within the $Au_{24}(SCH_3)_{20}$ MNC.

27

locations that are lowest in energy impart a nearly identical change in NBO charge on the Ag atoms when doped into the framework. The other doping locations (Figure 3.3), however, impose a lower charge state change than the three experimental locations. Therefore, we suggest the doping location is directly tied with relative charge transfer between Ag and the rest of the MNC when it is doped into the MNC. The larger the charge transfer, the more electrostatic interactions likely occur between the dopant and the surrounding MNC, lowering the overall energy of the doped MNC. Thus, we have explained why the experimental doping locations are observed using DFT and suggest that targeted charge analysis can aid in screening doping locations of other metals into MNCs.

3.2.3   Reconstructing the Surface of Au MNCs by Cd Doping.

Experimentally, the $[Au_{19}Cd_2(SR)_{16}]^-$ (representing a doped MNC with no Au MNC analog, unique in literature) was synthesized.[100] This $[Au_{19}Cd_2(SR)_{16}]^-$ was also interesting in that it featured two Cd dopants tri-coordinated with sulfur, which has never been observed in any other doped Au MNC. Here, we focused on developing better understanding on the unique dopant locations of the $[Au_{19}Cd_2(SR)_{16}]^-$ MNC. Figure 3.4 shows the calculated structural and electronic characteristics as well as the energy preference of various $[Au_{19}Cd_2(SR)_{16}]^-$ isomers, where the first Cd atom is placed on the experimentally determined position and the second Cd is placed on one of the remaining metal positions of the cluster.

First, we note that over geometry relaxation the $[Au_{19}Cd_2(SR)_{16}]^-$ MNC with the Cd dopants at the experimental positions (labeled 9 in Figure 3.4 A) is a stable MNC with little geometric displacement (δ). However, when this $[Au_{19}Cd_2(SR)_{16}]^-$ MNC has just one of the Cd positions shifted, in most cases the cluster becomes unstable under relaxation, displaying significant geometric displacement (δ), cases (1) – (8), see Figure 3.4(b). Furthermore, the two additional doping positions that do not displace, (10) and (11), are of higher Gibbs Free Energy (approximately $+65$ kJ/mol, Figure 3.4(b)) than the experimentally-determined doping position (9), highlighting the unique preference of Cd doping locations in this MNC. For comparison, the energetic difference between Ag doping locations within the $[Au_{23}(SR)_{16}]^-$
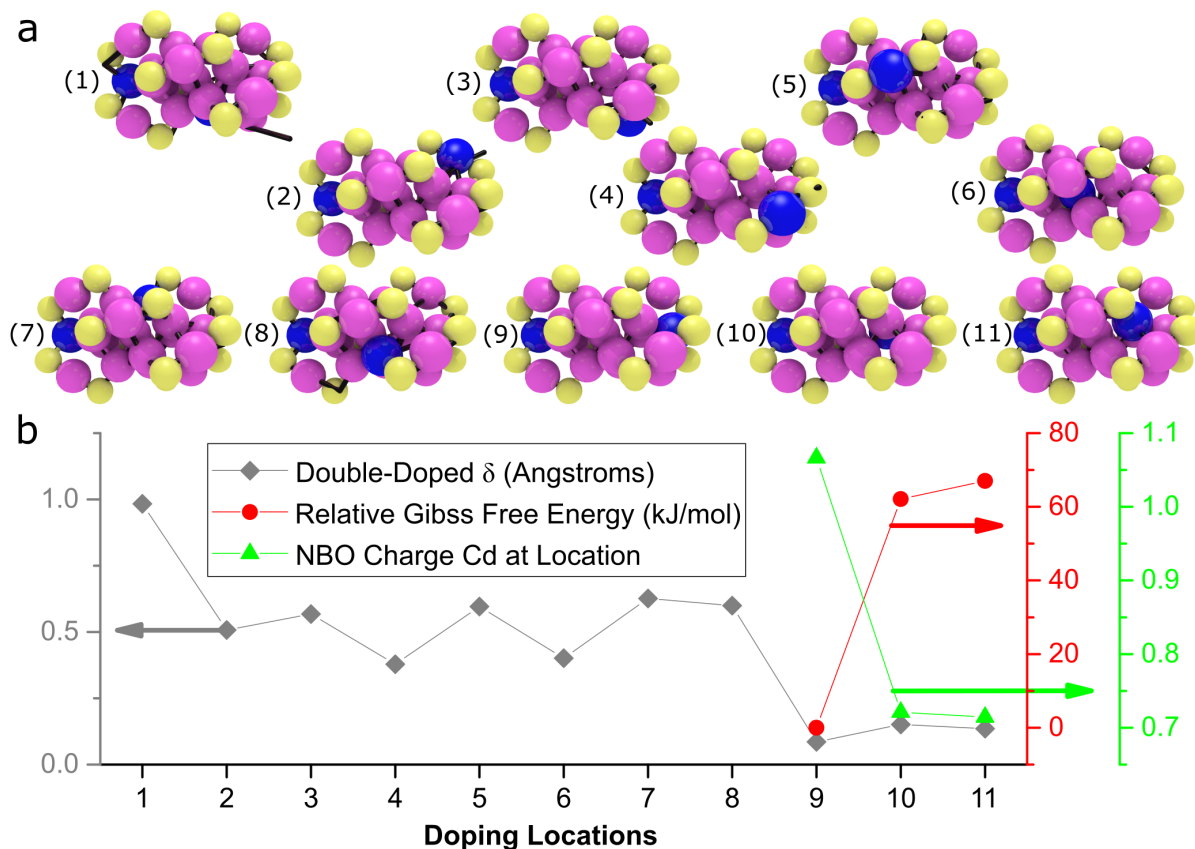
Figure 3.4: DFT results for $[Au_{19}Cd_2(SR)_{16}]^-$ with Cd dopants shifted to different locations where doping location (9) represents the experimentally observed structure. (a) Experimental nanocluster geometries before ('ball and stick') and after (black sticks) geometry relaxation. In the 'ball and stick' representations, Magenta=Au; Blue=Cd; and Yellow=S. All C and H atoms are omitted for clarity. (b) Doping locations compared to geometric rearrangement, Gibbs free energy, and NBO charge. For clusters with $> 0.2\mathring{A}$, the free energies and NBO charges have been omitted due to their geometric reconstruction.

MNC previously reported [98] were closer to +10 kJ/mol. For the three doping positions (9, 10, and 11) that did not displace (in Figure 3.4), the charge state of the dopants trends exactly with the energetic preference of the dopants in these positions, as observed in our previous study of Ag doping into the $Au_{24}(SR)_{20}$ MNC.[99] Taken together, the DFT results suggest that the presence of this unique "paw-like" surface motif formed in the presence of Cd, makes back-replacement of Cd with Au unfavorable.

Additionally, when only either one or both Cd atoms are replaced with Au in the $[Au_{19}Cd_2(SR)_{16}]^-$ MNC framework, the MNC reconstructs, regardless of the dopant position (see Figure C2). To our knowledge this is the first observation of a doped nanocluster structure that is independent of an analogous pure Au cluster and is likely due to the presence of the unique "paw" surface motif introduced by the presence of Cd. These observations help rationalize the formation of this new surface motif and MNC compared to other MNCs produced from doping the $[Au_{23}(SR)_{16}]^-$ MNC in Section 3.2.1. [98]

3.3   Conclusions

In this chapter we highlighted three examples of targeted doping and MNC transformation and how DFT was used to gain deeper understanding into how and why the doping and transformations occurred. Specifically, we used free energy analysis to study MNC transformations in $[Au_{23}(SR)_{16}]^-$ MNC that perfectly matched theoretical results directly to experiments, rationalizing both dopant locations and concentrations. We also used free energy and charge analysis to study doping in $Au_{24}(SCH_3)_{20}$ MNC, capturing dopant location preference through dopant charge transfer trends. Finally, we studied the unique stability of tri-coordinated Cd atom in the $[Au_{19}Cd_2(SR)_{16}]^-$ MNC, and its lack of a pure Au structural analog. For the $[Au_{19}Cd_2(SR)_{16}]^-$ MNC we introduced the geometric displacement vector (δ) from DFT relaxations as a measure of MNC rearrangement that helps identify synthetically inaccessible MNCs. We also verified dopant NBO charge transfer again trends with doping preference at specific locations. Overall, we have demonstrated three targeted MNC transformation cases and ways of understanding their physical underpinnings.

4.0   Heterometal Doping in Ligand-Protected MNCs

Reprinted (adapted) with permission from M. G. Taylor and G. Mpourmpakis, "Rethinking Heterometal Doping in Ligand-Protected Metal Nanoclusters," *Journal of Physical Chemistry Letters*, vol. 9, pp. 6773–6778, 2018. Copyright 2018 American Chemical Society.

4.1   Computational Methods

The thermodynamic stability model (TSM) that was applied is largely the same as outlined in Section 2. To capture doping, we first relaxed the $[Au_{25}(SC_2H_4Ph)_{18}]^-$ [60] (Au_{25}) and $Au_{38}(SC_2H_4Ph)_{18}$ [78] (Au38q) MNCs as found from their experimental crystal structures. From the relaxed forms of the Au MNC we doped each position and fully re-relaxed the doped MNC structures to find the final structures as reported in Figure D2. To most directly compare our results with experiments, the doped-MNC charges were also assigned based on experimentally-observed charge states.[9] Assignment of (q=-1) charges on the core/shell region was also applied as in Section B where the electron affinities (EAs) of the core and shell regions were calculated and all the shell regions showed higher EAs (stabilization of electron on the shell). To ensure the lowest energy electronic state was selected for the core and shell regions, we tested all applicable multiplicities lower than 14 for every core and shell structure. We also quantified reconstruction in the cores, using displacement as defined in Equation 3.1 over the core of the Au_{25} MNC as indicated and n represents the total number of atoms in the core structures. After quantifying reconstruction, we applied the TSM by calculating the core CE and shell-to core BE (see Equation 2.1) terms to capture the chemical potentials of both the core and shell regions. For doped MNCs, the core CE is calculated slightly different than Equation 2.2 as:

$$Core\,CE = \frac{(E_{FullCluster} - \sum_{i=1}^{n_c} E_{MetalAtom,i}) - E_{Shell}}{n_c + n_{ShellInt}} \qquad (4.1)$$

where E_x = electronic energy of species X, and all other definitions are identical to Equation 2.2. Note that in bimetallic MNCs, each individual metal atom identity must be taken into account to calculate the Core CE.

4.2 Results and Discussion

4.2.1 Full Ligand TSM Extension

We first applied the TSM on monometallic fully-ligated systems, rationalizing the stability of the experimental $Au_{18}(SC_6H_{11})_{14}$,[1] $Au_{24}(SCH_2PhC(CH_3)_3)_{20}$,[59] $[Au_{25}(SC_2H_4Ph)_{18}]^-$,[60] and $Au_{38}(SC_2H_4Ph)_{24}q$-isomer [78] MNCs as seen in Figure 4.1. These structures were selected since they have been successfully doped with at least one heterometal, [99, 103, 104, 46] and represent DFT-tractable fully-ligated MNCs. The $[Au_{25}(SC_2H_4Ph)_{18}]^-$ MNC, especially, has been the focus of extensive study in doping.[105] In Figure 4.2 we highlight that these full-ligand structures are all well within the previously-defined [50] 95% prediction interval (for $Au_n(SR)_m$ R=CH_3 MNCs) in a parity plot between shell-to-core BE and core CE. As there is a non-zero energetic shift in the core CE and shell-to-core BEs for methyl vs. full ligands (Figure D1), herein we treat the 95% prediction interval as an approximate boundary for the synthetic accessibility of full-ligand structures, serving more as a guide rather than as a strict cutoff for doped MNC synthesis. For example, a structure within the 95% prediction interval should be considered synthesizable, while structures that fall within 0.7 kcal mol^{-1} (See Figure D1 for justification of this number) of the 95% prediction interval may also be considered synthesizable. With this definition of synthetic accessibility for thiolate-protected MNCs within the TSM we turn to doped MNCs.

4.2.2 Heterometal Doping of Au$_{25}$ MNC

We started by doping the $[Au_{25}(SC_2H_4Ph)_{18}]^{-1}$ MNC structure (hereafter referred to as the Au_{25} MNC) to form $[Au_{25-x}M_x(SC_2H_4Ph)_{18}]^q$ with M=Ag (q = -1), Cd (q = 0), Cu (q = -1), Hg (q = 0), Pd (q = 0), and Pt (q = 0), x=1,2. These metals have all been

a

b

Au$_{18}$(SC$_6$H$_{11}$)$_{14}$

Au$_{24}$(SCH$_2$PhC(CH$_3$)$_3$)$_{20}$

c

d

[Au$_{25}$(SC$_2$H$_4$Ph)$_{18}$]$^-$
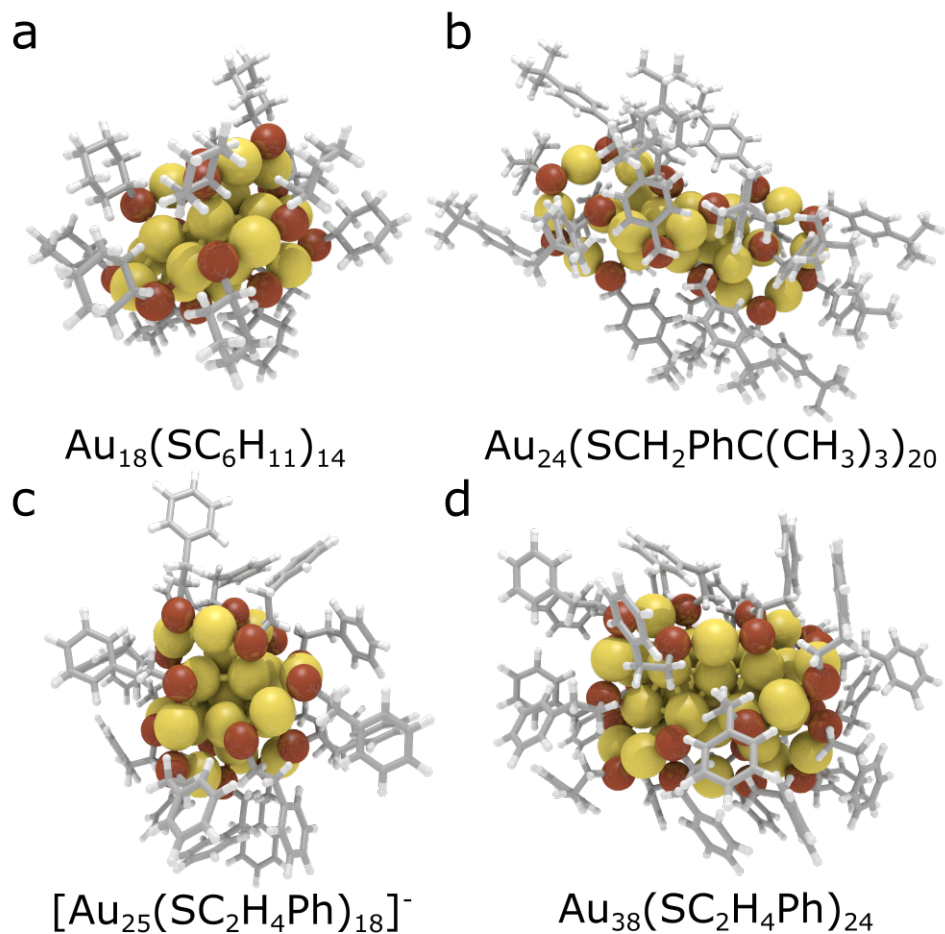
Au$_{38}$(SC$_2$H$_4$Ph)$_{24}$

Figure 4.1: DFT-relaxed structures of (a) $Au_{18}(SC_6H_{11})_{14}$ (b) $Au_{24}(SCH_2PhC(CH_3)_3)_{20}$ (c) $[Au_{25}(SC_2H_4Ph)_{18}]^-$ and (d) $Au_{38}(SC_2H_4Ph)_{24}$q-isomer. Organic ligands are shown in sticks, whereas, Au and S atoms, in yellow and brown balls, respectively.

successfully doped into the Au_{25} MNC with full $-SC_2H_4Ph$ ligands, but display distinct concentration, dopant location, and doped MNC charge (q) behavior as summarized in Table 4.1.[9] Although MNC charge behavior is an important aspect in predicting doped MNC stability,[106] here we have only run the experimentally observed charge states of each MNC for the purpose of directly comparing our calculations and the TSM to all experiments. We note that the TSM may also readily be applied to MNCs with different charge states (see Figure 2.2). To test the ability of the TSM to rationalize the synthetic accessibility of doped MNCs, we first focus on doped MNCs that have not been experimentally observed (utilizing information from Table 4.1 and Figure 4.2). In Figure 4.2 the core (C), shell (S), and icosahedron (I) distinct dopant locations within the Au_{25} MNC are shown and all metals were doped (one at a time) into each location. Based on the observed doping locations in Figure 4.2 we also tested one double-doped configuration for each metal in the Au_{25} MNC. We note that the only doped MNCs that do not fall near the 95% prediction interval on Figure 4.2 are the $Pt_{C/I}$, Hg_C, and Cu_C MNCs. Experimentally, Pt [107] has been shown to only be mono-doped to the C location in the Au_{25} MNC, so deviation from parity for the double doped $Pt_{C/I}$ MNCs aligns with the experimental observation of dopant concentration. Additionally, Cu_C falling away from parity in the TSM appears to largely align with experimental observations where either the S [108] or I [109] sites are preferred for Cu incorporation into this MNC. The Cu_C MNC has been predicted only by comparison of time-dependent DFT (TD-DFT) calculations with uv-vis spectrum, representing relatively weak evidence compared to that of the Cu_S or Cu_I MNCs (see Table 4.1). [110] Thus, all doped MNCs that deviate from the TSM in Figure 4.2 either have not been experimentally synthesized, or show weak experimental evidence compared to other MNC isomers.

Apart from the TSM shown in Figure 4.2, work in Section 3.2.3 has indicated geometric reconstruction can serve as a metric for lack of stability for doped MNC. Here, we quantify reconstruction by comparing the relaxed structures of the cores of the doped MNC structures to that of the core of the Au_{25} MNC in the displacement (δ) metric. The structures and δs of the cores of the doped MNCs are shown in Figure D2 and Table D1. From Figure D2 we highlight that the doped MNCs showing reconstruction under geometry relaxation included the Cd_{2I}, Hg_{2S}, Pd_I, Pd_S, $Pd_{C/I}$, Pt_I, and Pt_S MNCs. We note in Figure D3
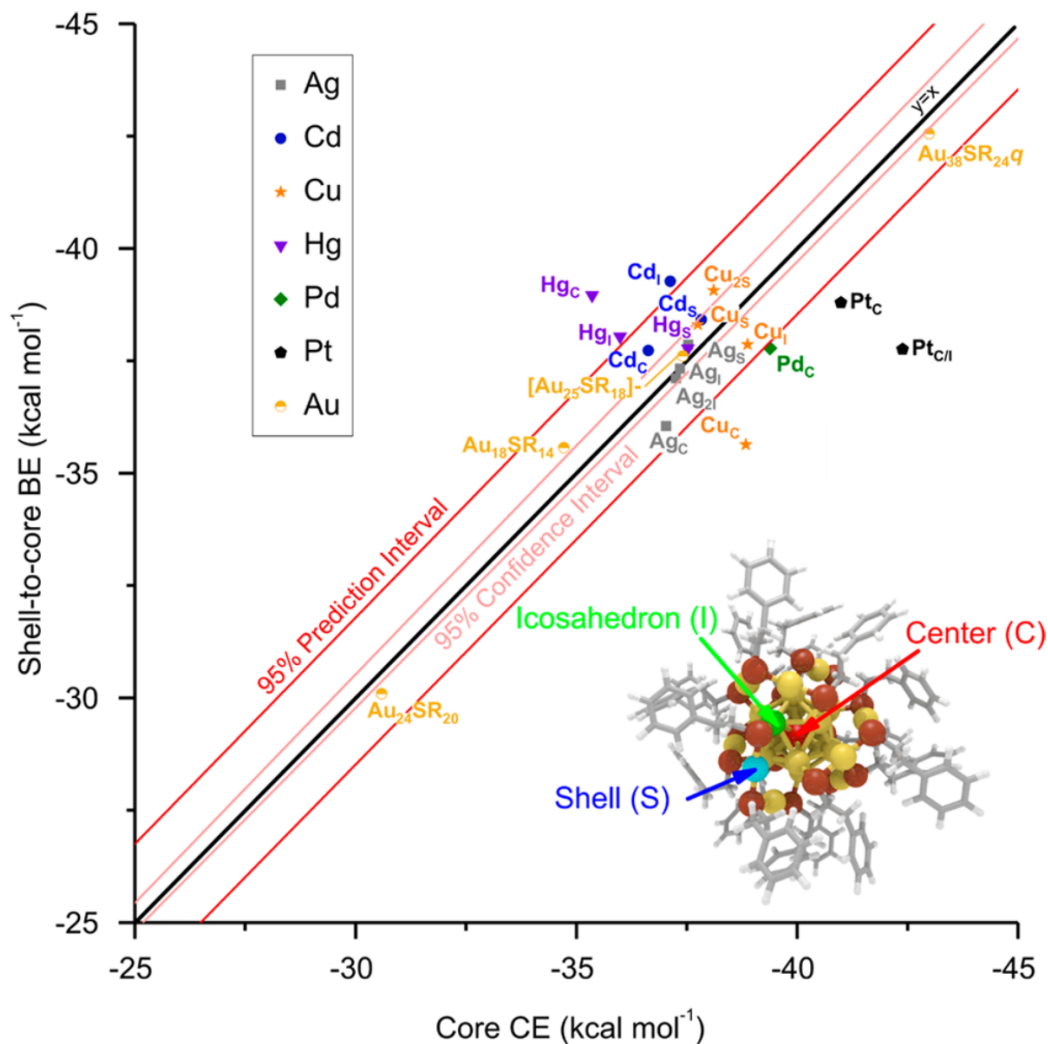
Figure 4.2: Thermodynamic stability parity plot between Shell-to-core BE and core CE on both monometallic and doped $[Au_{25-x}M_x(SC_2H_4Ph)_{18}]^q$ MNCs (x= 1,2) (M = Ag (q=-1), Cd (q=0), Cu (q=-1), Hg (q=0), Pd (q=0), and Pt (q=0)). Monometalic Au MNC structures are displayed in Figure 4.1. 95% prediction and confidence intervals displayed were generated based on previously-tested monometallic Au methyl-thiolate MNCs (Figure 2.3. The inset image shows the 3 different dopant locations (Icosahedron, I; Center, C; and Shell, S) within the Au_{25} MNC. All data points with metal labels correspond to doped $[Au_{25-x}M_x(SC_2H_4Ph)_{18}]^q$ MNCs with subscripts corresponding to the location(s) doped within the MNC. Energetics are shown only for MNCs that did not reconstruct during DFT geometry relaxation.

Table 4.1: Combined experimental doping results and locations tested for this work within the Au_{25} MNC along with experimental characterization techniques of doped MNCs.

dopant, q	locations tested	experimentally observed?	experimental methods for dopant locations
Ag, -1	I, S, C, 2I	I[111, 109], S[112], 2I[112], Up to 20Ag[112]	I/2I–XRD[111] , MALDI-MS [109] , S-XRD[112] (in heavily-doped MNC)
Cu, -1	I, S, C, 2S	I/(C)[109, 108], S[110], 2I[109], Up to 5Cu[108]	I/2I–MALDI-MS[109] , C–UV-VIS/TD-DFT[108], S-EXAFS[110]
Cd, 0	I, S, C, 2I	I[47] , C[113]	I-XRD[113] , C-XRD[47]
Hg, 0	I, S, C, 2S	S[48], C[47]	S-XRD/MALDI–MS/TGA[48], C–XRD/MALDI-MS[47]
Pd, 0	I, S, C, C/I	C[114, 35, 115]	C-MALDI-MS[114, 35] XRD[115]
Pt, 0	I, S, C, C/I	C[116, 107]	C–EXAFS/XPS[107] , MALDI-MS/NMR[116]

that although some of these reconstructed MNCs follow the TSM, they are not likely to be experimentally isolated due to further reconstruction and possible transformation to other MNCs.[112] Given Cd,[113] Hg,[48] and Pd[35] have only been successfully mono-doped into Au_{25} MNCs in experiments, δ here appears to capture lack of stability of the double-doped Cd_{2I}, Hg_{2S}, and $Pd_{C/I}$ MNCs. Additionally, both Pd[115] and Pt[107] have been shown to only occupy the C position within the MNC, indicating that δ further rationalizes why the Pt_I, Pt_S, Pd_I, and Pd_S MNCs are not observed in experiments. We therefore show the combination of the TSM with core δ during geometry relaxation to be effective for screening the potentially non-synthesizable doped MNCs.

Beyond synthetic accessibility, the TSM can also be applied to rationalize dopant location-dependent preference trends. For MNCs, such as the Pd- and Pt-doped Au_{25}, where only one doping event does not induce MNC reconstruction and the doping location energetically follows the TSM, then, the location preference assignment is trivial. For other dopants it is not as simple, and several dopant locations remain under debate in literature (in the absence of definitive single-crystal x-ray diffraction (XRD) results) as highlighted in Table 4.1. For Ag, we note in Figure 4.2 that all Ag-doped $Au_2 5$ MNCs tested did not reconstruct and fall well within the 95% prediction interval. For cases such as Ag, we propose that the distance from parity in the TSM for these MNCs can serve as a metric for dopant location preference. Thus, the Ag_I MNC is favored (XRD results) at lower doping[111] concentrations and falls closest to the parity line in Figure 4.2. The Ag_{2I} MNC also falls close to the parity line in Figure 4.2, suggesting further doping is achievable, in line with experimental observations.[109] Additionally, heavily Ag-doped MNCs showed the S-locations being occupied following the filling of the I-locations,[112] and our TSM shows (with single doping) the Ag_S MNC being the next closest to the parity line (vs. Ag_I) in Figure 4.2. Finally, the C-location doping with Ag is predicted accessible by the TSM, where in Figure 4.2 the Ag_C falls within 95% prediction interval. However, the Ag_C MNC falls much further away from the parity line than either the Ag_I or Ag_S MNCs which helps explain the experimental inaccessibility of this Au_C MNC as two other doping locations are more thermodynamically favored. Looking to dopant metals other than Ag, we note Cu was shown to likely be doped into the

S site of the MNC by extended X-ray absorption fine structure (EXAFS) analysis[110] and it falls closest to the parity line in Figure 4.2. The next closest MNC laying within the 95% prediction interval in Figure 4.2 is the Cu_{2S} MNC, and experimental doping has been observed up to 5 Cu atoms within the MNC.[108] Next, while still within the 95% prediction interval in Figure 4.2, the Cu_I has been inferred from experiments by matrix-assisted laser desorption/ionization mass spectroscopy (MALDI-MS) fragment analysis (though less definitive than EXAFS results).[109] A potential experimental verification of these results would be using electrospray ionization mass spectroscopy (ESI-MS), as this analytical technique has proven more effective in rationalizing dopant positions than MALDI-MS.[117] Finally, the Cu_C MNC is shown to fall outside the 95% prediction interval in Figure 4.2, and, as discussed above, shows relatively weaker experimental evidence.[108] Following a similar analysis as for Ag and Cu, for Hg we note that the MNC most conclusively observed in single crystal XRD was the Hg_S MNC,[48] which falls closest to the parity line of any Hg-doped Au_{25} MNCs in Figure 4.2. We note that the doping of Hg into the Au_{25} MNC gives conflicting results in experimental literature where reports of both the Hg_S[48] and Hg_C[47] exist. The study reporting Hg_C indicates difficulty in properly assigning doping location based on the XRD patterns and relies on MALDI-MS fragmentation analysis to suggest the Hg_C position.[47] However, the study reporting the Hg_S MNC appears conclusive as to the dopant location, combining XRD with MALDI-MS and thermogravimetric analysis (TGA) results. We therefore highlight the Hg_S as more prominently observed in experiments and further note that the Hg_C MNC deviates significantly from the parity in Figure 4.2. Although the Hg_I MNC is also near the 95% prediction interval (i.e. potentially synthesizable) in Figure 4.2 (unlike Hg_C that deviates), the relative proximity of the Hg_S to the parity compared to the Hg_I MNC seems to indicate stronger preference for the Hg_S MNC over the Hg_I MNCs, providing the first theoretical rationalization for the experimental observation of the Hg_S MNC. Thus, the Ag, Cu, and Hg doping results shown in Figure 4.2 (ranked by distance from the parity line) qualitatively agree with a series of experimental observations of both concentration and dopant location preference.

The doping location preferences for Cd within the MNC, though, first appear to slightly deviate from those in Table 4.1. For the Cd-doped Au_{25} MNC, all the dopant locations appear

to fall within, or near the 95% prediction interval, and therefore would all be predicted as synthesizable by the TSM. However, in XRD crystal structures of the isolated Cd-doped MNCs, only the I[118] and C[113] locations have been replaced by Cd. In Figure 4.2 We also note that the Cd_C falls closer to the parity line in Figure 4.2, and therefore suggest that Cd_I could potentially be transformed to the Cd_C MNC under appropriate experimental conditions. Additionally, although the Cd_S is not observed in these experiments it appears closest to the parity line in Figure 4.2 and does not undergo reconstruction during relaxation. This deviation of TSM from experiments, specific to Cd doping, is likely due to the high reactivity of the Cd dopant and its relative oxidation state in the Cd_S MNC. In metal exchange experiments, the Cd-doped MNC was observed to rapidly react with Hg2+ ions to form the Hg_S MNC, while the reverse reaction to form Cd_I from Hg_S was unfavorable. This indicates that the Hg_S MNC is more stable and the doped Cd is likely more reactive than the doped Hg.[113] When the doped Cd atom occupies either the C or I locations within the Au_{25} MNC framework it is likely shielded from further reactions with Au salts in solution, while the S-doped Cd atoms react with surrounding Au salts and are destroyed. Additionally, our previous work on doping within Au MNCs showed that difference in the charge of dopant and the Au atom replaced in a MNC (delta charge) can be tied to the relative dopant oxidation state and trends directly with the Gibbs free energy of formation of the doped MNC (see Section 3). In Table D2 we highlight the delta charges of all the monodoped Au_{25} MNCs, showing that the Cd delta charge in Cd_S (charge compared to the equivalent Au atom in the Au_{25} MNC) shows the largest positive charge transfer. This seems to indicate the Cd in the Cd_S is closer to an oxidized form of dopant metal than in any of the other doped MNCs, in seeming agreement that the Cd_S is highly reactive and likely chemically unstable relative to either the Cd_I or Cd_C MNCs. Taking these special considerations for Cd, the TSM captures the experimental observations of Cd doping location within the Au_{25} MNC as well.

Apart from the special case of the Cd_S MNC, the TSM captures both doping locations and concentration behavior within the Au_{25} MNC for a wide variety of metals and experimental observations. Importantly, we note that simple DFT energetics to a large extent do not capture these same trends and offer little to no insights into synthetic accessibility of doped MNCs. In Table D3 we show the relative DFT energies of the three isomers of the

mono-doped Au_{25} MNCs with each metal. By only utilizing the total DFT energies shown in Table D3 we would predict Ag to occupy the I location, Cu to occupy the C and I locations, Cd and Hg to only occupy the I location, and Pd and Pt to only occupy the C location (due to the high energy difference 10-18 kcal mol^{-1} between the ground state and other dopant positions). While Ag, Pd, and Pt doping locations are quite accurately captured by this method in comparison to experiments, the Hg, Cu, and Cd doping locations/energetics are not. Hg, for instance is predicted most stable at the I location by 10 kcal mol^{-1} and is not observed at this position in experiments. We therefore highlight the power of the TSM over simple DFT energetics for predicting and screening heterometal doping within a MNC framework. Doped MNCs which show low total energetics, but do not follow the TSM, can be viewed as intermediate structures of MNCs that will either grow in size, or change composition in a way to alter the core/shell energetics and fulfill the perfect energy balance of the TSM. We note that while experimental attempts to dope other metals (such as Ni[113] and Zn[47] in the Au_{25} MNC) have proven unsuccessful thus far, we focused here on metals that have been successfully doped into the Au_{25} MNCs and rationalize the preference on doping positions. Additionally, ligands can play a role in determining the preference of doping[112] and our results with $-CH_2CH_2Ph$ ligands may not be straightforwardly transferable to doped Au_{25} MNCs stabilized by other ligands.

4.2.3   Doping and Prediction of Au_{38} MNC

Beyond the ubiquitous Au_{25} MNC, we also tested doping within the $Au_{38-x}M_x(SR)_{24}$ (q-isomer) MNC with M=Pd (x=1,2) (q=0) and Pt (x=1 (q=-1) ,2 (q=-2)) in the locations seen in Table 4.2 and Figure 4.3. Due to the larger computational cost of the $Au_{38-x}M_x(SR)_{24}$ system (herein referred to as the $Au_{38}q$ MNC) we did not exhaustively test all doping locations, but focused on the ones that were shown to remain rigid in previous theoretical work.[49] Focusing first on the Pd-doped MNCs, we see that only one of the MNCs falls outside the "synthesizable regime", which is the Pd_{2C} MNC. In Table 4.2 we see that DFT[37, 119] has previously predicted the Pd_{2C} to be the most stable structure. However, another experimental work showed evidence of Pd-S bonds in EXAFS analysis,[49] leading them to conclude the

40
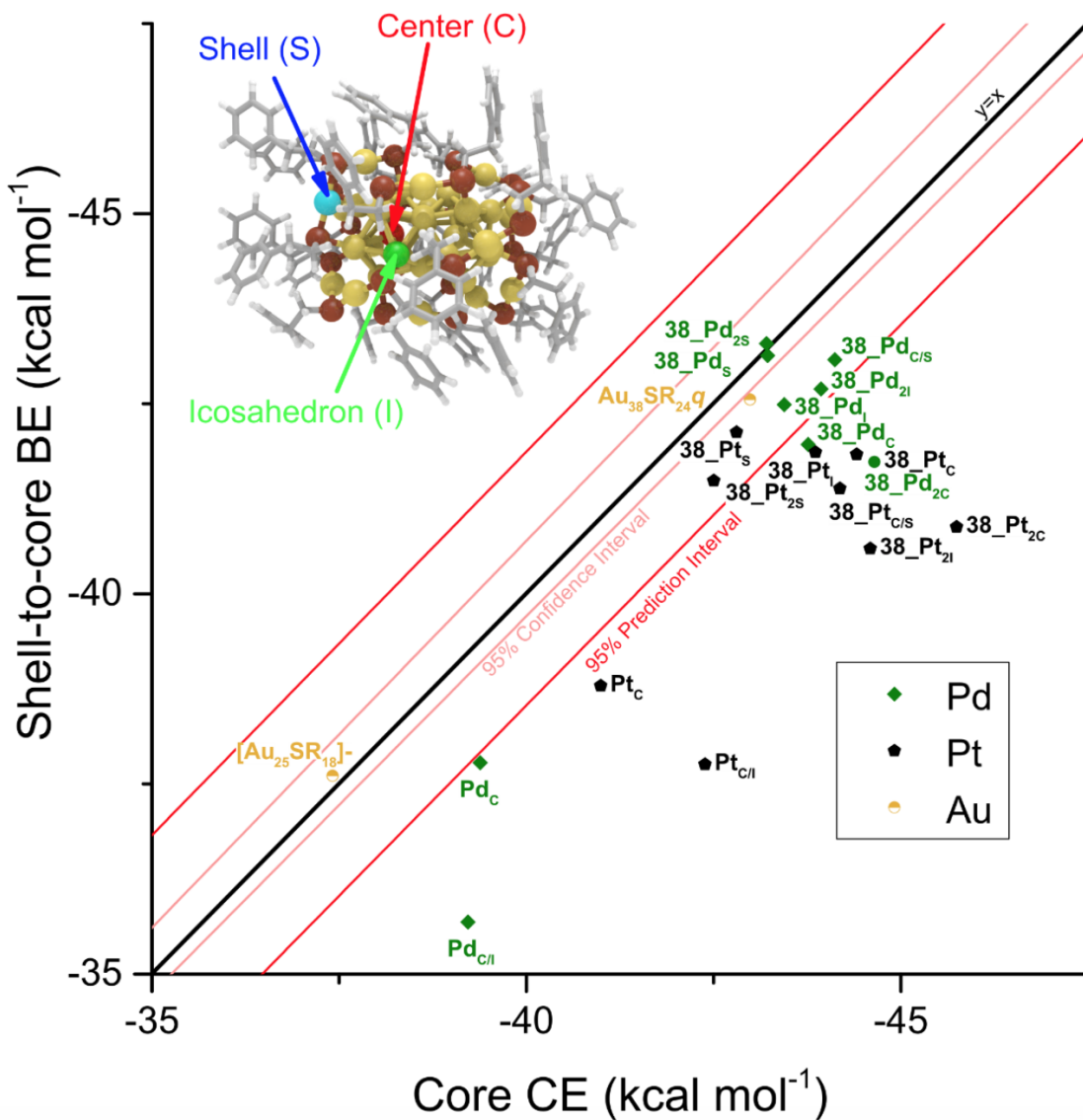
Figure 4.3: Thermodynamic stability parity plot between Shell-to-core BE and core CE on both monometallic and doped $[Au_{38-x}M_x(SC_2H_4Ph)_{24}]^q$ MNCs (x= 1,2) (M = Pd (q=0), and Pt (q=-1, -2)). Monometallic Au MNC structures are displayed in Figure 4.1. 95% prediction and confidence intervals displayed were generated based on previously-tested monometallic Au methyl-thiolate MNCs (Figure 2.3). The inset image shows the 3 different dopant locations (Icosahedron, I; Center, C; and Shell, S) within the $Au_{38}a$ MNC. All data points with metal labels beginning with 38 correspond to doped $[Au_{38-x}M_x(SC_2H_4Ph)_{24}]^q$ MNCs with subscripts corresponding to the location(s) doped within the MNC. None of these MNCs showed reconstruction during relaxation with DFT.

Table 4.2: Combined experimental doping results and locations tested for this work within the $Au_{38}q$ MNC along with experimental characterization techniques of doped MNCs.

dopant, q	locations tested	experimentally observed?	experimental methods for dopant locations
Pd, 0	I, S, C, 2I, 2S, 2C, C/S	2C[37, 119], C/S[49]	2C-DFT-Suggested[37, 119] C/S-EXAFS[49]
Pt, 0	I, S, C	——	——
Pt, -1	2I, 2S, 2C, C/S	2C[119]	2C-XPS[119]

actual structure was largely comprised of either the Pd_{2S} or $Pd_{C/S}$ MNCs. Pd_{2S} and $Pd_{C/S}$ both also match the results suggested by the TSM in Figure 4.3, where the Pd_{2S} MNC falls closest to the parity line and the $Pd_{C/S}$ MNC is next closest of the double doped MNCs. Based on the results from the TSM, we suggest, along with previous authors,[49] that the Pd is located at the S site of the Pd-doped $Au_{38}q$ MNC, distinct from the Pd-doped Au_{25} MNC, where the heterometal Pd is definitively doped in the C location. Finally, we turn to the Pt-doped $Au_{38}q$ MNC. This MNC was recently reported[119] to have a q=-2 charge and the authors utilized DFT and X-ray photoelectron spectroscopy (XPS) analysis to conclude that the only Pt dopant location within the $Au_{38}q$ MNC would be the Pt_{2C} MNC. In the absence of a more conclusive experimental method such as XRD for Pt-location determination, we cannot rule out the stabilization of Pt at other locations of the MNC. Analysis with TSM in Figure 4.3 again reveals that the S location is highly preferred in this structure, with the Pt_S and Pt_{2S} being the only two Pt-doped MNCs to fall within the 95% prediction interval. Based on the doping observations in the Pd-doped $Au_{38}q$ MNC and the demonstrated ability of the TSM to capture experimental dopant locations in the Au_{25} MNCs we suggest that at least some of the Pt dopants are located at the S position within the $Au_{38}q$ MNC. In analyzing the $Au_{38}q$ MNC for doping with different metals, we have found the

TSM to agree with at least one report of the Pd-doped MNC and suggest dopant locations not currently reported in literature for the Pt-doping within the Au_{38} MNC. We have also shown that the TSM works for doping in MNCs beyond the Au_{25} and have used the TSM to make predictions surrounding doping location within an already experimentally-synthesized MNCs.

4.3   Conclusions

In summary, we have applied our TSM for understanding doping effects and stability of ligand protected MNCs. We have shown the TSM to be a valuable extension to the current knowledge surrounding doping within MNCs, capturing a wide range of experimental observations from dopant locations to concentrations. The application of the TSM to doped MNCs represents a novel way for rationalizing doping within MNCs, moving away from simplified total-energy (DFT) calculations and significantly increasing the agreement between theory and experimental observations of doping on MNCs. We therefore view the application of the TSM to the doped MNCs as a new way to revisit doping energetics on ligand-protected MNCs. As such, it has the potential to open new avenues for accelerating bimetallic MNC discovery.

5.0   Future Work

5.1   TSM for MNC Structure Prediction AND Ligand-Mediated Doping

While experimental identification of new Au MNCs crystal structures has accelerated in recent years, computational prediction of MNC structures (especially larger MNCs) has begun to lag experiments.[120] To overcome this lag in computational predictions and create new datasets a universal tool should be developed for Au MNC structure prediction. To achieve this, ideas from the TSM can be combined with those previously proposed for MNC "inherent structure rules" and geometric scaling principles to create candidate structures[57] to expand the creation of valid MNC structures. Importantly, our TSM energetic analysis should be incorporated into this process to rule out physically-unreasonable MNC structures. The addition of the TSM should allow a ready and robust criterion for experimental accessibility to be introduced to the structure-prediction process. We note that the TSM has already been referenced and applied in structural prediction literature. [89] This future work would therefore result in an accelerated Au MNC structural prediction procedure targeted towards larger and currently undiscovered MNCs.

Additionally, with the value of the TSM in identifying dopant locations and concentrations as highlighted in Chapter 4, more Au MNC structures should be screened for potential targeted doping. As ligands have been shown to influence doping behavior [112], the TSM should also be tested against ligand-mediated doping behavior in MNCs. The TSM would be especially important for analysis of ligand-mediated doping as free energy methods highlighted in Chapter 3 are currently computationally intractable on full-ligand MNCs. In Figure 5.1, as a proof of concept for ligand-mediated doping, we tested three different ligands and two compositions of Ag doped into the $Au_{38}q$ MNC. The 5-Ag-doped MNC in Figure 5.1 was reported in literature to have a layered structure and was achieved with the R=PET ligand, which seems to agree quite well with R=CH_3 ligand energetics as well.[104] We note that at higher Ag dopant concentrations than experimentally accessible with R=PET ligands (24-Ag) in Figure 5.1, both R=PET and R=CH_3 ligands deviate significantly from parity.
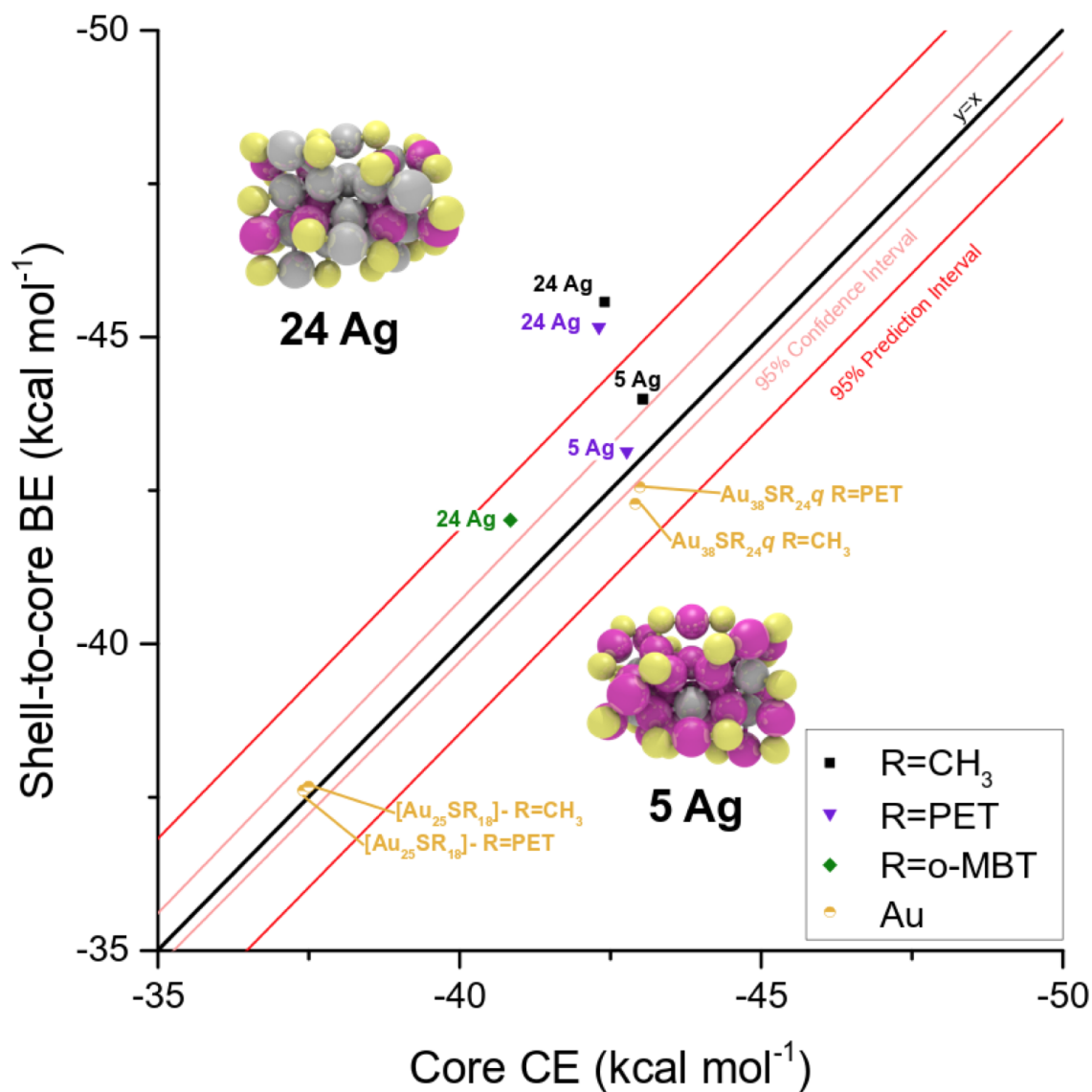
Figure 5.1: Thermodynamic stability parity plot between Shell-to-core BE and core CE on both monometallic and doped $Au_{38-x}Ag_x(SC_2H_4Ph)_{24}$ MNCs (Ag= 5, 24). Monometallic Au MNC structures are displayed in Figure 4.1 and are identical to those shown in Figure D1. 95% prediction and confidence intervals displayed were generated based on previously-tested monometallic Au methyl-thiolate MNCs (Figure 2.3). The inset images show the 5-Ag- and 25-Ag-doped MNCs, with Au as pink, Ag as silver, and S as yellow (R groups omitted for clarity). None of these MNCs showed reconstruction during relaxation with DFT.

However, when the ortho-methylbenzenethiolate (o-MBT) ligand is used (as in the synthesis of other MNCs[16]) with 24-Ag doped, the MNC now falls within parity and is predicted synthetically accessible. We note the 24-Ag MNC tested is layered in a similar way to the 5-Ag-doped MNC. Therefore, with additional testing, the TSM may open avenues to MNC synthesis via ligand-mediated doping for tailored applications.

6.0   Summary of Publications from PHD

1. M. G. Taylor and G. Mpourmpakis, "Thermodynamic Stability of Ligand- Protected Metal Nanoclusters," *Nature Communications*, vol. 8, no. May, p. 15988, 2017. [50]

2. Q. Li*, T.-y. Luo*, M. G. Taylor*, S. Wang, X. Zhu, Y. Song, G. Mpourmpakis, N. L. Rosi, and R. Jin, "Molecular "Surgery" on a 23-gold-atom Nanoparticle," *Science Advances*, vol. 3, no. 5, p. e1603193, 2017. [98]

3. Q. Li, M. G. Taylor, K. Kirschbaum, K. J. Lambright, X. Zhu, G. Mpourmpakis, and R. Jin, "Site-selective Substitution of Gold Atoms in the $Au_{24}(SR)_{20}$ Nanocluster by Silver," Journal of Colloid and Interface Science, vol. 505, no. 1 Nov 2017, pp. 1202–1207, 2017.[99]

4. Q. Li, K. J. Lambright, M. G. Taylor, K. Kirschbaum, T.-Y. Luo, J. Zhao, G. Mpourmpakis, S. Mokashi-Punekar, N. L. Rosi, and R. Jin, "Reconstructing the Surface of Gold Nanoclusters by Cadmium Doping," *Journal of the American Chemical Society*, vol. 139, no. 49, pp. 17779–17782, 2017. [100]

5. M. G. Taylor and G. Mpourmpakis, "Rethinking Heterometal Doping in Ligand-Protected Metal Nanoclusters," *Journal of Physical Chemistry Letters*, vol. 9, pp. 6773–6778, 2018. [102]

6. M. G. Taylor*, N. Austin*, C. Gounaris, and G. Mpourmpakis. "Catalyst Design Based on Morphology and Environment Dependent Adsorption on Metal Nanoparticles," *ACS Catalysis* vol. 5 no. 11, pp. 6296–6301, 2015. [10]

7. Z. Yan*, M. G. Taylor*, A. Mascareno, and G. Mpourmpakis, "Size-, Shape-, and Composition-Dependent Model for Metal Nanoparticle Stability Prediction," *Nano Letters*, vol. 18, no. 4, pp. 2696–2704, 2018. [6]

8. J. Chung, I. Granja*, M. G. Taylor*, G. Mpourmpakis, J. R. Asplin, and J. D. Rimer, "Molecular Modifiers Reveal a Mechanism of Pathological Crystal Growth Inhibition," *Nature*, vol. 536, no. 7617, pp. 446–450, 2016. [4]

9. J. Chung, M. G. Taylor, I. Granja, J. R. Asplin, G. Mpourmpakis, and J. D. Rimer. "Factors Differentiating the Effectiveness of Polyprotic Acids as Inhibitors of Calcium

Oxalate Crystallization in Kidney Stone Disease," *Crystal Growth & Design*, vol. 18 no. 9, pp. 1528–7483, 2018. [5]

10. W. Li, M. G. Taylor, S. Mozaffari, M. Dixit, S. Ivanov, S. Seifert, B. Lee, N. Shanaiah, Y. Lu, L. Kovarik, G. Mpourmpakis, and A. M. Karim. "Solvent Manipulation of the Pre-reduction Metal-Ligand Complex and Particle-Ligand Binding for Controlled Synthesis of Pd Nanoparticles," *ACS Nano*,2019, *Under Revision.*

11. J. Dean, M. G. Taylor, and G. Mpourmpakis. "Unfolding Adsorption on Metal Nanoparticles: Connecting Stability with Catalysis," *Science Advances*, 2019, *Under Revision.*

12. N. Isenberg, M. G. Taylor, C. L. Hanselman, Z. Yan, G. Mpourmpakis, and C. Gounaris. "Accurate Low-Cost Nanoparticle Energetics and Global Optimization via Tuned Bond-cutting Model," 2019, *Under Preparation.*

13. Y. Li*, M. G. Taylor*, T.-Y. Luo*, Y. Song, N. L. Rosi, G. Mpourmpakis, and R. Jin. "Heteroatom Tracing: Identification of a Dimerization Growth Pattern and Implications for Electronic Structure of Gold Nanoclusters," 2019, *Under Preparation.*

* Indicates equal contributions from the authors.

Works 1-5 are highlighted in this Thesis Document.

Appendix A

Abbreviations

BE	Binding Energy
CE	Cohesive Energy
CN	Coordination Number
COSMO	COnductor-like Screening MOdel
DFT	Density Functional Theory
ESI-MS	ElectroSpray Ionization Mass Spectroscopy
EXAFS	Extended X-ray Absorption Fine Structure
LEIST	Ligand Exchange Induced Size/Structural Transformation
MALDI-MS	Matrix-Assisted Laser Desorption/Ionization Mass Spectroscopy
MD	Molecular Dynamics
MNC	Metal Nanocluster
MNP	Metal Nanoparticle
NBO	Natural Bond Orbital
o-MBT	ortho-methylbenzethiolate
PET	Phenylethanethiolate
TBBT	4-tert-butylbenzenethiolate
TGA	Thermogravimetric analysis
TSM	Thermodynamic Stability Model
XPS	X-ray photoelectron spectroscopy
XRD	X-ray Diffraction

Appendix B

Thermodynamic Stability Model

Note: Charge and orbital determination of interacting shell atoms.

The metal atoms were first determined as core vs. shell by examining their NBO charge state. Metal atoms with more than 0.2 charge were identified as shell (indicating partially cationic Au atoms). This 0.2 charge threshold was established based on the charge of the shell Au atoms in all of the structures (via same analysis as in Figure B1). For this same core vs. shell determination, alternatively, metal atoms that were coordinated to 2 sulfurs were assigned as shell metal atoms and all other metal atoms were assigned as core. These two methods produced identical results. To determine the number of interacting metal atoms we identified the distance between the shell metal atoms and their nearest core atoms. Assuming an interaction distance cutoff for bonding at approximately 2.5 times the van der wall radii for the Au metals (4 $\mathring{A}$), the interacting or non-interacting metals can simply be counted by the number of shell metal atoms with a minimum shell-core distance less or larger than this cutoff. This automated process exactly results in the energy balance shown in Figure 2.2 for every MNC (core CE=shell-to-core BE) with the exception of $Au_{20}SR_{16}$ (and the negative test $[Cu_{25}SR_{18}]^-$ MNC). For the $Au_{20}SR_{16}$ MNC, further examination of the HOMO (electronic) orbital structure indicated primary bonding for 2 of the atoms identified as interacting shell with another shell Au atom as shown in Figure B1. This indicated that these atoms could more accurately be represented as non-interacting shell atoms despite their close proximity to one of the core metal atoms. For the charged systems ($[Au_{25}SR_{18}]^-$, $[Cu_{25}SR_{18}]^-$, and $[Ag_{25}SR_{18}]^-$) we performed vertical electron affinity calculations between the separated core and shell regions to identify where the negative charge will be located. In all cases, the shell region showed a higher electron affinity and the electron was attributed to the shell in the charged systems.
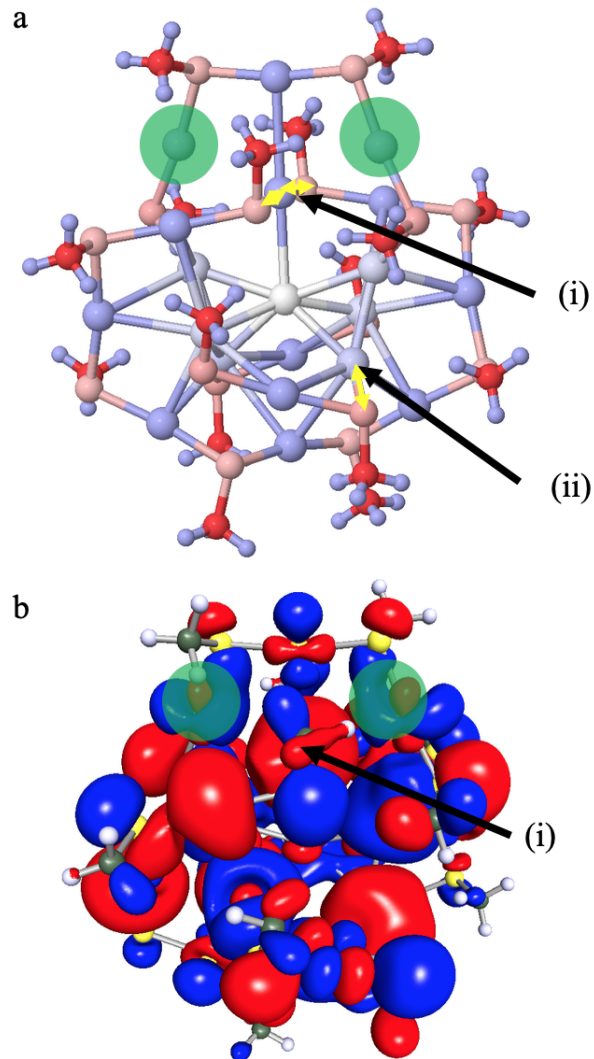
Figure B1: Optimized structure of $Au_{20}SR_{16}$, R=CH_3. (a): charge analysis, where red tints indicate negative and blue positive charges, respectively (darkest red=-0.76, darkest blue=+0.23). Dark blue metal atoms are counted as shell. Similarly, Au atom (i) shows bonds (highlighted yellow) to two sulfurs (making it a shell Au), while Au atom (ii) only shows one bond to a sulfur (making it a core Au). (b) HOMO orbital structure. Highlighted (green) Au atoms show more bonding character with bridging shell metal atom (indicated with black arrow) and therefore are counted as non-interacting shell metal atoms.
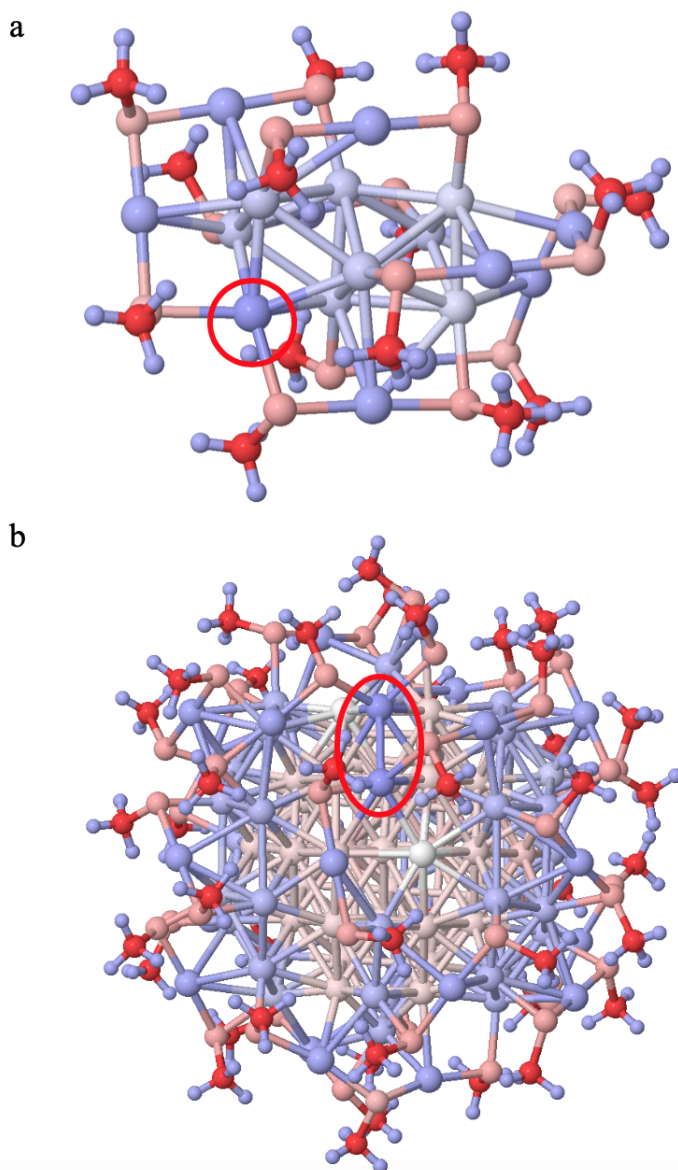
Figure B2: NBO Charge analysis highlighting differences between reported core and shell atoms. (a) optimized structure of $Au_{18}SR_{14}$ and (b) $Au_{102}SR_{44}$, with R=CH_3. Red tints indicate negative charge (darkest red=-0.76) and blue indicate positive charges (darkest blue=+0.23). Highlighted (with red ovals) Au atoms correspond to atoms previously identified as core, [1] while here we show they share the same charge state as the shell Au atoms leading to cores of 8 and 77 Au atoms for $Au_{18}SR_{14}$ and $Au_{102}SR_{44}$, respectively.

a

BE=–45 kcal mol⁻¹

b

BE=–48 kcal mol⁻¹
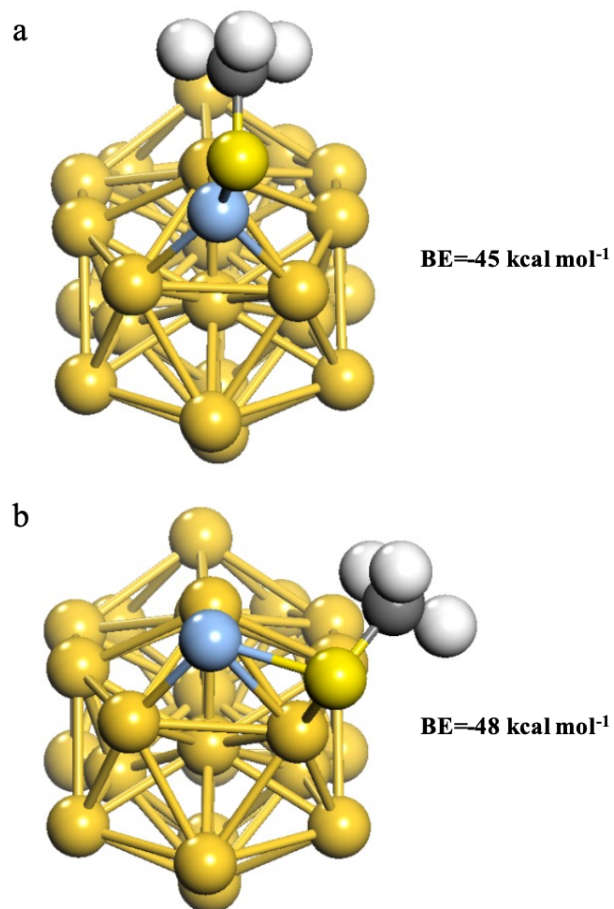
Figure B3: Binding energy of sulfur motifs with the core. Optimized structures of a single Au-SR, R=CH_3, ligand placed on the Au_{38} core structure. (a) Configuration where the S atom of the ligand interacts with the core metal structure. The shell Au has been colored in blue (the same color scheme as Figure 2.1) to differentiate from the core Au atoms. (b) Configuration where the S atom of the ligand interacts with the core structure.
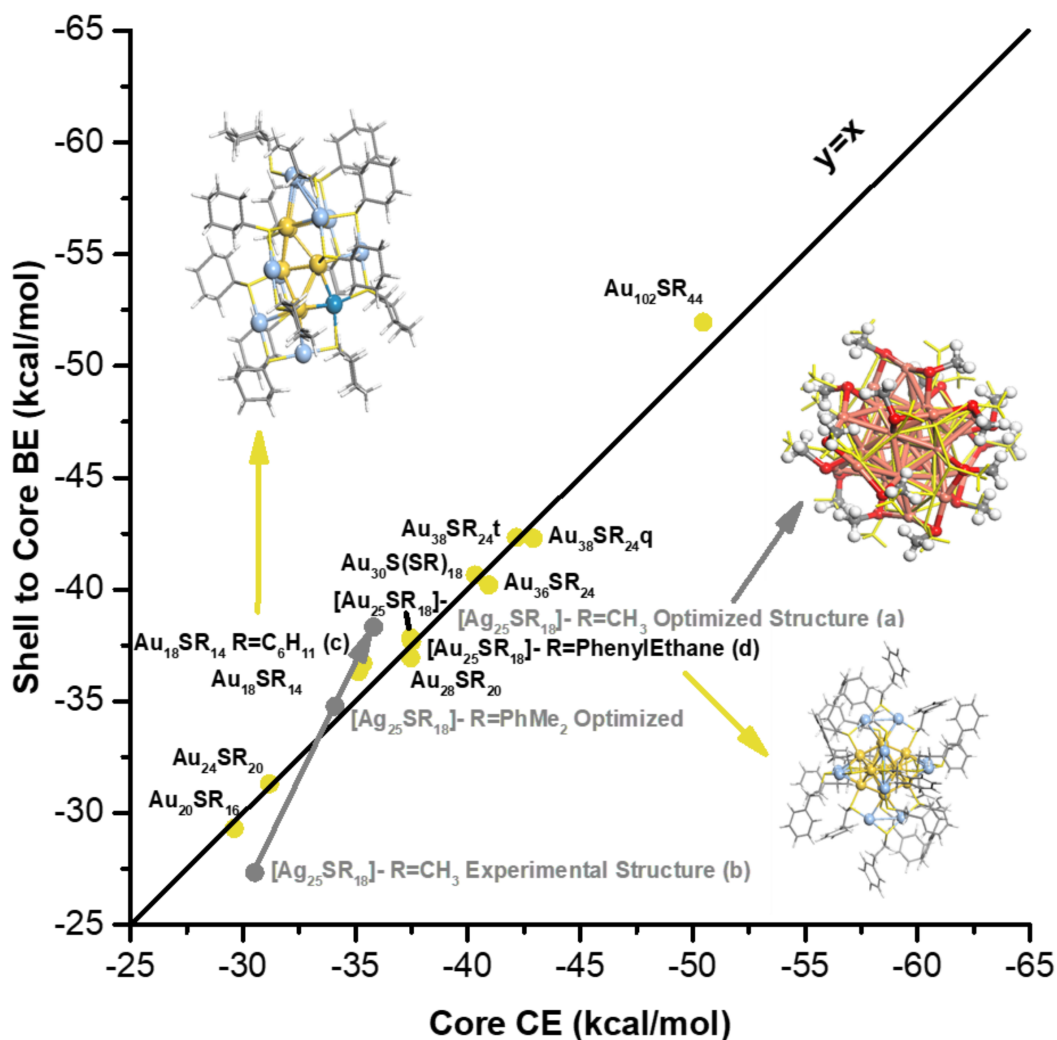
Figure B4: Ligand effects in TSM. Parity plot between core CE and the shell-to-core BE as suggested by our developed TSM. Most of the values are identical to Figure 2.2. Additional points include: the $[Ag_{25}(SR)_{18}]^-$, with R=CH_3 (i) optimized and (ii) experimental structures, respectively, (iii) the optimized $Au_{18}(SR)_{14}$ with R=C_6H_{11} and (iv) the $[Au_{25}(SR)_{18}]^-$, with R=PhenylEthyl structures. The silver arrow from (ii) to (i) indicates the shift of the core CE and shell-to-core BE during optimization of the $[Ag_{25}(SR)_{18}]^-$ R=CH_3 MNC. In the $[Ag_{25}(SR)_{18}]^-$ R=CH_3 MNC image, the red ball/stick represent the experimental structure, whereas, the yellow sticks, the optimized structure.

Note: Ligand Effects

For the $[Ag_{25}SR_{18}]^-$ MNC (Figures B4 (i) and (ii)), geometric reconstruction during optimization was noticeable (using as initial state the experimental structure and substituting the R-groups with methyls) and it is due to the lack of hydrogen-bonding in R-groups when R=CH_3. The surface reconstruction of the $[Ag_{25}SR_{18}]^-$ MNC with methyls was also evident in the energetics of the MNC after optimization when this was the only experimental structure that did not show the BE-CE energy balance. Since we noticed this reconstruction (and CE-BE imbalance), we considered the full ligands and we optimized the experimental $[Ag_{25}(SPhMe_2)_{18}]^-$ MNC. Only in this case, we noticed that optimizing the MNC accounting for the full ligands results to a perfect CE-BE energy balance. It should be noticed that none of the experimental Au structures showed any similar reconstruction upon methyl substitution and optimization. To further verify that the methyl R-group substitution does not alter the stability of other Au MNCs, we optimized the $Au_{18}SR_{14}$ and $[Au_{25}SR_{18}]^-$ MNCs with their full ligands, finding variations of only 0.3 kcal mol^{-1} in the core to shell BE while the core CE remained identical to the R=CH_3 structure for each (Figures B4 (iii) and (iv)).
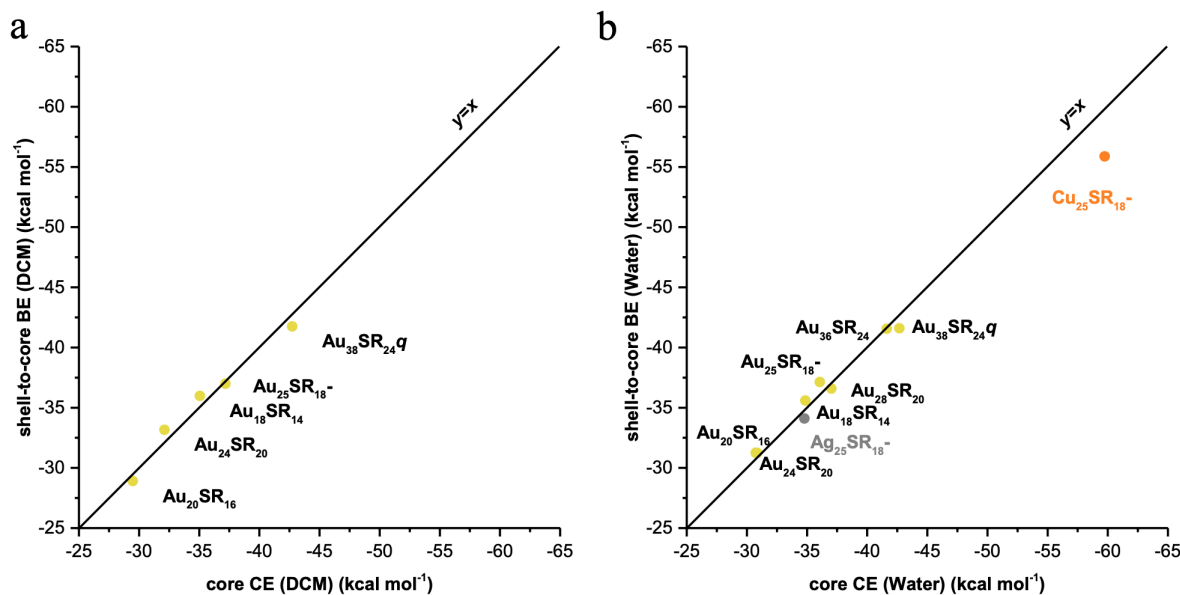
Figure B5: Solvent effects in thermodynamic stability theory. Parity plot between core CE (kcal mol^{-1}) and the shell to core BE including (a) dichloromethane (ϵ=8.93) and (b) water (ϵ=78.46) solvent effects, using the COSMO implicit solvation model.

Table B1: Density Functional comparison.

Method (DFT)	core CE (kcal mol^{-1})	shell-to-core BE (kcal mol^{-1})
ri-BP-86	-37.82	-37.40
ri-PBE	-38.95	-39.29
ri-BLYP	-31.0	-28.57

56
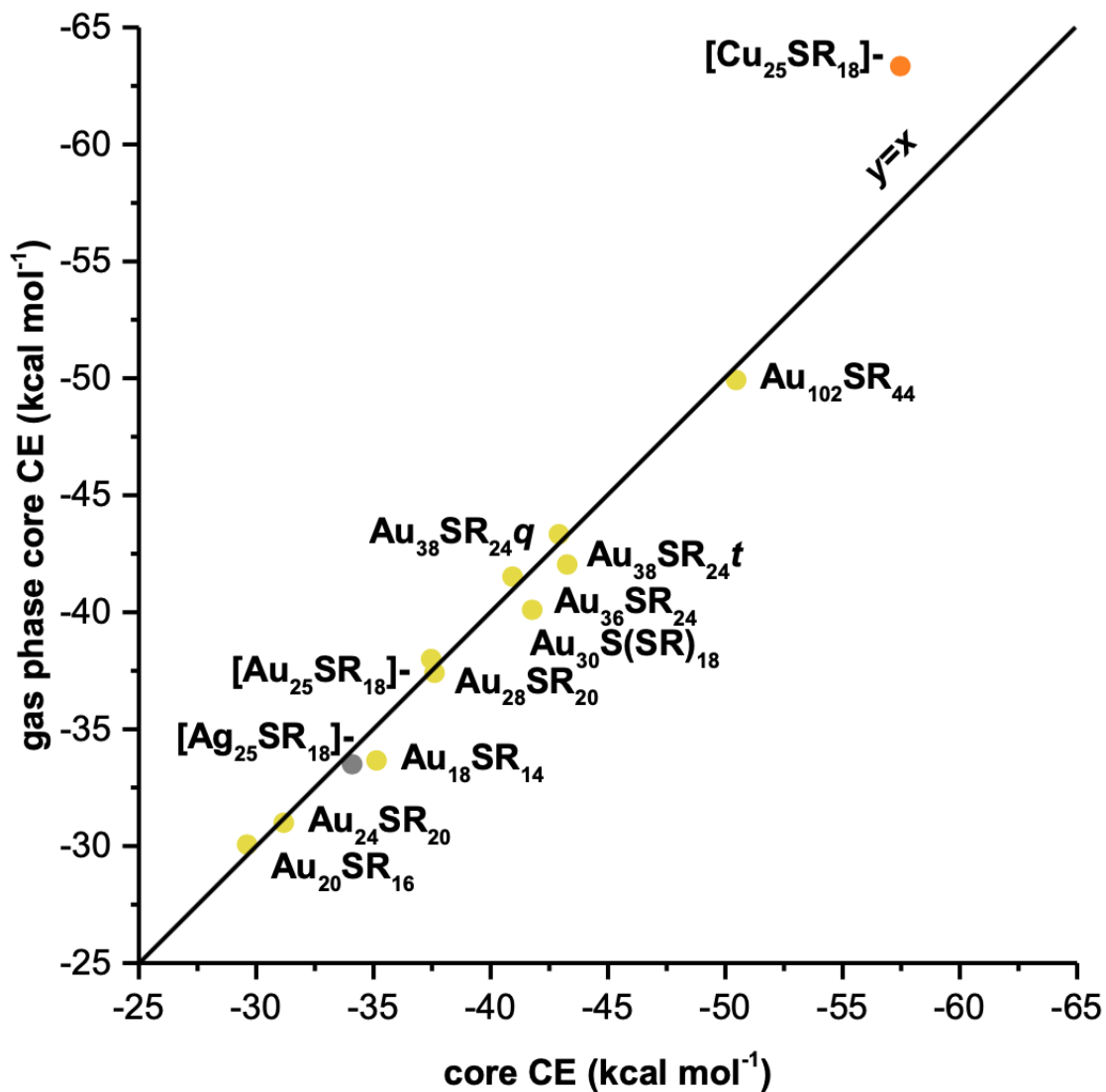
Figure B6: Gas phase to core cohesive energy comparison. Parity plot between core CE and the gas phase core CE, indicating remarkable parity between the gas phase and shell-influenced CE values.

Appendix C

Targeted MNC Transformations
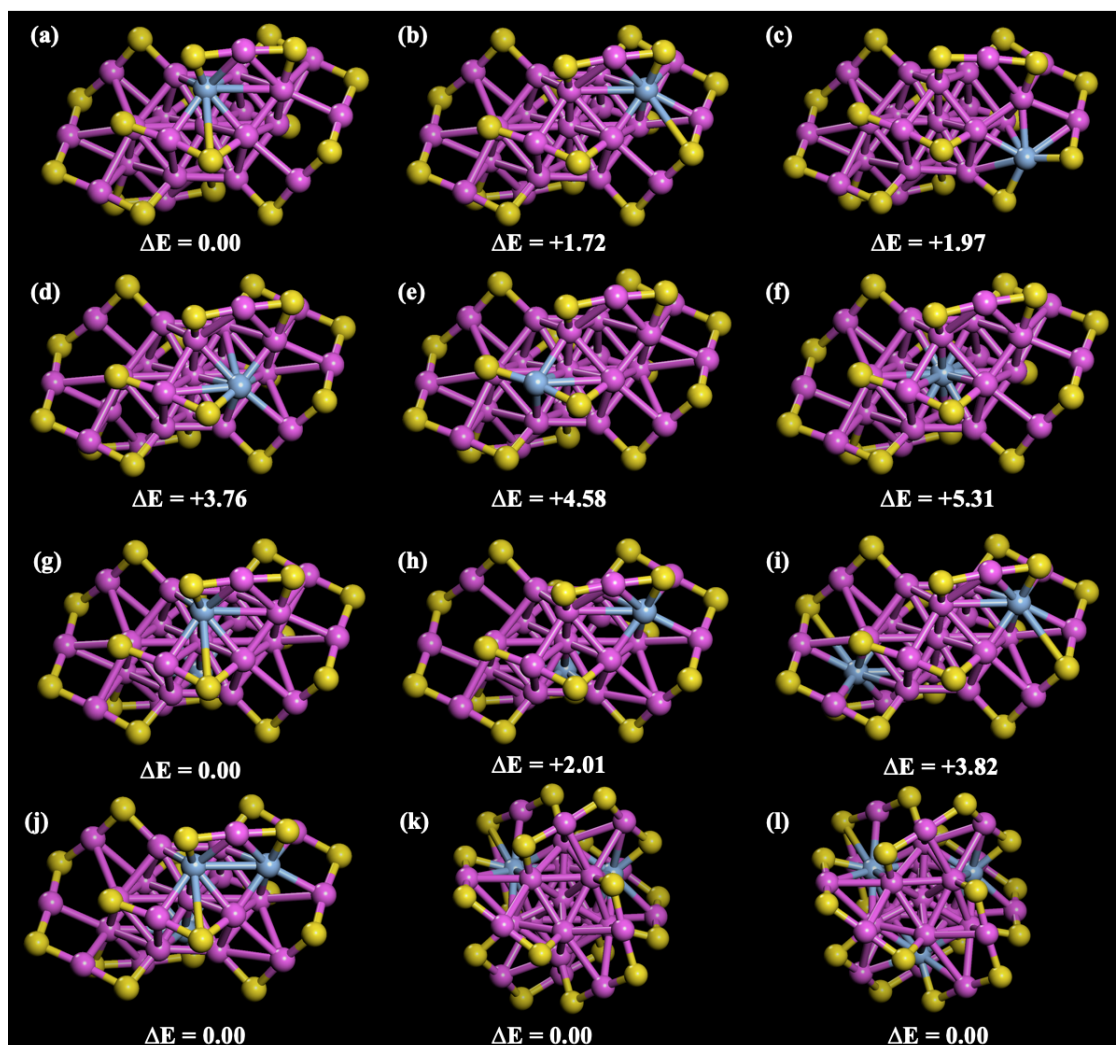
Figure C1: DFT-relaxed $[Au_{23-x}Ag_x(SR)_{18}]^-$ (x = 1 to 3) and $[Au_{25-y}Ag_y(SR)_{18}]^-$ (y = 2, 3) MNCs and associated relative electronic energies (ΔE in kcal mol^{-1} taken in reference to lowest energy isomer for each composition). Carbon and hydrogen atoms have been removed for clarity. Color code: Pink=Au, Yellow=S, Silver=Ag. In (a-f), x=1 and (a) and (b) represent the positions observed in X-ray Diffraction experiments. In (g-i), x=2, in (j), x=3, in (k), y=2, and in (l), y=3.
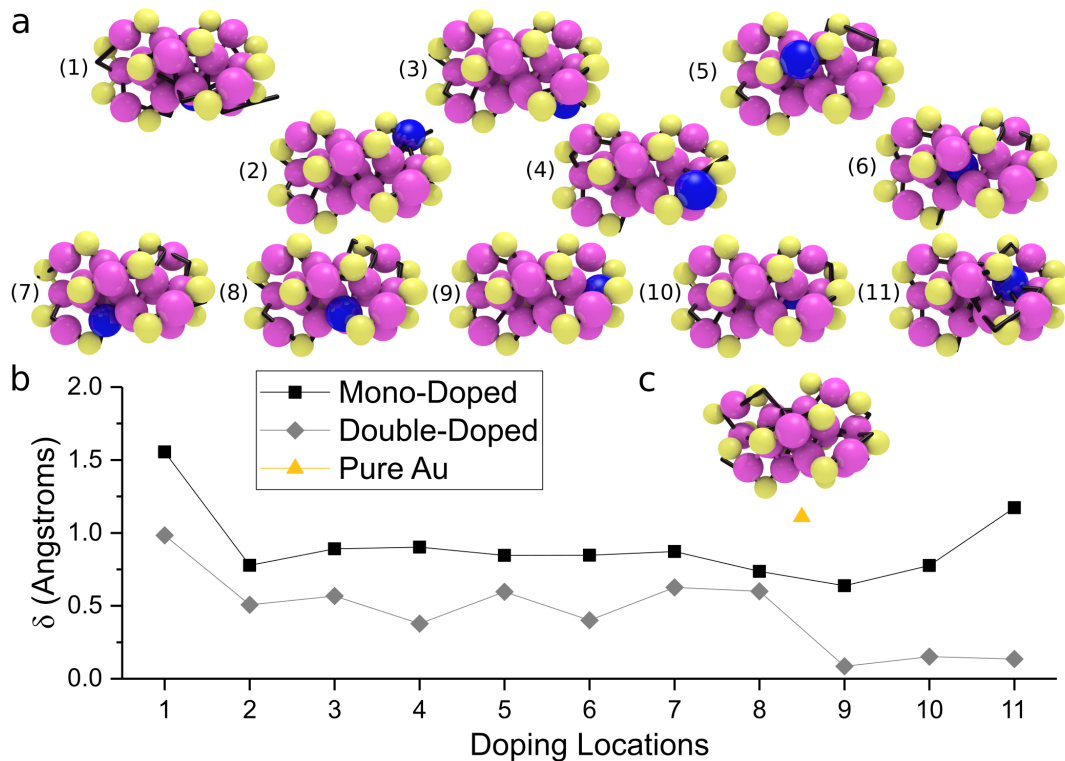
Figure C2: DFT results for $Au_{20}Cd(SR)_{16}$ and $[Au_{21}(SR)_{16}]^-$ MNCs, with the Cd dopant placed at different locations. Structure (9) represents the experimentally determined doping locations (in double doped configuration). (a) $Au_{20}Cd(SR)_{16}$ geometries generated from experimental $[Au_{20}Cd_2(SR)_{16}]^-$ by switching or replacing Cd with Au at specific locations before ('ball and stick') and after (red sticks) geometry relaxation. In the 'ball and stick' representations Magenta=Au; Blue=Cd; and Yellow = S. All C and H atoms are omitted for clarity. (b) Doping locations in $Au_{20}Cd(SR)_{16}$ and pure $[Au_{21}(SR)_{16}]^-$ compared to geometric rearrangement. Data for $[Au_{20}Cd_2(SR)_{16}]^-$ reconstruction as seen in Figure 3.4 is shown for comparison. (c) $[Au_{21}(SR)_{16}]^-$ geometry generated from experimental $[Au_{20}Cd_2(SR)_{16}]^-$ by replacing Cd with Au before ('ball and stick') and after (red sticks) geometry relaxation with the same coloring scheme as (a).

60

Appendix D

Heterometal Doping of MNCs
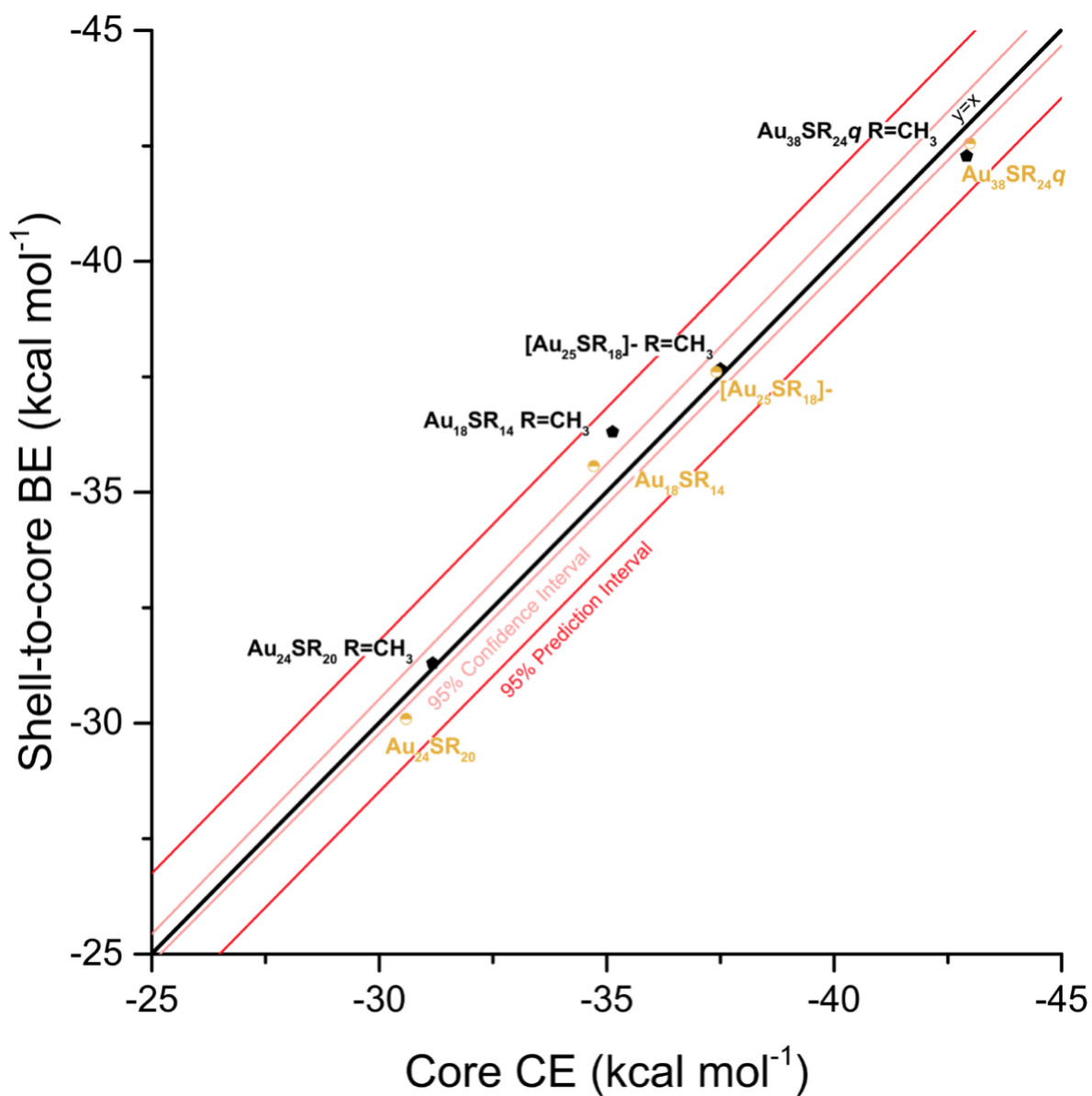
Figure D1: TSM (Shell-to-core BE vs. Core CE) applied to Au MNCs highlighted in Figure 4.2 (gold points) compared to the same MNC frameworks with R=CH_3 (black points). The distance between two corresponding black and gold points is at most 1.34 kcal mol^{-1} (Au_{24} MNC), while the average distance between the two is 0.65 kcal mol^{-1}, which was rounded up to 0.7 kcal mol^{-1}, representing the extended range of "synthesizability" with full-ligand MNCs.
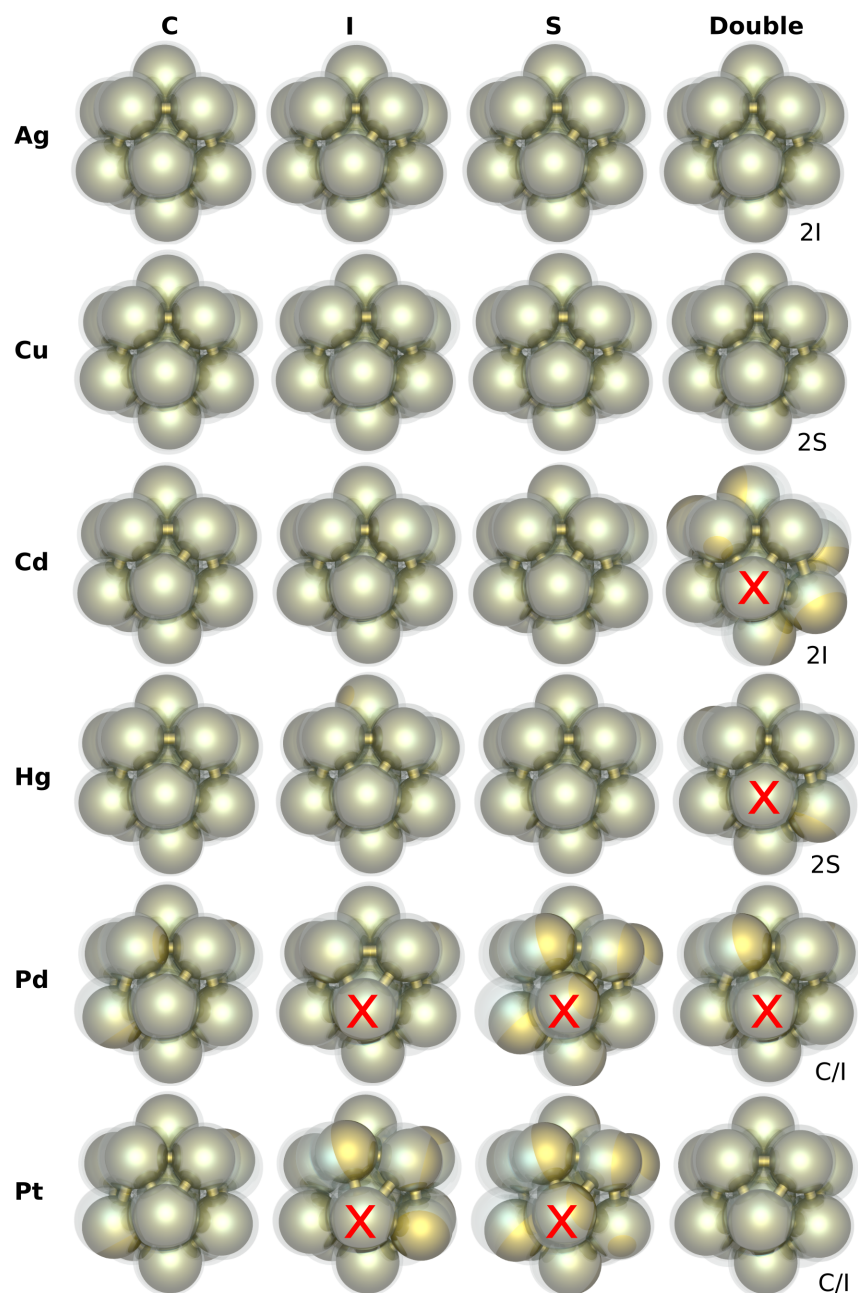
Figure D2: Relaxed (golden balls/sticks) conformations of cores of the $[Au_{25-x}M_x(SC_2H_4Ph)_{18}]^q$ MNCs shown in Figure 4.2 compared to the core of the pure Au25 MNC (transparent blue balls). Different metal dopants are highlighted in the rows, while the different dopant locations/concentrations are in the columns. Structures that show reconstruction (distortion from icosahedral symmetry) are indicated with a red X.

Table D1: Average displacements (δ), in $\mathring{A}$, of core structures of doped $[Au_{25-x}M_x(SC_2H_4Ph)_{18}]^q$ MNCs (shown in Figure 4.2 and Figure D2). Cores that visibly reconstructed above in Figure D2 are counted as reconstructed and are highlighted in bold. We note that these MNCs all show δs larger than 0.17 $\mathring{A}$.

| | | MNC by Dopant Location/Concentration | | | |
		C	I	S	Double Doped
	Ag	0.04	0.07	0.05	0.08
	Cu	0.08	0.09	0.06	0.09
Metals	Cd	0.07	0.08	0.11	**0.26**
	Hg	0.08	0.10	0.09	**0.17**
	Pd	0.14	**0.18**	**0.30**	**0.20**
	Pt	0.14	**0.32**	**0.33**	0.16
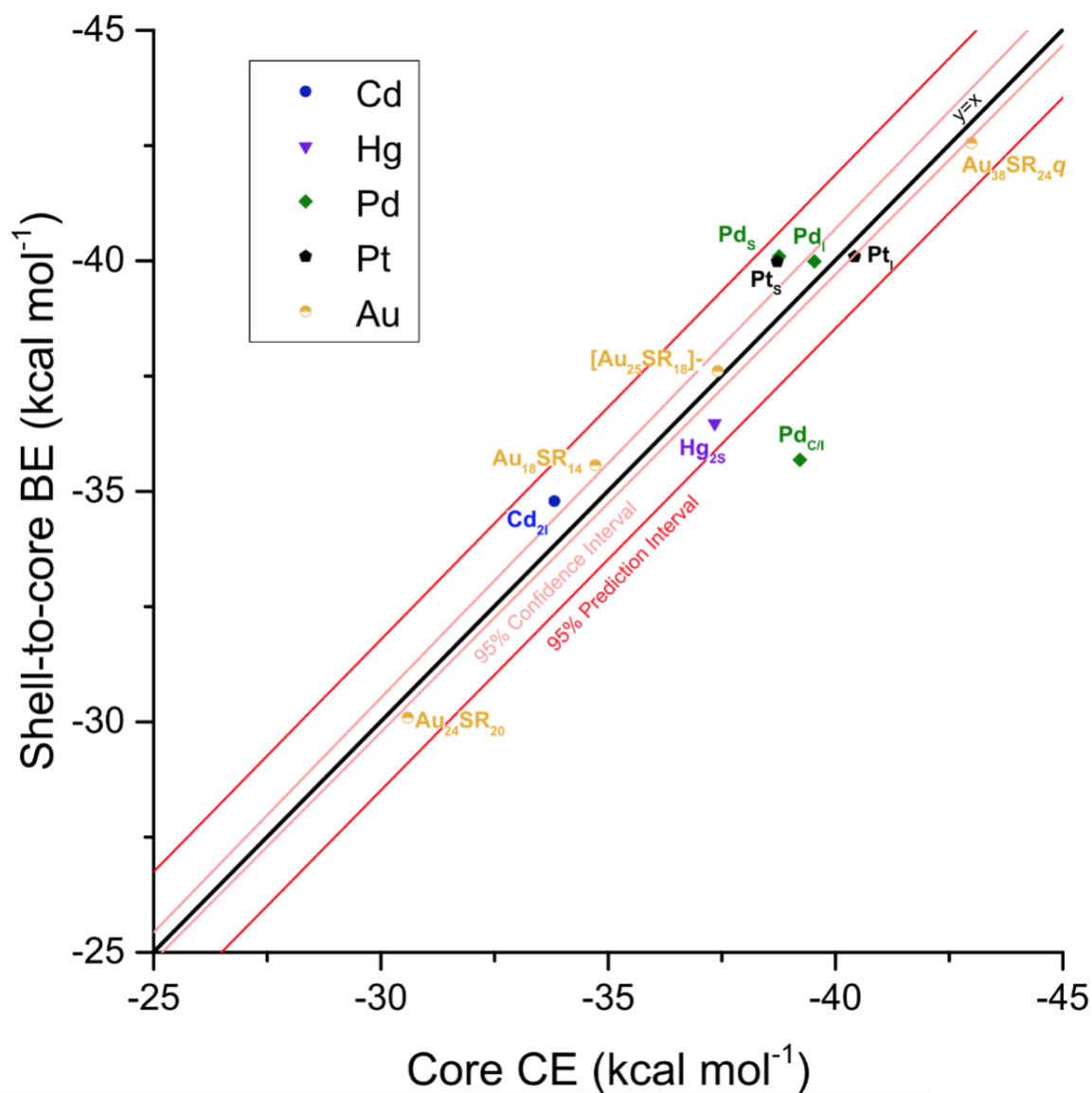
Figure D3: TSM parity plot between Shell-to-core BE and core CE applied to MNCs that rearranged over the course of relaxation highlighted in Figure D2 and Table D1. Pure Au structures are identical to those displayed in Figure 4.1. 95% prediction and confidence are identical to Figure 2.3. All data points with metal labels correspond to doped $[Au_{25-x}M_x(SC_2H_4Ph)_{18}]^q$ MNCs with subscripts corresponding to the location(s) doped within the MNC.

Table D2: Delta (difference in) charge (calculated via NBO) between the dopants in the relaxed $[Au_{24}M(SC_2H_4Ph)_{18}]^q$ MNCs (shown in Figure 4.2 and Figure D3) and the Au in the corresponding location within the Au_{25} MNC. MNCs that reconstructed (see Table D1) are not included as there are not roughly equivalent Au locations to compare to for these MNCs. Cd_S is highlighted in bold due to its large positive charge relative to Au at this position.

		MNC by Dopant Location		
		C	I	S
	Ag	0.16	0.26	0.24
	Cu	0.55	0.46	0.40
Metals	Cd	0.71	0.77	**0.87**
	Hg	0.61	0.49	0.61
	Pd	-0.38	—-	—-
	Pt	-0.61	—-	—-

Table D3: Relative DFT electronic energies (taken with respect to the lowest-energy isomers) in kcal mol^{-1} for relaxed $[Au_{24}M(SC_2H_4Ph)_{18}]^q$ MNCs (shown in Figure 4.2 and Figure D2) and Au in the corresponding location within the Au_{25} MNC. Lowest energy MNCs among the isomers are highlighted in bold and are equal to zero.

		MNC by Dopant Location		
		C	I	S
	Ag	7.09	**0.00**	4.31
	Cu	**0.00**	0.50	3.81
Metals	Cd	10.83	**0.00**	10.93
	Hg	14.83	**0.00**	15.92
	Pd	**0.00**	12.33	14.97
	Pt	**0.00**	14.25	18.40

Bibliography

[1] A. Das, C. Liu, H. Y. Byun, K. Nobusada, S. Zhao, N. Rosi, and R. Jin, "Structure Determination of $[Au_{18}(SR)_{14}]$," *Angewandte Chemie International Edition*, vol. 54, no. 10, pp. 3140–3144, 2015.

[2] M. Haruta, T. Kobayashi, H. Sano, and N. Yamada, "Novel Gold Catalysts for the Oxidation of Carbon Monoxide at a Temperature far Below 0 °C," *Chemistry Letters*, vol. 16, no. 2, pp. 405–408, 1987.

[3] M. C. Daniel and D. Astruc, "Gold Nanoparticles: Assembly, Supramolecular Chemistry, Quantum-Size-Related Properties, and Applications Toward Biology, Catalysis, and Nanotechnology," *Chemical Reviews*, vol. 104, no. 1, pp. 293–346, 2004.

[4] J. Chung, I. Granja, M. G. Taylor, G. Mpourmpakis, J. R. Asplin, and J. D. Rimer, "Molecular Modifiers Reveal a Mechanism of Pathological Crystal Growth Inhibition," *Nature*, vol. 536, no. 7617, pp. 446–450, 2016.

[5] J. Chung, M. G. Taylor, I. Granja, J. R. Asplin, G. Mpourmpakis, and J. D. Rimer, "Factors Differentiating the Effectiveness of Polyprotic Acids as Inhibitors of Calcium Oxalate Crystallization in Kidney Stone Disease," *Crystal Growth & Design*, vol. 18, no. 9, pp. 5617–5627, 2018.

[6] Z. Yan, M. G. Taylor, A. Mascareno, and G. Mpourmpakis, "Size-, Shape-, and Composition-Dependent Model for Metal Nanoparticle Stability Prediction," *Nano Letters*, vol. 18, no. 4, pp. 2696–2704, 2018.

[7] C. Dhand, N. Dwivedi, X. J. Loh, A. N. Jie Ying, N. K. Verma, R. W. Beuerman, R. Lakshminarayanan, and S. Ramakrishna, "Methods and Strategies for the Synthesis of Diverse Nanoparticles and their Applications: A Comprehensive Overview," *RSC Advances*, vol. 5, no. 127, pp. 105003–105037, 2015.

[8] G. Niu, L. Zhang, A. Ruditskiy, L. Wang, and Y. Xia, "A Droplet-Reactor System Capable of Automation for the Continuous and Scalable Production of Noble-Metal Nanocrystals," *Nano Letters*, vol. 18, pp. 3879–3884, jun 2018.

[9] R. Jin, C. Zeng, M. Zhou, and Y. Chen, "Atomically Precise Colloidal Metal Nanoclusters and Nanoparticles: Fundamentals and Opportunities," *Chemical Reviews*, vol. 116, pp. 10346–10413, sep 2016.

[10] M. G. Taylor, N. Austin, C. Gounaris, and G. Mpourmpakis, "Catalyst Design Based on Morphology and Environment Dependent Adsorption on Metal Nanoparticles," *ACS Catalysis*, vol. 5, no. 11, pp. 6296–6301, 2015.

[11] R. Jin, "Toward Atomically Precise Nanoclusters and Nanoparticles," *Acta Phys. - Chim. Sin.*, vol. 34, pp. 737–739, dec 2018.

[12] P. D. Jadzinsky, G. Calero, C. J. Ackerson, D. A. Bushnell, and R. D. Kornberg, "Structure of a Thiol Monolayer-Protected Gold Nanoparticle at 1.1 A Resolution," *Science*, vol. 318, no. October, pp. 430–433, 2007.

[13] I. Chakraborty and T. Pradeep, "Atomically Precise Clusters of Noble Metals: Emerging Link between Atoms and Nanoparticles," *Chemical Reviews*, vol. 117, no. 12, pp. 8208–8271, 2017.

[14] C.-j. Zeng, M. Zhou, C. Gayathri, R. R. Gil, M. Y. Sfeir, and R. Jin, "$Au_{10}(TBBT)_{10}$: The Beginning and the End of $Au_n(TBBT)_m$ Nanoclusters," *Chinese Journal of Chemical Physics*, vol. 31, no. 4, pp. 555–562, 2018.

[15] M. Brust, M. Walker, D. Bethell, D. J. Schiffrin, and R. Whyman, "Synthesis of Thiol-derivatised Gold Nanoparticles in a Two-phase Liquid-Liquid System," *Journal of the Chemical Society, Chemical Communications*, no. 7, pp. 801–802, 1994.

[16] Y. Chen, C. Zeng, D. R. Kauffman, and R. Jin, "Tuning the Magic Size of Atomically Precise Gold Nanoclusters via Isomeric Methylbenzenethiols," *Nano Letters*, vol. 15, no. 5, pp. 3603–3609, 2015.

[17] R. Jin, H. Qian, Z. Wu, Y. Zhu, M. Zhu, A. Mohanty, and N. Garg, "Size Focusing: A Methodology for Synthesizing Atomically Precise Gold Nanoclusters," *The Journal of Physical Chemistry Letters*, vol. 1, no. 19, pp. 2903–2910, 2010.

[18] C. Zeng, Y. Chen, A. Das, and R. Jin, "Transformation Chemistry of Gold Nanoclusters: From One Stable Size to Another," *The Journal of Physical Chemistry Letters*, vol. 6, no. 6, pp. 2976–2986, 2015.

[19] H. Häkkinen, M. Walter, and H. Grönbeck, "Divide and Drotect: Capping Gold Nanoclusters with Molecular Gold-thiolate Rings," *Journal of Physical Chemistry B*, vol. 110, no. 20, pp. 9927–9931, 2006.

[20] H. Häkkinen, "Atomic and Electronic Structure of Gold Clusters: Understanding Flakes, Cages and Superatoms from Simple Concepts," *Chemical Society Reviews*, vol. 37, no. 9, p. 1847, 2008.

[21] M. Walter, J. Akola, O. Lopez-Acevedo, P. D. Jadzinsky, G. Calero, C. J. Ackerson, R. L. Whetten, H. Grönbeck, and H. Häkkinen, "A Unified View of Ligand-Protected Gold Clusters as Superatom Complexes.," *Proceedings of the National Academy of Sciences of the United States of America*, vol. 105, no. 27, pp. 9157–9162, 2008.

[22] T. Iwasa and K. Nobusada, "Theoretical Investigation of Optimized Structures of Thiolated Gold Cluster $[Au_{25}(SCH_3)_{18}]^+$," *Journal of Physical Chemistry*, vol. 111, no. 111, pp. 45–49, 2007.

[23] S. Yamazoe, S. Takano, W. Kurashige, T. Yokoyama, K. Nitta, Y. Negishi, and T. Tsukuda, "Hierarchy of Bond Stiffnesses Within Icosahedral-based Gold Clusters Protected by Thiolates," *Nature Communications*, vol. 7, p. 10414, 2016.

[24] J. R. Reimers, Y. Wang, B. O. Cankurtaran, and M. J. Ford, "Chemical Analysis of the Superatom Model for Sulfur-stabilized Gold Nanoparticles," *Journal of the American Chemical Society*, vol. 132, no. 24, pp. 8378–8384, 2010.

[25] C. Zeng, C. Liu, Y. Chen, N. L. Rosi, and R. Jin, "Gold-Thiolate Ring as a Protecting Motif in the $Au_{20}(SR)_{16}$ Nanocluster and Implications.," *Journal of the American Chemical Society*, vol. 20, no. 136, pp. 16–19, 2014.

[26] A. Das, C. Liu, C. Zeng, G. Li, T. Li, N. L. Rosi, and R. Jin, "Cyclopentanethiolato-Protected $Au_{36}(SC_5H_9)_{24}$ Nanocluster: Crystal Structure and Implications for the Steric and Electronic Effects of Ligand.," *Journal of Physical Chemistry A*, vol. 36, no. 118, pp. 8264–8269, 2014.

[27] L. Cheng, Y. Yuan, X. Zhang, and J. Yang, "Superatom Networks in Thiolate-protected Gold Nanoparticles," *Angewandte Chemie - International Edition*, vol. 52, no. 34, pp. 9035–9039, 2013.

[28] W. W. Xu, B. Zhu, X. C. Zeng, and Y. Gao, "A Grand Unified Model for Liganded Gold Clusters," *Nature Communications*, vol. 7, p. 13574, 2016.

[29] W. W. Xu, X. C. Zeng, and Y. Gao, "Application of electronic counting rules for ligand-protected gold nanoclusters," *Accounts of Chemical Research*, vol. 51, no. 11, pp. 2739–2747, 2018.

[30] Y. Pei, P. Wang, Z. Ma, and L. Xiong, "Growth-rule-guided structural exploration of thiolate-protected gold nanoclusters," *Accounts of Chemical Research*, vol. 52, no. 1, pp. 23–33, 2019.

[31] G. Salassa, A. Sels, F. Mancin, and T. Bürgi, "Dynamic Nature of Thiolate Monolayer in $Au_{25}(SR)_{18}$ Nanoclusters," *ACS Nano*, vol. 11, no. 12, pp. 12609–12614, 2017.

[32] B. Zhang, G. Salassa, and T. Bürgi, "Silver migration between $au_{38}(sc_2h_4ph)_{24}$ and doped $ag_xau_{38-x}(sc_2h_4ph)_{24}$ nanoclusters," *Chem. Commun.*, vol. 52, pp. 9205–9207, 2016.

[33] K. Kimura, N. Sugimoto, S. Sato, H. Yao, Y. Negishi, and T. Tsukuda, "Size Determination of Gold Clusters by Polyacrylamide Gel Electrophoresis in a Large Cluster Region," *Journal of Physical Chemistry C*, vol. 113, no. 32, pp. 14076–14082, 2009.

[34] A. Dass, "Nano-scaling Law: Geometric Foundation of Thiolated Gold Nanomolecules," *Nanoscale*, vol. 4, no. 7, p. 2260, 2012.

[35] Y. Negishi, T. Iwai, and M. Ide, "Continuous Modulation of Electronic Structure of Stable Thiolate-protected Au_{25} Cluster by Ag Doping," *Chemical Communications*, vol. 46, no. 26, p. 4713, 2010.

[36] J. Zhao and R. Jin, "Heterogeneous Catalysis by Gold and Gold-based Bimetal Nanoclusters," *Nano Today*, vol. 18, pp. 86–102, 2018.

[37] Y. Negishi, K. Igarashi, K. Munakata, W. Ohgake, and K. Nobusada, "Palladium doping of magic gold cluster $au_{38}(sc_2h_4ph)_{24}$: Formation of $pd_2au_{36}(sc_2h_4ph)_{24}$ with higher stability than $au_{38}(sc_2h_4ph)_{24}$," *Chemical Communications*, vol. 48, pp. 660–662, 2012.

[38] Z. Wu, "Anti-galvanic reduction of thiolate-protected gold and silver nanoparticles," *Angewandte Chemie International Edition*, vol. 51, no. 12, pp. 2934–2938, 2012.

[39] S. Bhat, A. Baksi, S. K. Mudedla, G. Natarajan, V. Subramanian, and T. Pradeep, "$au_{22}ir_3(pet)_{18}$: An unusual alloy cluster through intercluster reaction," *The Journal of Physical Chemistry Letters*, vol. 8, no. 13, pp. 2787–2793, 2017.

[40] S. Wang, Q. Li, X. Kang, and M. Zhu, "Customizing the Structure, Composition, and Properties of Alloy Nanoclusters by Metal Exchange," *Accounts of Chemical Research*, vol. 51, no. 11, pp. 2784–2792, 2018.

[41] R. Jin and K. Nobusada, "Doping and Alloying in Atomically Precise Gold Nanoparticles," *Nano Research*, vol. 7, no. 3, pp. 285–300, 2014.

[42] M. J. Hartmann, H. Häkkinen, J. E. Millstone, and D. S. Lambrecht, "Impacts of Copper Position on the Electronic Structure of $[Au_{25-x}Cu_x(SH)_{18}]^-$ Nanoclusters," *The Journal of Physical Chemistry C*, vol. 119, no. 15, pp. 8290–8298, 2015.

[43] Y. Niihori, S. Hossain, B. Kumar, L. V. Nair, W. Kurashige, and Y. Negishi, "Perspective: Exchange Reactions in Thiolate-protected Metal Clusters," *APL Materials*, vol. 5, no. 5, p. 053201, 2017.

[44] D.-e. Jiang and S. Dai, "From Superatomic $Au_{25}(SR)_{18}^-$ to Superatomic $M@Au_{24}(SR)_{18}^q$ Core-Shell Clusters," *Inorganic Chemistry*, vol. 48, no. 7, pp. 2720–2722, 2009.

[45] R. Jin, "Atomically Precise Metal Nanoclusters: Stable Sizes and Optical Properties," *Nanoscale*, vol. 15, no. 7, pp. 1549–1565, 2015.

[46] S. Sharma, S. Yamazoe, T. Ono, W. Kurashige, Y. Niihori, K. Nobusada, T. Tsukuda, and Y. Negishi, "Tuning the Electronic Structure of Thiolate-protected 25-atom Clusters by Co-substitution with Metals Having Different Preferential Sites," *Dalton Transactions*, vol. 45, no. 45, pp. 18064–18068, 2016.

[47] S. Wang, Y. Song, S. Jin, X. Liu, J. Zhang, Y. Pei, X. Meng, M. Chen, P. Li, and M. Zhu, "Metal Exchange Method Using Au_{25} Nanoclusters as Templates for Alloy Nanoclusters with Atomic Precision," *Journal of the American Chemical Society*, vol. 137, no. 12, pp. 4018–4021, 2015.

[48] L. Liao, S. Zhou, Y. Dai, L. Liu, C. Yao, C. Fu, J. Yang, and Z. Wu, "Mono-mercury Doping of Au_{25} and the HOMO/LUMO Energies Evaluation Employing Differential Pulse Voltammetry," *Journal of the American Chemical Society*, vol. 137, no. 30, pp. 9511–9514, 2015.

[49] B. Zhang, S. Kaziz, H. Li, D. Wodka, S. Malola, O. Safonova, M. Nachtegaal, C. Mazet, I. Dolamic, J. Llorca, E. Kalenius, L. M. Lawson Daku, H. Hakkinen,

T. Bürgi, and N. Barrabés, "$Pd_2Au_{36}(SR)_{24}$ Cluster: Structure Studies," *Nanoscale*, vol. 7, no. 40, pp. 17012–17019, 2015.

[50] Taylor, Michael G. and Mpourmpakis, Giannis, "Thermodynamic Stability of Ligand-Protected Metal Nanoclusters," *Nature Communications*, vol. 8, no. May, p. 15988, 2017.

[51] A. D. Becke and J. P. Perdew, "Density-Functional Exchange-Energy Approximation with Correct Asymptotic Behavior," *Physical Review A*, vol. 38, no. 6, pp. 3098–3100, 1988.

[52] J. P. Perdew, "Density-Functional Approximation for the Correlation Energy of the Inhomogeneous Electron Gas," *Physical Review B*, vol. 33, no. 12, pp. 8822–8824, 1986.

[53] F. Weigend, M. Häser, H. Patzelt, and R. Ahlrichs, "RI-MP2: Optimized Auxiliary Basis Sets and Demonstration of Efficiency," *Chemical Physics Letters*, vol. 294, no. 1-3, pp. 143–152, 1998.

[54] F. Weigend and M. Häser, "RI-MP2: First Derivatives and Global Consistency," *Theoretical Chemistry Accounts*, vol. 97, no. 1-4, p. 331, 1997.

[55] M. Feyereisen, G. Fitzgerald, and A. Komornicki, "Use of Approximate Integrals in *ab initio* Theory. An Application in MP2 Energy Calculations," *Chemical Physics Letters*, vol. 208, pp. 359–363, jun 1993.

[56] R. Ahlrichs, M. Bär, M. Häser, H. Horn, C. Kölmel, M. Bar, M. Haser, H. Horn, and C. Kolmel, "Electronic-Structure Calculations on Workstation Computers - the Program System Turbomole," *Chemical Physics Letters*, vol. 162, no. 3, pp. 165–169, 1989.

[57] Y. Pei, R. Pal, C. Liu, Y. Gao, Z. Zhang, and X. C. Zeng, "Interlocked Catenane-like Structure Predicted in $Au_{24}(SR)_{20}$: Implication to Structural Evolution of Thiolated Gold Clusters from Homoleptic Gold(I) Thiolates to Core-stacked Nanoparticles," *Journal of the American Chemical Society*, vol. 134, no. 6, pp. 3015–3024, 2012.

[58] D. Crasto, G. Barcaro, M. Stener, L. Sementa, A. Fortunelli, and A. Dass, "$Au_{24}(SAdm)_{16}$ Nanomolecules: X-ray Crystal Structure, Theoretical Analysis, Adaptability of Adamantane Ligands to Form $Au_{23}(SAdm)_{16}$ and $Au_{25}(SAdm)_{16}$,

and its Relation to $Au_{25}(SR)_{18}$," *Journal of the American Chemical Society*, vol. 136, no. 42, pp. 14933–14940, 2014.

[59] A. Das, T. Li, G. Li, K. Nobusada, C. Zeng, N. L. Rosi, and R. Jin, "Crystal Structure and Electronic Properties of a Thiolate-protected Au_{24} Nanocluster.," *Nanoscale*, vol. 6, no. 12, pp. 6458–62, 2014.

[60] M. Zhu, C. M. Aikens, F. J. Hollander, G. C. Schatz, and R. Jin, "Correlating the Crystal Structure of A Thiol-Protected Au_{25} Cluster and Optical Properties," *Journal of the American Chemical Society*, vol. 130, no. 18, pp. 5883–5885, 2008.

[61] C. Zeng, T. Li, A. Das, N. L. Rosi, and R. Jin, "Chiral Structure of Thiolate-protected 28-gold-atom Nanocluster Determined by X-ray Crystallography," *Journal of the American Chemical Society*, vol. 135, no. 27, pp. 10011–10013, 2013.

[62] Y. Li, G. Galli, and F. Gygi, "Electronic structure of thiolate-covered gold nanoparticles: $au_{102}(mba)_{44}$," *ACS Nano*, vol. 2, no. 9, pp. 1896–1902, 2008.

[63] Q. Tang and D. E. Jiang, "Revisiting Structural Models for $Au_{18}(SR)_{14}$," *Journal of Physical Chemistry C*, vol. 119, no. 5, pp. 2904–2909, 2015.

[64] S. Malola, L. Lehtovaara, S. Knoppe, K.-j. Hu, R. E. Palmer, T. Bu, and H. Hakkinen, "$Au_{40}(SR)_{24}$ Cluster as a Chiral Dimer of 8-Electron Superatoms: Structure and Optical Properties," *Journal of the American Chemical Society*, vol. 134, no. 48, p. 19560−19563, 2012.

[65] Y. Pei, Y. Gao, N. Shao, and C. Z. Xiao, "Thiolate-Protected $Au_{20}(SR)_{16}$ Cluster: Prolate Au_8 Core with New $[Au_3(SR)_4]$ Staple Motif," *Journal of the American Chemical Society*, vol. 131, no. 38, pp. 13619–13621, 2009.

[66] S. Tian, Y.-Z. Li, M.-B. Li, J. Yuan, J. Yang, Z. Wu, and R. Jin, "Structural Isomerism in Gold Nanoparticles Revealed by X-ray Crystallography.," *Nature communications*, vol. 6, p. 8667, 2015.

[67] B. M. Barngrover and C. M. Aikens, "Oxidation of Gold Clusters by Thiols," *Journal of Physical Chemistry A*, vol. 117, no. 25, pp. 5377–5384, 2013.

[68] A. Fernando and C. M. Aikens, "Ligand Exchange Mechanism on Thiolate Monolayer Protected $Au_{25}(SR)_{18}$ Nanoclusters," *The Journal of Physical Chemistry C*, vol. 119, no. 34, pp. 20179–20187, 2015.

[69] Y. Pei, Y. Gao, and X. C. Zeng, "Structural Prediction of Thiolate-Protected Au_{38}: A Face-Fused Bi-icosahedral Au Core," *Journal of the American Chemical Society*, vol. 130, no. 25, pp. 7830–7832, 2008.

[70] H. Grönbeck, H. Häkkinen, and R. L. Whetten, "Gold - Thiolate Complexes Form a Unique c(4×2) Structure on Au(111)," *J. Phys. Chem. C*, vol. 112, no. 41, pp. 15940–15942, 2008.

[71] A. A. E. Reed, R. B. Weinstock, and F. Weinhold, "Natural Population Analysis," *The Journal of Chemical Physics*, vol. 83, no. 1985, p. 735, 1985.

[72] S. Zhen and G. J. Davies, "Calculation of the lennard-jones n–m potential energy parameters for metals," *Physica Status Solidi (a)*, vol. 78, no. 2, pp. 595–605, 1983.

[73] A. Klamt and G. Schuurmann, "COSMO: a New Approach to Dielectric Screening in Solvents with Explicit Expressions for the Screening Energy and its Gradient," *Journal of the Chemical Society, Perkin Transactions 2*, vol. 5, no. 5, p. 799, 1993.

[74] M. Uematsu and E. U. Frank, "Static Dielectric Constant of Water and Steam," *Journal of Physical and Chemical Reference Data*, vol. 9, no. 4, p. 1291, 1980.

[75] H. Häkkinen, "The Gold–sulfur Interface at the Nanoscale," *Nature Chemistry*, vol. 4, no. 6, pp. 443–455, 2012.

[76] V. Ravi, J. Binz, and R. Rioux, "Thermodynamic Profiles at the Solvated Inorganic − Organic Interface: The Case of Gold − Thiolate Monolayers," *Nano letters*, vol. 13, no. 13, pp. 4442–4448, 2013.

[77] C. Zeng, H. Qian, T. Li, G. Li, N. L. Rosi, B. Yoon, R. N. Barnett, R. L. Whetten, U. Landman, and R. Jin, "Total Structure and Electronic Properties of the Gold Nanocrystal $Au_{36}(SR)_{24}$.," *Angewandte Chemie (International ed. in English)*, vol. 51, no. 52, pp. 13114–8, 2012.

[78] H. Qian, Y. Zhu, and R. Jin, "Isolation of Ubiquitous $Au_{40}(SR)_{24}$ Clusters from the 8 kDa Gold Clusters," *Journal of the American Chemical Society*, vol. 132, no. 13, pp. 4583–4585, 2010.

[79] C. P. Joshi, M. S. Bootharaju, M. J. Alhilaly, and O. M. Bakr, "$[Ag_{25}(SR)_{18}]^{-}$: The "Golden" Silver Nanoparticle," *Journal of the American Chemical Society*, vol. 137, no. 36, pp. 11578–11581, 2015.

[80] T. A. D. Nguyen, Z. R. Jones, B. R. Goldsmith, W. R. Buratto, G. Wu, S. L. Scott, and T. W. Hayton, "A Cu_{25} Nanocluster with Partial Cu(0) Character," *Journal of the American Chemical Society*, vol. 137, no. 41, pp. 13319–13324, 2015.

[81] X. Yuan, N. Goswami, I. Mathews, Y. Yu, and J. Xie, "Enhancing Stability Through Ligand-shell Engineering: A Case Study with $Au_{25}(SR)_{18}$ Nanoclusters," *Nano Research*, vol. 8, no. 11, pp. 3488–3495, 2015.

[82] F. Pan, N. V. Perera, M. Ruzzi, T. Dainese, S. Antonello, A. Venzo, A. Zoleo, and K. Rissanen, "$Au_{25}(SEt)_{18}$, a Nearly Naked Structural Analysis by Single Crystal X-ray Crystallography and Electron Nuclear Double Resonance," *ACS Nano*, vol. 8, no. 4, pp. 3904–3912, 2014.

[83] Y. Chen, C. Liu, Q. Tang, C. Zeng, T. Higaki, A. Das, D.-e. Jiang, N. L. Rosi, and R. Jin, "Isomerism in $Au_{28}(SR)_{20}$ Nanocluster and Stable Structures," *Journal of the American Chemical Society*, vol. 138, no. 5, pp. 1482–1485, 2016.

[84] C. L. Heinecke, T. W. Ni, S. Malola, V. Mäkinen, O. A. Wong, H. Häkkinen, and C. J. Ackerson, "Structural and Theoretical basis for Ligand Exchange on Thiolate Monolayer Protected Gold Nanoclusters," *Journal of the American Chemical Society*, vol. 134, no. 32, pp. 13316–13322, 2012.

[85] C. Zeng, Y. Chen, C. Liu, K. Nobusada, N. L. Rosi, and R. Jin, "Gold Tetrahedra Coil up: Kekule-like and Double Helical Superstructures," *Science Advances*, vol. 1, no. 9, pp. e1500425–e1500425, 2015.

[86] J. P. Perdew, K. Burke, and M. Ernzerhof, "Generalized Gradient Approximation Made Simple- ERRATA," *Physical Review Letters*, vol. 77, no. 18, pp. 3865–3868, 1996.

[87] C. Lee, W. Yang, and R. G. Parr, "Development of the Colle-Salvetti Correlation-energy Formula into a Functional of the Electron Density," *Physical Review B*, vol. 37, no. 2, pp. 785–789, 1988.

[88] Y. Pei and X. C. Zeng, "Investigating The Structural Evolution of Thiolate Protected Gold Clusters from First-principles," *Nanoscale*, vol. 4, no. 14, p. 4054, 2012.

[89] P. Wang, X. Sun, X. Liu, L. Xiong, Z. Ma, Y. Wang, and Y. Pei, "A Revisit to the Structure of $Au_{20}(SCH_2CH_2Ph)_{16}$: a Cubic Nanocrystal-like Gold Kernel," *Nanoscale*, vol. 20, pp. 10357–10364, 2018.

[90] B. Chan and W.-L. Yim, "Accurate Computation of Cohesive Energies for Small to Medium-Sized Gold Clusters," *Journal of Chemical Theory and Computation*, vol. 9, no. 4, pp. 1964–1970, 2013.

[91] O. D. Haberlen, S. C. Chung, M. Stener, and N. Rosch, "From Clusters to Bulk: A Relativistic Density Functional Investigation on a Series of Gold Clusters Au_n, n=6...147," *Journal of Chemical Physics*, vol. 106, no. 12, pp. 5189–5201, 1997.

[92] G. Mpourmpakis, A. N. Andriotis, and D. G. Vlachos, "Identification of Descriptors for the CO Interaction with Metal Nanoparticles," *Nano Letters*, vol. 10, no. 3, pp. 1041–1045, 2010.

[93] M. J. Hostetler, J. E. Wingate, C.-J. Zhong, J. E. Harris, R. W. Vachet, M. R. Clark, J. D. Londono, S. J. Green, J. J. Stokes, G. D. Wignall, G. L. Glish, M. D. Porter, N. D. Evans, and R. W. Murray, "Alkanethiolate Gold Cluster Molecules with Core Diameters from 1.5 to 5.2 nm: Core and Monolayer Properties as a Function of Core Size," *Langmuir*, vol. 14, no. 1, pp. 17–30, 1998.

[94] A. Deka and R. C. Deka, "Structural and Electronic Properties of Stable Au_n (n=2–13) Clusters: A Density Functional Study," *Journal of Molecular Structure: THEOCHEM*, vol. 870, no. 1-3, pp. 83–93, 2008.

[95] P. Gruene, D. M. Rayner, B. Redlich, A. F. G. van der Meer, J. Lyon, G. Meijer, and A. Fielicke, "Structures of Neutral Au_7, Au_{19}, and Au_{20} Clusters in the Gas Phase," *Science*, vol. 321, no. August, pp. 674–676, 2008.

[96] A. Vargas, G. Santarossa, M. Iannuzzi, and A. Baiker, "Fluxionality of gold nanoparticles investigated by born-oppenheimer molecular dynamics," *Physical Review B - Condensed Matter and Materials Physics*, vol. 80, no. 19, pp. 1–13, 2009.

[97] N. Austin, J. K. Johnson, and G. Mpourmpakis, "Au_{13}: CO Adsorbs, Nanoparticle Responds," *The Journal of Physical Chemistry C*, vol. 119, no. 32, pp. 18196–18202, 2015.

[98] Q. Li, T.-y. Luo, M. G. Taylor, S. Wang, X. Zhu, Y. Song, G. Mpourmpakis, N. L. Rosi, and R. Jin, "Molecular "surgery " on a 23-gold-atom nanoparticle," *Science Advances*, vol. 3, no. 5, p. e1603193, 2017.

[99] Q. Li, M. G. Taylor, K. Kirschbaum, K. J. Lambright, X. Zhu, G. Mpourmpakis, and R. Jin, "Site-selective substitution of gold atoms in the $Au_{24}(SR)_{20}$ nanocluster by

silver," *Journal of Colloid and Interface Science*, vol. 505, no. 1 Nov 2017, pp. 1202–1207, 2017.

[100] Q. Li, K. J. Lambright, M. G. Taylor, K. Kirschbaum, T.-Y. Luo, J. Zhao, G. Mpourmpakis, S. Mokashi-Punekar, N. L. Rosi, and R. Jin, "Reconstructing the Surface of Gold Nanoclusters by Cadmium Doping," *Journal of the American Chemical Society*, vol. 139, no. 49, pp. 17779–17782, 2017.

[101] A. Das, T. Li, K. Nobusada, C. Zeng, N. L. Rosi, and R. Jin, "Nonsuperatomic $[Au_{23}(SC_6H_{11})16]^-$ Nanocluster Featuring Bipyramidal Au_{15} Kernel and Trimeric $Au_3(SR)_4$ Motif," *Journal of the American Chemical Society*, vol. 135, no. 49, pp. 18264–18267, 2013.

[102] M. G. Taylor and G. Mpourmpakis, "Rethinking Heterometal Doping in Ligand-Protected Metal Nanoclusters," *The Journal of Physical Chemistry Letters*, vol. 9, no. 23, pp. 6773–6778, 2018.

[103] J. Xiang, P. Li, Y. Song, X. Liu, H. Chong, S. Jin, Y. Pei, X. Yuan, and M. Zhu, "X-Ray Crystal Structure, and Optical and Electrochemical Properties of the $Au_{15}Ag_3(SC_6H_{11})_{14}$ Nanocluster with a Core–shell Structure," *Nanoscale*, vol. 7, no. 43, pp. 18278–18283, 2015.

[104] C. Kumara, K. J. Gagnon, and A. Dass, "X-ray Crystal Structure of $Au_{38-x}Ag_x(SCH_2CH_2Ph)_{24}$ Alloy Nanomolecules," *Journal of Physical Chemistry Letters*, vol. 6, no. 7, pp. 1223–1228, 2015.

[105] X. Kang, H. Chong, and M. Zhu, "$Au_{25}(SR)_{18}$: The Captain of the Great Nanocluster Ship," *Nanoscale*, vol. 10, no. 23, pp. 10758–10834, 2018.

[106] F. Alkan, A. Muñoz-Castro, and C. M. Aikens, "Relativistic DFT Investigation of Electronic Structure Effects Arising from Doping the Au_{25} Nanocluster with Transition Metals," *Nanoscale*, vol. 9, no. 41, pp. 15825–15834, 2017.

[107] S. L. Christensen, M. A. MacDonald, A. Chatt, P. Zhang, H. Qian, and R. Jin, "Dopant Location, Local Structure, and Electronic Properties of $Au_{24}Pt(SR)_{18}$ Nanoclusters," *Journal of Physical Chemistry C*, vol. 116, no. 51, pp. 26932–26937, 2012.

[108] Y. Negishi, K. Munakata, W. Ohgake, and K. Nobusada, "Effect of Copper Doping on Electronic Structure, Geometric Structure, and Stability of Thiolate-protected Au_{25}

Nanoclusters," *Journal of Physical Chemistry Letters*, vol. 3, no. 16, pp. 2209–2214, 2012.

[109] E. Gottlieb, H. Qian, and R. Jin, "Atomic-level Alloying and De-alloying in Doped Gold Nanoparticles," *Chemistry - A European Journal*, vol. 19, no. 13, pp. 4238–4243, 2013.

[110] S. Yamazoe, W. Kurashige, K. Nobusada, Y. Negishi, and T. Tsukuda, "Preferential Location of Coinage Metal Dopants (M = Ag or Cu) in $[Au_{25-x}M_x(SC_2H_4Ph)_{18}]^-$ (x   1) As Determined by Extended X-ray Absorption Fine Structure and Density Functional Theory Calculations," *The Journal of Physical Chemistry C*, vol. 118, no. 43, pp. 25284–25290, 2014.

[111] C. Kumara, C. M. Aikens, and A. Dass, "X-ray Crystal Structure and Theoretical Analysis of $Au_{25-x}Ag_x(SCH_2CH_2Ph)_{18}^-$ Alloy," *Journal of Physical Chemistry Letters*, vol. 5, no. 3, pp. 461–466, 2014.

[112] Q. Li, S. Wang, K. Kirschbaum, K. J. Lambright, A. Das, and R. Jin, "Heavily Doped $Au_{25-x}Ag_x(SC_6H_{11})_{18}^-$ Nanoclusters: Silver Goes from the Core to the Surface," *Chem. Commun.*, vol. 52, no. 29, pp. 5194–5197, 2016.

[113] C. Yao, Y. J. Lin, J. Yuan, L. Liao, M. Zhu, L. H. Weng, J. Yang, and Z. Wu, "Mono-cadmium vs Mono-mercury Doping of Au25 Nanoclusters," *Journal of the American Chemical Society*, vol. 137, no. 49, pp. 15350–15353, 2015.

[114] H. Qian, E. Barry, Y. Zhu, and R. Jin, "Doping 25-atom and 38-atom Gold Nanoclusters with Palladium," *Wuli Huaxue Xuebao/ Acta Physico - Chimica Sinica*, vol. 27, no. 3, pp. 513–519, 2011.

[115] M. A. Tofanelli, T. W. Ni, B. D. Phillips, and C. J. Ackerson, "Crystal Structure of the $PdAu_{24}(SR)_{18}^0$ Superatom," *Inorganic Chemistry*, vol. 55, no. 3, pp. 999–1001, 2016.

[116] H. Qian, Y. Zhu, and R. Jin, "Atomically Precise Gold Nanocrystal Molecules with Surface Plasmon Resonance.," *Proceedings of the National Academy of Sciences of the United States of America*, vol. 109, no. 3, pp. 696–700, 2012.

[117] Q. Yao, Y. Feng, V. Fung, Y. Yu, D.-e. Jiang, J. Yang, and J. Xie, "Precise Control of Alloying Sites of Bimetallic Nanoclusters via Surface Motif Exchange Reaction," *Nature Communications*, vol. 8, no. 1, p. 1555, 2017.

[118] S. Wang, H. Abroshan, C. Liu, T.-Y. Luo, M. Zhu, H. J. Kim, N. L. Rosi, and R. Jin, "Shuttling Single Metal Atom Into and out of a Metal Nanoparticle," *Nature Communications*, vol. 8, no. 1, p. 848, 2017.

[119] M. Kim, Q. Tang, A. V. Narendra Kumar, K. Kwak, W. Choi, D.-e. Jiang, and D. Lee, "Dopant-Dependent Electronic Structures Observed for $M_2Au_{36}(SC_6H_{13})_{24}$ Clusters (M = Pt, Pd)," *The Journal of Physical Chemistry Letters*, vol. 9, no. 5, pp. 982–989, 2018.

[120] Z. Ma, P. Wang, L. Xiong, and Y. Pei, "Thiolate-Protected Gold Nanoclusters: Structural Prediction and the Understandings of Electronic Stability from First Principles Simulations," *Wiley Interdisciplinary Reviews: Computational Molecular Science*, vol. 7, no. 4, p. e1315, 2017.